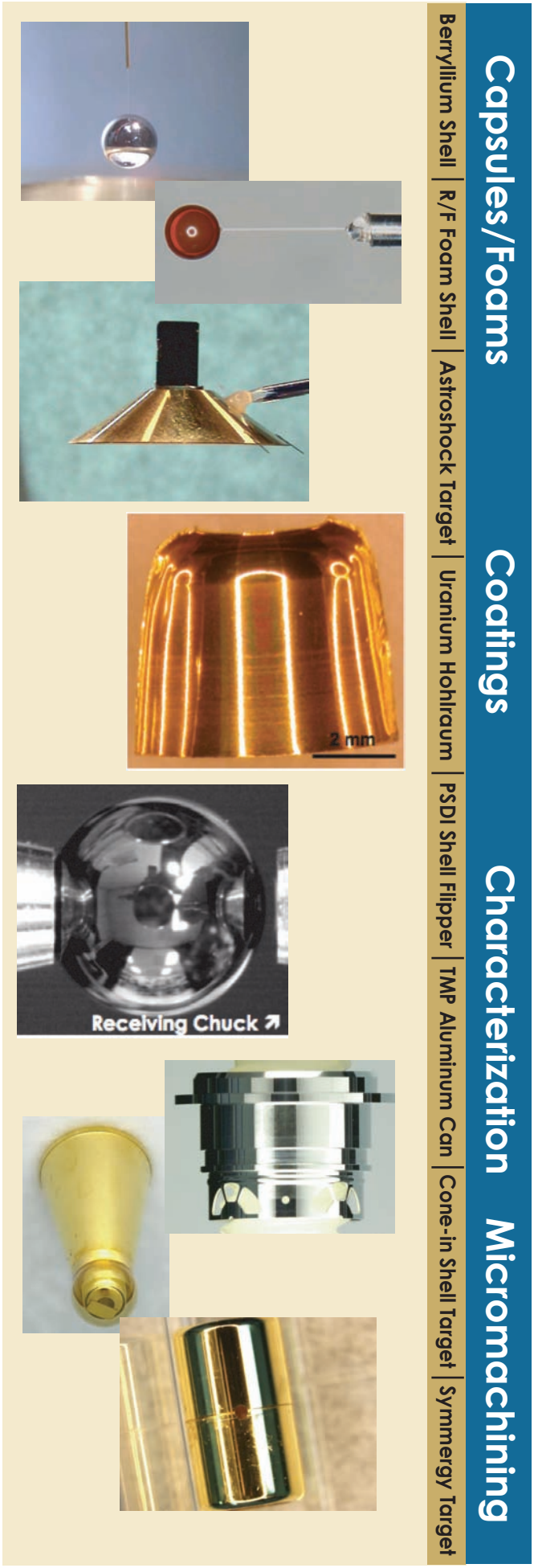

GA-A26340

INERTIAL CONFINEMENT FUSION

Annual Report

October 1, 2007
through
September 30, 2008

Schafer

GENERAL ATOMICS

GA–A26340

RESEARCH AND DEVELOPMENT AND FABRICATION OF INERTIAL CONFINEMENT FUSION TARGETS, COMPONENTS, AND COMPONENT TECHNOLOGY

ANNUAL REPORT TO THE U.S. DEPARTMENT OF ENERGY FOR THE PERIOD OCTOBER 1, 2007 THROUGH SEPTEMBER 30, 2008

by
PROJECT STAFF

Prepared under
Contract No. DE-AC52-06NA27279
for the U.S. Department of Energy

GENERAL ATOMICS PROJECT 30272
DATE PUBLISHED: FEBRUARY 2009

GENERAL ATOMICS

DISCLAIMER

GENERAL ATOMICS

ACRONYMS

AES	Auger electron spectroscopy
AFM	atomic force microscope
Ar	argon
AuB	gold boron
Be	beryllium
CD	carbon deuterium
CFTA	capsule fill tube assembly
CH	carbon hydrogen
CR	contact radiography
CTM	cryogenic target mount
CTS	cryogenic target system
D_2	deuterium
DG	droplet generator
DLA	diffusion limited aggregation
DOE	Department of Energy
DR	differential radiography
DT	deuterium-tritium
DU	depleted uranium
EDS	energy dispersive spectroscopy
EDXS	energy dispersive x-ray spectroscopy
FTIR	Fourier transform infrared spectroscopy
FWHM	full width half maximum
GA	General Atomics
GDP	glow discharge polymer
HDRF	high density resorcinol formaldehyde
HED	high energy density
HEDP	high energy density plasma
ICF	Inertial Confinement Fusion
IFT	Inertial Fusion Technology
ITIC	ignition target inserter cryostat
LANL	Los Alamos National Laboratory
LLCS	load, layer and characterization system

LLE	Laboratory for Laser Energetics
LLNL	Lawrence Livermore National Laboratory
MIFEDS	magneto inertial fusion electrical discharge system
MS	mass spectrometer
MW	molecular weight
NC	non-concentricity
NIC	National Ignition Campaign
NIF	National Ignition Facility
NLUF	National Laser Users Facility
NNSA	National Nuclear Security Administration
NRL	Naval Research Laboratory
PAA	poly acrylic acid
PAMS	poly-α-methylstyrene
PSDI	phase-shifting diffraction interferometer
PVA	poly vinyl alcohol
R/F	resorcinol formaldehyde
SBS	styrene-butadiene-styrene
SCD	strong carbon deuterium
SDRF	standard density resorcinol formaldehyde
SEM	scanning electron microscopy
Si-GDP	silicon-doped glow discharge polymer
SNL	Sandia National Laboratory
SNRT	Supernova Rayleigh-Taylor
SSP	Stockpile Stewardship Program
T_2B	trans-2-butene
TAS	target alignment system
TGA	thermogravimetric analysis
Ti-GDP	titanium-doped glow discharge polymer
TMG	tetramethyl germane
TMP	thermomechanical package
TMS	tetramethyl silane
U	uranium
UR/LLE	University of Rochester Laboratory for Laser Energetics
USAXS	ultra small angle x-ray scattering
XAS	x-ray absorption spectroscopy
XRF	x-ray fluorescence

TABLE OF CONTENTS

LIST OF FIGURES

LIST OF TABLES

1. INTRODUCTION

This report documents General Atomics' (GA) fiscal year 2008 (FY08) activity for Inertial Confinement Fusion (ICF), a research and development program of the U.S. Department of Energy (DOE) National Nuclear Security Administration (NNSA). The program goals are controlled nuclear fusion at laboratory scales using large laser and pulsed power facilities in the U.S., and conducting experiments relevant to high energy density physics (HEDP) using those same facilities. The ICF Campaign, which includes the National Ignition Campaign (NIC) and HEDP experiments, is presently executed at six sites: Los Alamos National Laboratory (LANL), Lawrence Livermore National Laboratory (LLNL), Sandia National Laboratories (SNL), the University of Rochester Laboratory for Laser Energetics (UR/LLE), the Naval Research Laboratory (NRL) and GA. There are three major ICF facilities where this work is performed: the OMEGA glass laser at UR/LLE, the Z pulsed-power facility at SNL, and the National Ignition Facility (NIF) at LLNL to be completed in FY09. These facilities are supplemented by LANL's Trident laser, NRL's Nike laser and other smaller lasers.

General Atomics' Inertial Fusion Technology (IFT) division concentrates on producing the targets and doing the R&D for the targets for experiments which are carried out at the above facilities and SNL's Z pulsed power facility. Through target fabrication, GA supports the ultimate goal of the ICF Campaign to develop laboratory capabilities to create and measure extreme conditions of temperature, pressure, and radiation density, including thermonuclear burn conditions that approach those in nuclear weapons, and to conduct weapons-related research in these environments and achieving HEDP conditions, critical to validate codes and to characterize weapons component performance. In this effort, GA supports all four of the strategies of NNSA's ICF Campaign to accomplish this long-term goal:

1. Achieve ignition in the laboratory and develop it as a scientific tool for stockpile stewardship.
2. Support execution of HEDP experiments necessary to provide advanced assessment capabilities for stockpile stewardship.
3. Develop advanced technology capabilities that support long-term needs of stockpile stewardship.
4. Maintain robust national program infrastructure and attract scientific talent to the SSP.

In FY08, GA continued its support of NNSA's ICF program by on time delivery of nearly 3000 fully characterized target components and targets, necessary to enable ICF and HEDP experiments at the various facilities. In doing so, the GA target fabrication group, an ISO 9001:2000 registered program, maintained excellent communication with the users of the targets to ensure adherence to the required quality and quantity, while continually seeking to improve processes to increase efficiency and enhance the performance of the team. As well as getting extensive and generally very positive feedback from its customers in FY08, the GA staff authored a number of papers in refereed journals and presented work at major international conferences. Highlights of the GA ICF technology work

performed under DOE Contract No. DE-AC52-06NA27279 in FY08 comprises the subject of this report.

In FY08, the OMEGA laser accounted for the majority of experiments for ICF and HEDP. Each shot requires a new and generally completely different type of tightly specified and well-characterized target for each day or half day of shots. The Z facility had a major refurbishment in FY07 and is now back online. In FY08, GA produced many different types of components for these facilities. Many of the components are novel and were made by techniques requiring significant development. As the targets are the initial conditions for the experiments, the targets and components need to be accurately measured and characterized for each shot, which destroys the target.

In Section 2 we give a brief overview of the fabrication centers within GA's IFT group that ensure delivery of the various components needed for ICF experiments. In Section 3, we summarize the target deliveries for these facilities and include descriptions of some target deliveries of note. In FY08, GA worked closely with LLNL — and the other sites — to manage the rolling specification of hundreds of targets per year required for OMEGA, through weekly teleconference and video conference meetings under a Change Control Board (CCB). Such meetings ensured that target specifications for each facility shot day, which is essentially a new experimental campaign, were specified well enough in advance for complete manufacture and characterization of the target to specification.

In Section 4, we summarize research and development work for the ignition campaign on the NIF (NIC Target Development); in Section 5 for supporting current deliveries for OMEGA (NIC x-ray drive target production and NIC direct drive target production); and in Section 6 for Z (SNL Target Development and Production). This development work has been presented to peers in the inertial fusion and HEDP community at major international conferences (e.g., Inertial Fusion Sciences and Applications, IFSA, in Kobe, Japan and the American Physical Society Division of Plasma Physics, APS/DPP). These sections have selected work presented at these major meetings; also included in these technical sections is closely related target work on fast ignition and inertial fusion energy funded via related contracts.

Demonstration of laboratory ignition is the highest priority and a major objective of NNSA. This work is encompassed in the NIC, which is an enhanced management activity of the NNSA, managed with the rigor of a project. There is a point design for the ignition target for the NIC. Major R&D is required to produce this target for 2010 due to the demanding specification on the ignition targets, the cryogenic capability required for ignition, and the higher quality standards required for experiments on the NIF.

In FY08, GA was the major program participant in the development of the non-cryogenic components of the new NIC targets. These include fuel capsules with graded doped ablators with micron-scale fill tubes. The specifications on the surface finish, roundness, uniformity, doping fraction, fill tube fillet, etc., are demanding. The cryogenic hohlraum that contains the capsules is continuing to evolve. GA is fabricating the prototypes and pieces used in current cryogenic fuel layering experiments. An accelerated program of R&D and preparing for facilitization to produce hundreds of targets per year is ongoing to ensure the success of the NIC. GA also supports the

Cryogenic Target System (CTS) for the NIF by supplying LLNL-onsite engineering and technician staff.

Development for current x-ray drive targets on OMEGA includes surrogate target components that are shot on OMEGA in preparation for NIC development work. For current direct drive targets on OMEGA, development includes novel ways of attaching fill tubes to direct-drive targets, ways of making targets to achieve enhanced implosion performance and x-ray yield for backlighting. Research for SNL includes a design to create targets for Z with many fill tubes on the large Z targets enabling several experiments on one shot to help examine the way the fill tube itself perturbs an implosion.

Comments and requests for further information may be directed to the GA Inertial Fusion Technology Program Manager, Abbas.Nikroo@gat.com, (858) 455-2931.

2. FABRICATION AND DEVELOPMENT CENTERS WITHIN GA IFT

2.1. CAPSULES

The Center for Capsule Production is responsible for the manufacturing of thin-layer microcapsule components and targets for experiments carried out at OMEGA, Z, NIF and other laser facilities for LLNL, LANL, UR/LLE, NLUF and SNL. In FY08, the Capsule Production Center produced approximately 1300 components and targets for 100 line items.

Capsule development for FY08 included improved Hoppe glass capsule production via a new agitation technique to reduce the incidence of wall wrinkling, and, expanded the experimental scope of Hoppe glass by introducing germanium doping. Silicon doped GDP capsule production was supplemented with additional characterization to study IR absorbance. The largest diameter (4000 μm) hemi shell ever produced in IFT was fabricated in a joint effort with the Center for Precision Manufacturing.

LANL deliveries focused on Hoppe glass and GDP capsules with gas permeation barriers. We again provided a special order of GDP capsules implanted with C^{13} isotope for the LANL Betamix experiment.

UR/LLE cryogenic experiments on OMEGA were supported by production of thin walled (~10 μm) strong CD and standard density (100 mg/cc) resorcinol formaldehyde (R/F) foam capsules with a GDP permeation barrier. Capsules were also delivered for use in qualifying the OMEGA-EP lasers. Deuterium-filled drop tower glass capsules were delivered for Fusion Science Center, HXRCal, Proton Backlighter, and MIFEDS experiments. High density (200 mg/cc) R/F foam capsules with a GDP layer and an attached fill tube were produced for room temperature surrogate shots.

NLUF deliveries included GDP capsules with a Ti-GDP layer for Core Imaging, and drop tower glass as well as polymer capsules for Prad.

SNL deliveries expressed reduced deliveries due to the Z machine shutdown, however, we continued support for developmental Fast Igniter targets supplying the GDP hemi-shells.

2.2. CENTER FOR PRECISION MANUFACTURING

The Center for Precision Manufacturing is responsible for the manufacturing of micro-machined components and machined targets for experiments carried out at OMEGA, Z, NIF and other laser facilities for LLNL, LANL, SNL, UR/LLE and several Universities. The Center for Precision Manufacturing in FY08 produced a total of 1284 components and targets. The majority of the components and targets are new and unique and required the development of new fabrication and characterization techniques.

The Center for Precision Manufacturing has fabricated, characterized and assembled several new types of targets in FY08, examples include: Shock Timing targets for UR/LLE, Fast Ignition targets for SNL, Implosion Symmetry targets for LANL, Thin Wall Hohlraums for LLNL-HEDP, and Super Nova Raleigh Taylor (SNRT) targets for the University of Michigan.

2.3. FOAMS AND MATERIALS CENTER

The Foams and Materials (FMS) Center produces a wide range of components and performs R&D work towards fabricating first of a kind targets. These targets were for experiments performed by LLE, LLNL, AWE and various universities. The FMS center in FY08 produced a total of 147 components and targets. (Not counting routine internal production of items such as PAMS mandrels for NIC capsules.) A number of these targets required extra development beyond ordinary production.

Several new targets were produced by the FMS center in FY08. In support of the NIF direct drive campaign, 3 mm diameter foam capsules with fill tubes for cryogenic layering experiments were developed, fabricated and delivered. We also developed the techniques necessary to produce foam shells at this large diameter with a thin (gas retentive) GDP layer. For OMEGA National Laser User Facility (NLUF) shots, we provided targets with two embedded spheres suspended only by the foam matrix, as well as targets with a tracer layer of titanium on the spheres. These targets were made with no visible density perturbations to the foam layer.

2.4. NIF CENTER

The center for NIF target development and fabrication is focused on developments necessary for producing NIF target components. These include areas that deal with fabrication and metrology of beryllium and CH capsules, laser machining of capsules and hohlraums, uranium hohlraums, subassemblies of capsules with fill tubes as well as thermomechanical package components used for fielding cryogenic targets. It also draws from the center for precision machining described above.

3. DELIVERY SUMMARY

3.1. DELIVERIES FROM SAN DIEGO

GA supplied nearly 3000 target and target components to LLNL, LANL, SNL, UR/LLE and others in FY08. Capsules and micromachined components comprise the majority of the components built at GA in support of this work. Figure 3-1 shows the deliveries for FY08 by laboratory or program on a quarterly basis. Table 3-1 summarizes these deliveries by major component types, capsules, micromachined and foam components, and "miscellaneous" components, such as flat plates with various precise surface perturbations, which in some cases can be more challenging to build. Table 3-2 shows a list of different types of components broken down more specifically by type, such as foam or beryllium shells.

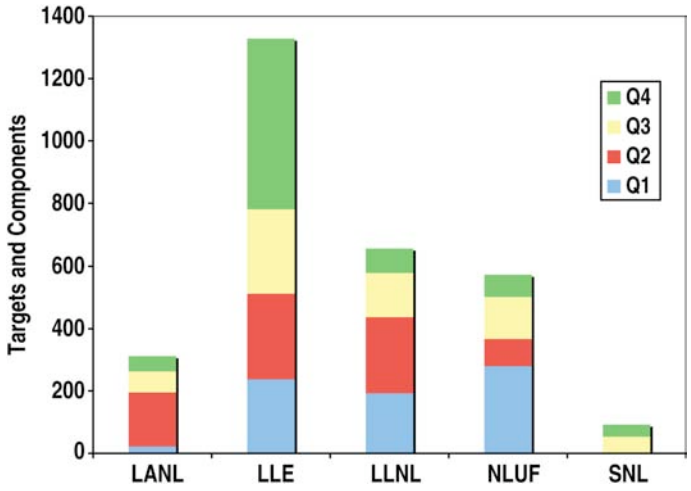

Fig. 3-1. FY08 deliveries by laboratory by quarter.

Table 3-1
FY08 Deliveries by High Level Components

	Orders	Capsules	μMachined Components	Foams	Miscellaneous Including Assemblies
LLNL	75	71	513	0	71
LANL	31	110	202	0	0
SNL	20	0	51	0	41
UR/LLE	130	999	263	19	47
NLUF	63	104	331	128	10
TOTAL	**319**	**1284**	**1360**	**147**	**169**

Table 3-2
Deliveries Broken Down by Specific Types of Components

Component Type	Total
Capsule-Be capsule	32
Capsule-CRYO	365
Capsule-Drop Tower Glass capsules	185
Capsule-Fill tube	12
Capsule-Germanium doped for CRYO	8
Capsule-Glass shell with fill	102
Capsule-Hoppe Glass capsules	53
Capsule-Other	25
Capsule-polymer capsules	455
Capsule-RF foam	20
Capsule-Si-GDP shells	33
Hohlraum-Hard	107
Hohlraum-Medium	94
Hohlraum-Simple	257
Package-Beryllium foil without a pattern	12
Package-Disk	136
Package-Foam	49
Package-Foil	389
Package-Other	121
Package-Patterned Be	13
Package-Patterned Foil	48
Polystyrene	16
Special-Ball in foam	10
Special-ball on cone	45
Special-Cone	72
Special-FI ball on cone	28
Special-Fill tube	7
Special-IR diffuser	7
Special-Laser Hole	15
Special-Other	129
Special-Saturn ring	6
Special-washer	105
Grand Total	2960

3.1.1. Capsule Deliveries

GA delivered a total of 1284 precision, fully characterized capsules of many different types. These included a wide variety of capsules ranging from plain CH, to cryogenic thin wall CD, to glass capsules. These deliveries and the some of the related developmental types are summarized below by laboratory.

LANL. The capsule group coordinated delivery of 110 capsules in 2008. This included CH capsules with gas permeation barriers for the symmergy campaign in support of the NIC OMEGA experimental series. We also provided beryllium capsules with fill tubes for this campaign, a first of kind for OMEGA (Fig. 3-2). We leveraged the developmental activities discussed later to fabricate Be shells, drill holes to allow fill tube attachment and verify gas filling capability and fielding of these capsules. The LANL assembly team installed these capsules in hohlraums made by GA. Neutron yields were measured in these symmetry experiments as precursors for those to be performed on NIF in FY09-10.

Fig. 3-2. Beryllium shell with fill tube.

We provided a special order of CH capsules implanted with upwards of 90% C^{13} isotope for the Betamix experiment. The C^{13} capsule was utilized for spectra analysis on OMEGA. We advanced Hoppe glass capsule production methods by developing agitation techniques and modifying process conditions to reduce the incidence of wall wrinkling in thinner walled capsules for improved surface quality, and expanded the experimental scope of Hoppe glass by introducing a high Z doped glass, specifically germanium. This development is discussed later in the OMEGA development section.

LLNL. We provided 30 bismuth coated CH shells for the Re-emit experiments that were designed to prove the technique to be used on NIF. Figure 3-3 shows a Bi coated shell.

We also supplied 8 very thin beryllium shells that were used in the “thin shell” experiments on OMEGA that again provided data to allow a decision as to the utility of this technique for future NIF experiments. In addition, 15 multilayer Be:Cu shells were supplied and 48 standard GDP shells. Figure 3-4 shows a radiograph of a thin walled (~12 μm) Be shell.

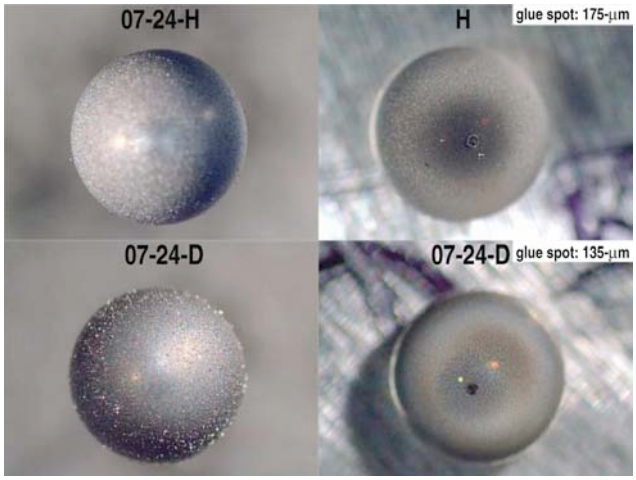

Fig. 3-3. Bi coated shell fabricated at GA.

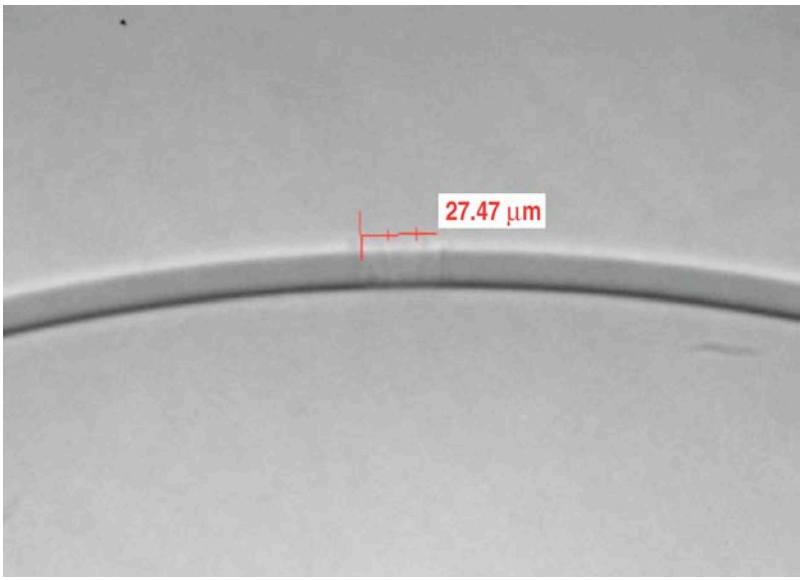

Fig. 3-4. Radiograph of a 2 mm Be shell with a 12 μm wall and 27 μm fill hole.

LLE. In FY08, our group coordinated delivery of 999 capsules to UR/LLE with special focus on capsules for cryogenic shots on OMEGA.

Cryogenic experiments at UR/LLE were supported by the production of thin walled, strong CD capsules. Capsule wall thicknesses varied from 13 μm to as thin as 2 μm. Each delivered shell was wallmapped for wall uniformity and spheremapped for comparison to the NIF standard. Shells from each batch were analyzed for buckle pressure.

In addition, 3 mm foam shells were delivered for cryogenic tests. Standard density (100 mg/cc) R/F foam shells with a GDP permeation barrier were also delivered for cryogenic experiments.

A new type of target that was produced and delivered in FY08 was a high density (200 mg/cc) R/F foam shell with a fill tube (Fig. 3-5). This target was developed due to the difficulties in

producing a reliable permeation barrier on such foam shells. The development of such targets is discussed later in Section 5.

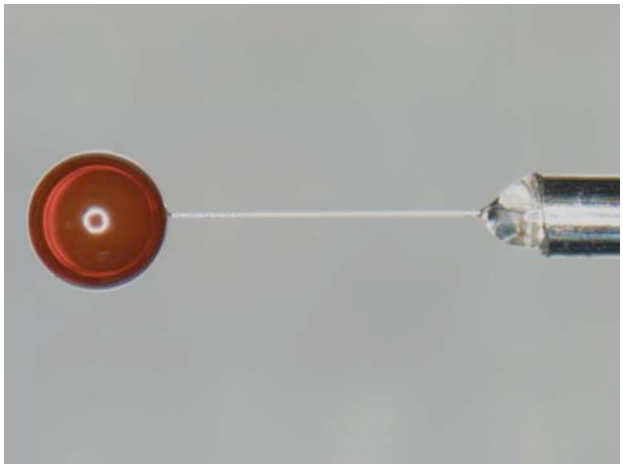

Fig. 3-5. 900 μm GDP coated R/F foam shell with fill tube attached.

Thin-walled Si-GDP shells were developed and delivered for cryo experiments, with additional characterization to study IR absorbance. Shells with walls from 12 to 40 μm in thickness were delivered for experiments such as Diagnostic Development, Ablator Proton, and Polar Direct Drive, and for use in qualifying the EP lasers. Deuterium-filled drop tower glass shells were delivered for Fusion Science Center, HXRCal, Proton Backlighter, NLUF and MIFEDS experiments. High density (200 mg/cc) R/F foam shells with a GDP layer and an attached fill tube were produced for room temperature surrogate shots. Developments in foam shells and SiGDP shells are discussed in more detail in Sections 4 and 5.

NLUF Capsules. GA coordinated delivery of 104 capsules in FY08 to NLUF. Capsules for NLUF experiments included GDP shells with a Ti-GDP layer for Core Imaging and glass backlighter and polymer shells for Prad. Backlighter shells were used by Rich Petrasso in a variety of experiments to use protons to radiograph Rayleigh-Taylor evolution of perturbations on flat plates. This work was published in the journal *Science*.

3.1.2. Micromachining Deliveries

LLE. We delivered 263 target components for LLE. The majority of the deliveries were cone-in-shell targets, which included machining and production of CH shells as well as gold components and precision assembly of these components into full targets. These targets were used for the very important shock timing experiments on OMEGA. Shock Timing experiments use the cone-in-shell target to observe shock-breakout on imploding capsules. Figure 3-6 shows a photomicrograph of an assembled cone-in-shell target. The special characteristic of this type target is the accurate position of the tip of the cone with respect to the top of the capsule both in the radial and axial directions and a leak tight and cryogenic capable joint between the cone and capsule. To facilitate the positioning of the cone with respect to the capsule, both are machined utilizing high precision diamond turning lathes and precision fixtures. During assembly, the position of the cone with respect to the capsule is

checked using high precision measuring equipment. To facilitate viewing and focusing of the inside of the capsule at the OMEGA facility, the cone is machined with a 14 μm wide annular feature on the inside of the cone as shown in Fig. 3-7.

Fig. 3-6. Shock timing cone-in-shell target used to observe the shock-breakout on imploding capsules.

Fig. 3-7. Alignment feature for two-piece hohlraum. Cone is machined with a 14 μm wide annular feature on the inside of the cone.

LANL. We delivered 202 target components for LANL. These included hohlraums, halfraums, cone targets and tantalum washers.

Collaboration between the Center for Precision Manufacturing and the Target fabrication group at LANL resulted in the design of a two-piece hohlraum intended to study implosion symmetry of CH and Be capsules. The two hohlraum halves were machined with male and female alignment features on their flanges that allow proper registry of the hohlraum halves and proper alignment of the diagnostic holes. Figure 3-8 shows a schematic of the type of alignment feature that was used. Figure 3-9 shows a photomicrograph of the two-piece hohlraum.

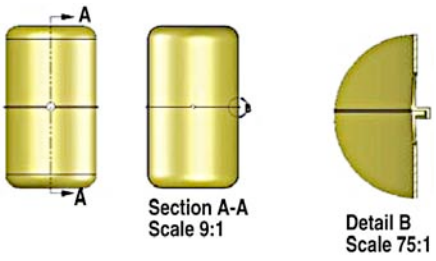

Fig. 3-8. Alignment feature for two-piece hohlraum.

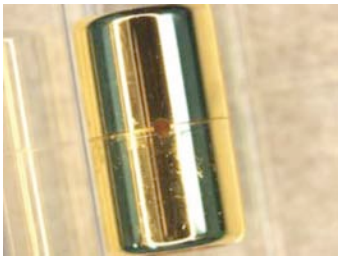

Fig. 3-9. Symmergy target with two-piece hohlraum.

LLNL Deliveries. We delivered 513 micromachined target components for LLNL including hohlraums, halfraums, cones and washers. We provided hohlraums that were used in the experiments supporting NIC, such as convergent ablation with precision slots to allow streak image recording of the implosion, and for the Re-emit campaign.

NLUF Deliveries. We delivered a total of 331 components for a number of NLUF campaigns. These included halfraums and other machined parts for Astroshock, precision washers and discs for Prad as well as perturbed foils for Supernova Rayleigh-Taylor (SNRT) experiments. The SNRT targets were particularly challenging from both fabrication and metrology points of view and we discuss these here in more detail.

Astrophysical phenomena such as Supernova hydrodynamics can be scaled down and studied in a laboratory system. The Center for Radiative Shock Hydrodynamics at the University of Michigan is studying these hydrodynamic effects by observing the growth of instabilities produced on drive disks machined with known perturbations. A complicated 51-mode perturbation was machined on a Polyimide – CHBr drive disk using a Fast Tool Servo. Figure 3-10 shows a photomicrograph of the machined drive disk and the resulting hydrodynamic instabilities. The Center for Precision Manufacturing had previously made periodic patterns using the Fast Tool Servo and these were easily characterized by white light interferometry or Confocal microscopy and simple 1-D line outs. For the non-periodic 51-mode perturbation, a 1-D line-out comparison is not possible so a new characterization technique had to be developed to analyze the machined pattern to determine the mode structure and compare it to the desired pattern. Figure 3-11 shows the desired pattern and the actual pattern in X-Y space. The 51 mode pattern was analyzed by doing a 2-D Fast Fourier Transform of the height data of the pattern. The height data was obtained from interferometric metrology data obtained with a WYKO. The 2-D Fast Fourier Transform of the height data provides the amplitude of the various modes and by plotting the intensity in kx and ky space it can be compared to the analytical expression describing the 51 mode pattern. The machined pattern was able to match the desired pattern up to mode 15. Frequency response of the piezoelectric stack, tool size, and phase lag limits of the Fast Tool Servo limited the machining of high mode numbers for the complex 51-mode perturbation.

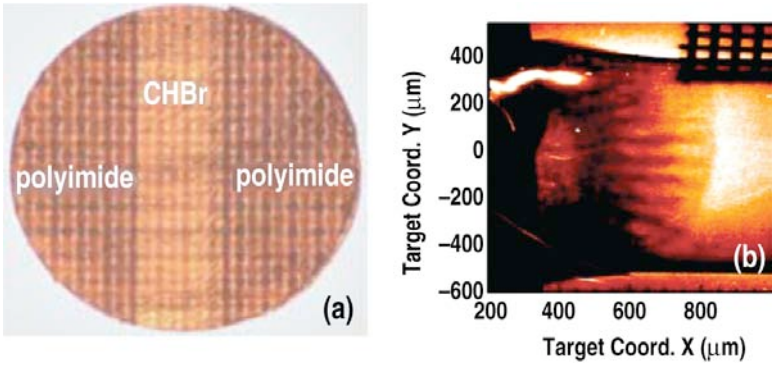

Fig. 3-10. SNRT drive disk and resulting hydrodynamic instability.

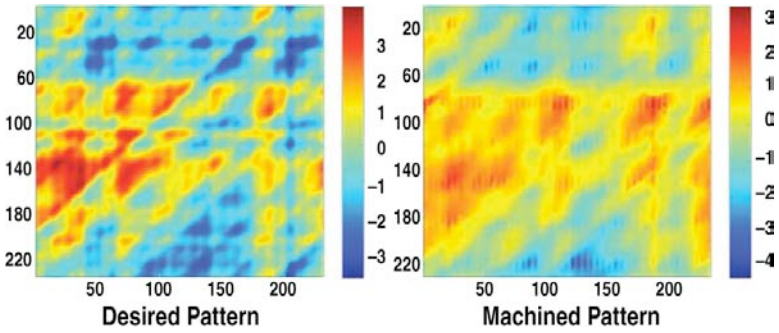

Fig. 3-11. Fifty-one mode perturbation pattern.

3.1.3. Foam Deliveries

We delivered a total of 147 foam-containing components, mainly spheres, multi-layer films, and cylinders.

LLE. We delivered 6 R/F foam capsules with fill tubes and 13 multi-layer films consisting of a **Si**-GDP/GDP/RF foam.

NLUF Deliveries. We delivered a total of 128 components consisting of disks, foams with embedded spheres, and foam cylinders.

3.1.4. Miscellaneous Deliveries

We delivered a total of 169 components that were outside the traditional capsule and micromachined component categories. These included witness plates made using various deposition and laser cutting techniques and foam components.

LLE. We provided a number of rippled flat targets for use at OMEGA, including rippled CH flats and multi-layer flats. We also produced multilayer flats with perturbations where one of the layers was a low density foam. Perturbations were machined into the full density layer which was overcoated onto the foam layer using an Excimer laser. While periodic perturbations of desired wavelength could be machined, the second harmonic amplitude compared to the desired fundamental was deemed too large as the experiments become more precise. Our goal in FY09 is to improve this process to reduce the second harmonic amplitude. Figure 3-12 shows the machined features and the associated power spectra.

We also delivered flats of CH and Ge doped CH to LLE for examining signals in tracking shocks through such materials in measuring their equation of state.

LLNL. We made a series of flat Be and plates with and without perturbations which were polished or roughened to mimic the surface finish of Be and CH capsules designed for NIF. These were made by Be deposition on flat mandrels, laser cutting the deposited material into the required dimensions and leaching from the mandrels. We worked to metrologize these more precisely (beyond the usual surface finish metrology) using capabilities at LLNL, which included transmission electron

microscopy and ultra-small angle x-ray scattering (performed at Advanced Photon Source). These targets provided crucial data on how capsule imperfections can seed instabilities in the capsule implosion process and compromise ignition.

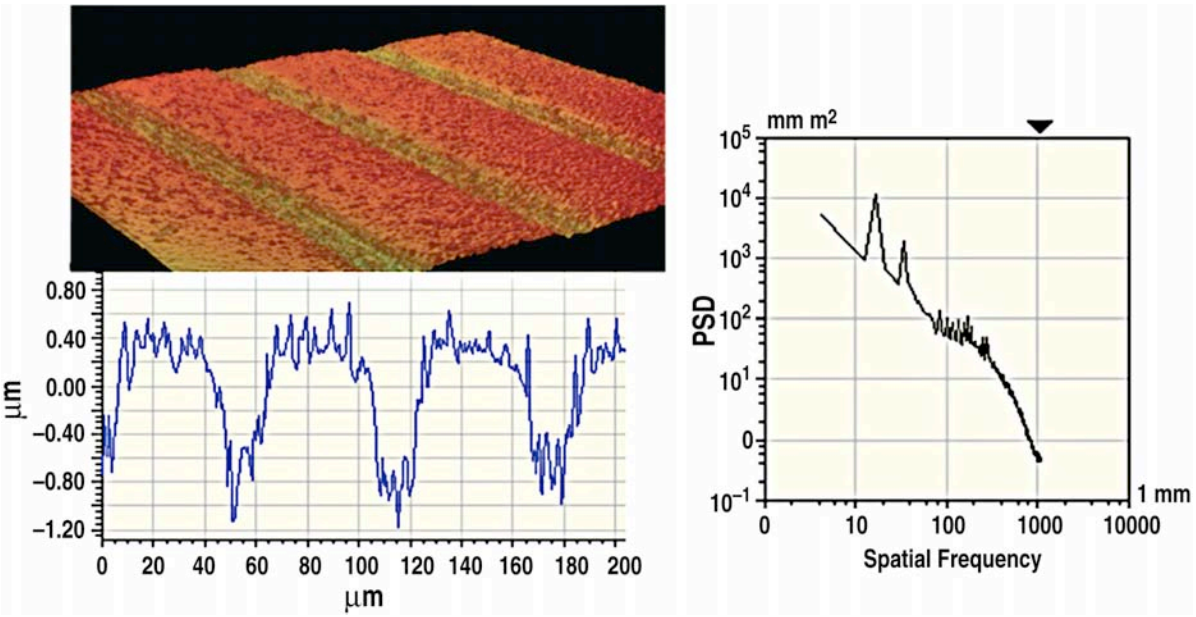

Fig. 3-12. Machined features and the associated power spectra of rippled flat targets.

NLUF. We provided foam components for both the Astroshock and Prad campaigns. These included shock or jet tubes, which in some cases contained embedded spheres to mimic astrophysical phenomena. The embedded sphere targets are discussed in Section 5.

Foam cylinders were fabricated and delivered for the Prad and Astroshock NLUF experimental series. For the Astroshock shots, we were able to provide targets with two embedded spheres suspended only by the foam matrix, as well as targets with a tracer layer of titanium on the spheres. These targets were made with no visible density perturbations to the foam layer.

NLUF targets were fully assembled in most cases by the GA team. The majority of these targets were assembled onsite at SNL while Z was being refurbished. Some examples include the Astroshock targets as shown in Fig. 3-13.

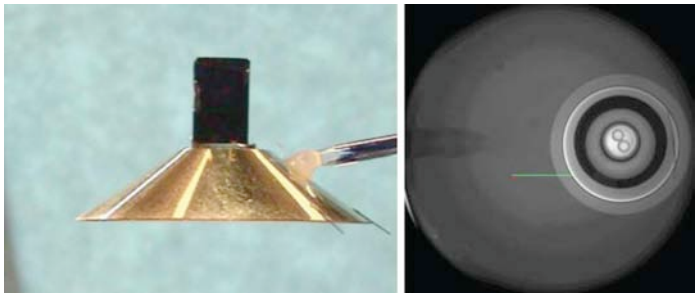

Fig. 3-13. Astroshock target.

3.1.4. Onsite Support

The GA/Schafer team provided onsite support for assembly and other related activities at all three sites primarily involved in OMEGA experiments, i.e., LLNL, LANL and LLE. GA had four onsite personnel at LLNL in support of OMEGA experiments at the beginning of the fiscal year. One of these personnel was transferred to support the NIF development described later. We continued to have one onsite person at LANL and one at UR/LLE in FY09.

3.2. SNL DELIVERIES

The effort at Sandia National Laboratories (SNL) provided targets for both drivers operated at SNL, Z and Saturn, and for SNL sponsored experiments at OMEGA. Table 3-3 shows the number and types of targets fabricated for these facilities.

Table 3-3
Target Fabrication Support Provided at SNL

SNL FY08		
	Targets	**Foams**
Z shots	82	12
Saturn	40	
OMEGA SNL	25	
OMEGA others	84	21

Z was refurbished in FY07 and resumed experiments in mid October 2008. During FY08, the facility worked to increase its power and its shot rate. It finished the year with 82 shots, very reduced from the FY06 level of 200 shots. The targets fielded at Z were of three types: wire array, equation of state (EOS) and cylindrical ICF targets. The targets fielded on Saturn were unique wire arrays.

3.2.1. Onsite Support

A major on site effort at Sandia was performed for Z by the GA/Schafer and Ktech team. Through this effort, components were fabricated as needed, assembled into targets and then incorporated into load assemblies for shots on Z. In addition to this effort, components were fabricated at GA for a significant fraction of target assemblies listed in Table 3-3. A number of these targets were developmental as described in Section 6. Some involved capsules and traditional micromachined components.

3.2.2. Capsule Support for SNL

Our group coordinated delivery of 19 capsules to SNL in 2008, expressing reduced production quantities due to the Z machine shutdown for most of FY07. We continued support for developmental Fast Igniter targets, supplying the inner and outer GDP hemi-shells. Target production included the fabrication of the largest diameter hemi-shell ever made at GA with a 4000 μm inner diameter. These developments are discussed in Section 6.

3.2.3. Micromachined Components for SNL

Sandia National Laboratory is exploring using single-sided Z-pinch radiation drive for Fast Ignition experiments. In Fast Ignition, compression and ignition are two separate steps. In this experiment, the compression step is achieved by radiation drive, single-sided Z-pinch. A Petawatt, short pulse laser, achieves the ignition step. A schematic of the Fast Ignition Target is shown in Section 6. This particular target consisted of six precision-machined components that are assembled together into a target with very tight tolerances. The machining of the inner capsule is a complicated process. A capsule cutting process had to be developed to ensure the survivability of the 4 μm thick hemi-shell. The process was developed in collaboration with SNL and consists of accurately positioning and gluing a GA produced thin walled capsule to a mounting fixture at SNL, sending the glued capsule assembly back to GA where it is placed in a special fixture, and then cutting away half of the capsule with a diamond tool. The resulting hemi-shell is sent back to SNL for final assembly.

4. NIF TARGET DEVELOPMENT AND SUPPORT

Although NIF is scheduled to be completed in FY09 and was not shooting targets in FY08, we produced a variety of components for the NIF target assembly developmental effort at LLNL. We also produced components for studies in forming cryogenic DT layers that meet specification including the design of the thermomechanical package (TMP) structure used to provide the required cooling and housing for the hohlraum. In this effort, we continued our development of capsules and hohlraums, as well as being integral in TMP design development. We also delivered over 1000 components for this effort, often demonstrating the agility to keep up with the design changing on a weekly basis. Finally, we also supported the construction of the cryogenic target system for handling and fielding cryogenic targets on NIF. This section describes our effort in these various areas.

GA also had four onsite personnel in target fabrication, mainly in final assembly, at LLNL in support of NIF target fabrication activities. GA provided three onsite personnel for the cryogenic insertion system under construction for NIF.

4.1. INDIRECT DRIVE NIF TARGET DEVELOPMENT

4.1.1. NIF Capsule Fabrication and Metrology Development

In FY08, we continued our collaborative efforts with LLNL to produce beryllium and CH shells that meet all NIF design specifications and evaluated the yield of the process. In this effort, we also made a series of capsules to support the effort at LLNL on cryogenic layering of NIF capsules. These included CH shells (which allow optical examination of the layers) as well as Be shells. These shells were fitted with a fill tube as described later to allow filling of the capsule cryogenically.

Development of Be shells concentrated on reduction of argon content in the shell wall while keeping gas retentiveness of the shells. We also continued improving hole drilling in Be shells as the microstructure of Be changed upon changes in the deposition process. We also focused on fill tube attachment and matured that process into one that supplied a steady supply of shells for the layering work. CH shell development was mainly focused on further reducing the isolated defects on CH shells to allow scale up fabrication capacity.

Metrology of both CH and Be shells was further enhanced through implementation of the shell flipper system developed at LLNL on the phase-shifting diffraction interferometer (PSDI) to fully map the shell for such isolated defects. Also, the PSDI was further improved at GA to allow more rapid examination of the shells using batch processing of the images by software enhancement. An x-ray edge absorption technique was also developed to provide an independent measure of total shell dopant content. These developments are discussed below.

4.1.1.1. Beryllium Capsule Coating Developments for NIF Targets. Beryllium is the baseline material for the capsule ablator for the National Ignition Facility (NIF) target due to its relative high density and low x-ray opacity. Be capsules are fabricated using a magnetron sputtering technique. In

order for NIF to attempt inertial confinement fusion, there are a number of specifications for the Be capsule. These specifications include surface data, chemical composition data and dimensional data. One of the challenges is to produce gas retentive capsules, which meet all the requirements.

In our previous investigations, we have found that gas retentive shells can be produced reliably and reproducibly using ion-assisted magnetron sputtering. This process ensures ion bombardment of the substrate. The energetic species attracted to the substrate will deposit energies to the substrate and modify the film microstructures, which lead to gas retentive capsules with half-lives of well above the 7 day specification.

The advantage of ion-assisted deposition to produce gas retentive shells is reliability. Figure 4-1 shows a plot of the D_2 gas retention half-lives of the shells versus substrate biasing. The plot shows that at -80V biasing across the substrate, gas retentive shells can be produced reliably. However, since deposition is carried out in an Ar environment, the process of attracting energetic species to the surface also introduced excessive Ar to the film. In the NIF specifications, there is an explicit requirement for Ar incorporation in the film. The allowable Ar concentration in the film is 0.25 ± 0.1 at.%. In a typical coating, Ar incorporation varies with thickness and the highest level can reach 1.5 at. %.

To fabricate Be capsules meeting NIF specifications, we have to reduce the Ar incorporation and still maintain gas tight capsules. By varying the deposition conditions, the argon content can be reduced while maintaining the gas retentiveness of the capsules as shown in Fig. 4-2.

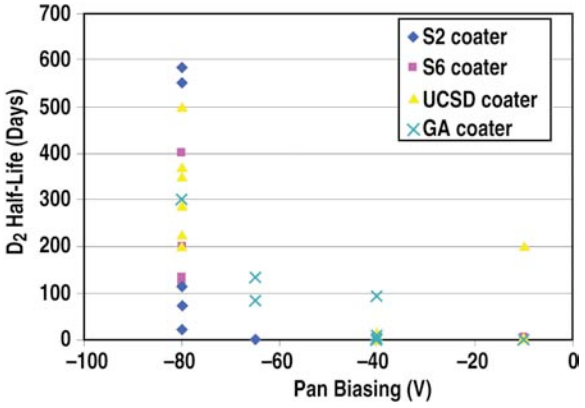

Fig. 4-1. A plot of D_2 gas retention half-lives versus substrate biasing. The reliable gas retentive shells are produced at -80V substrate biasing.

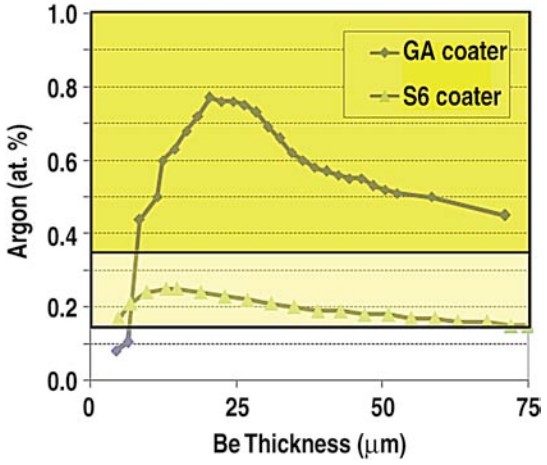

Fig. 4-2. A plot of Ar distribution in a shell coated using ion assist in different coater configurations. Using the proper configuration, argon level is within specification of ~0.25 ± 0.1 at%. When ion assist is not used, the argon level is very low (below 0.1 at%) but the shells do not retain gas.

4.1.1.2. Beryllium Shell Laser Drilling. In FY2008, we have further optimized the beryllium shell laser drilling parameters by decreasing the total laser drilling energy used by a factor of ~21 – from ~113 to ~5.4 mJ. It can approximated that the theoretical lower threshold of laser energy needed (vaporization energy only) to remove material to form a ~5.4 μm cylindrical hole in a full-thickness Be capsule is ~0.27 mJ. This reduction is significant since excessive laser energy can lead to microstructural changes in the parent material surrounding the hole. This present 5.4 mJ is only 20 times the theoretical minimum which is an excellent achievement in such a small, high aspect, hole.

A problem that can occur when laser drilling metals with a nanosecond laser is material redepositing on the sample surface which forms a crown-like structure around the circumference of the hole entrance. We have observed these crowns projecting up to 40 μm above the sample surface in the worst cases. We have developed a technique to eliminate this debris through the use of sacrificial foils.

A capsule holding apparatus was engineered to stretch a thin foil over the apex of a capsule during laser drilling. Using this technique, material is redeposited on the surface of the foil and can subsequently be peeled off after laser drilling leaving a clean hole entrance on the capsule surface. Several foils with varying thicknesses were tested during process development of which we found 9 μm silver foil to work best.

We have developed a process to produce counterbores with entrance diameters ranging from ~15–60 μm and depths of up to ~60 μm, drilled over a fill-hole with mass deficit less than NIC specs.

Laser drilling a counterbore is a two-step in-situ process utilizing the percussion drilling technique. Figure 4-3 shows an x-ray image of such a counterbore. The parameters used for a NIC specification counterbore are as follows: (1) the counterbore is drilled first using 30 double-pulse shots with an energy of 92.5 mJ/pulse pair, with ~80% of the energy in the first pulse and ~20% in the second pulse; 2) the through-hole is then drilled using 150 double-pulse shots with an energy of 22.5 mJ/pulse pair, with equal energies in each pulse. The double-pulse energy described in step 1) of the counterbore process is split 80/20 as it was found empirically that material redeposition, or slag, was inhibited on the bore walls near the counterbore entrance using this energy ratio. We postulate that the strong primary pulse in the counterboring shots produces a relatively energetic ablation plasma that leads to strong radial ablation.

Consequently, counterbore diameters can be controlled by altering the laser power setting, depth can be controlled by altering the exposure energy. Experiments have shown that counterbore diameters and depths can be controlled to a tolerance of ± 2 μm for capsules fabricated with similar layers of dopants and beryllium densities. Figure 4-4 shows the repeatability of counterbore diameters in capsules drilled to date. The three different subsets of data represent similar laser drilling parameters that were used during the ongoing development phase. Greater than 90% of the dimensions in each subset fall within a ± 2 μm range.

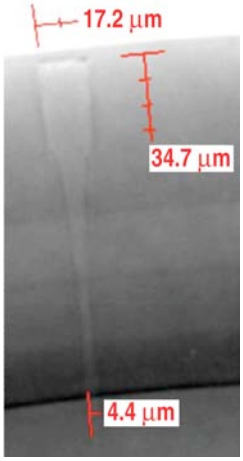

Fig. 4-3. X-ray image of laser drilled counterbore hole in beryllium capsule.

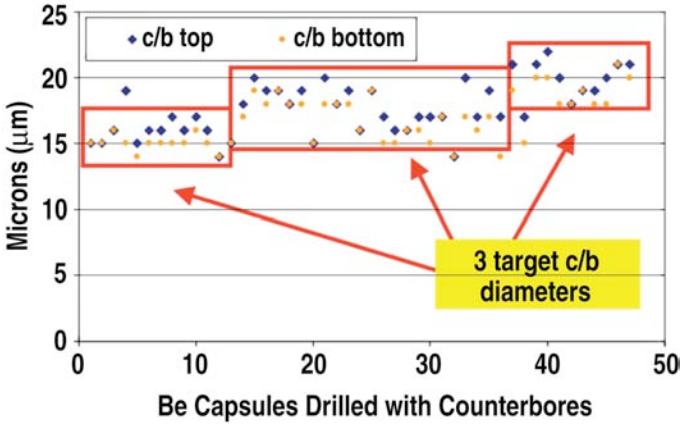

Fig. 4-4. Repeatability of counterbore diameters is shown by three different subsets of data representing similar laser drilling parameters. Greater than 90% of the dimensions in each subset fall within a ± 2 μm range.

4.1.1.3. Scale-Up and Current Yields of Germanium-Doped CH Capsule Production. We made initial attempts to scale-up the production of Ge-doped CH capsules. We were aiming for NIF-quality capsules and focusing on reproducibility and defining yields. Eight batches with batch sizes of 15, 24, 36, 40, 43, 46, 54, and 57 mandrels were made using rotation agitation to evaluate our production setting. Individual NIF specification yields as well as the overall yield (i.e., meeting all NIF specifications) were examined.

The NIF specifications have been modified from Rev. 2 to Rev. 3.1 in May 2008. Batches made before June 2008 were aimed to meet Rev.2 specification and batches made after June were aimed for Rev. 3.1 specification and SymCaps scale 0.9 and 1.07 design.

Nanometer-height domes appeared on capsule surfaces when the batch size was more than 20 capsules and the wall thickness was more than 70 μm (Fig. 4-5). Many nm-sized seeds and micrometer-sized beads were also observed on the capsule surface under SEM. This appearance of nm-height domes is often associated with static-charge-like behavior.

The dome formation mechanism was attributed to be abrasion of capsules in the middle of the coater pan under the weight of surrounding capsules leading to nm-sized seed formation from which domes started to grow. The odds of forming abraded, nm-beads increased with batch size due to a greater tendency of capsules to slip and slide, adding friction to the rolling. Limiting batch size to 15 capsules after the third layer reduced the chance of nm-height dome formation. Four batches and a total of 154 capsules were made using the "sub-batch" approach for surface reproducibility and yield evaluation. Approximately 80% of capsules from 15-shell batches met the NIF surface smoothness specification characterized by AFM (atomic force microscope). In addition, 85% of the capsules also met the isolated defect specification characterized by the PSDI.

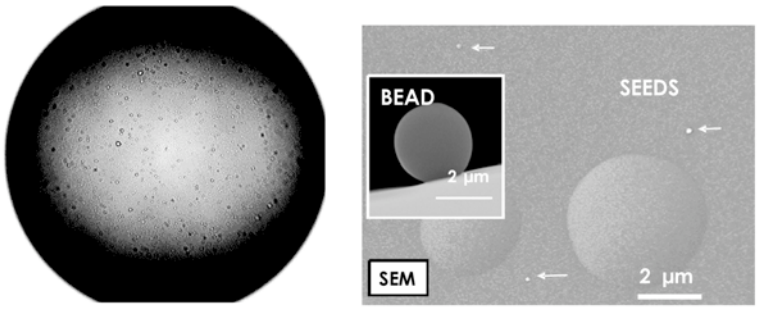

Fig. 4-5. (a) Tiny domes appear on the surfaces of NIF-size capsules for batch sizes of more than 20 capsules and thicknesses of greater than 70 μm. (b) Micron-size beads and nm-size seeds were observed on capsule surfaces after capsules started to slide. Round beads and seeds form by prolonged rolling of abraded surface patches.

Of the few inner surfaces scanned to date with the PSDI, the scans show that the inner surface met the surface roughness specification in high modes (>100). The inner smoothness of CH capsules is also an imprint of the outer smoothness of the mandrel used. The mandrel batches selected for capsule production have power spectra one order of magnitude below the NIF inner surface standard.

The yields of the first layer, the second layer, the third layer and wall thicknesses are 100%, 88%, 100% and 58%, respectively. Most out-of-specification capsules are ~2–3 μm too thick. It was later found that in a rolling agitation each capsule's layer thickness is related to its mandrel diameter, since smaller capsules move toward the coater edge where coating rate is lower. These findings led to sampling two shells out of a batch, one shell from the center and the other shell from the outer edge. This coating interruption sampling was done in order to determine the average wall thickness and fine-tune the remaining coating time. Since then, the yield of targets meeting the wall thickness specification has improved to near 100%. However, pyrolysis shrinkage (4±1%) will also introduce a variation in the wall thickness of ~2 μm.

Previously, cryogenic thermal shrinkage was not added to the outer diameter (OD) specification and 40% of the capsules met the OD specification. If linear thermal shrinkage of 1.27% from room temperature to cryogenic temperature is taken into consideration, the yield becomes 28% at cryogenic temperature. The current mandrel diameter selection has factored in thermal shrinkage at cryogenic temperature. However, the outer diameter yield is affected by available mandrel diameters and its spread. A typical mandrel batch diameter has a standard deviation of ±10 μm and a range of ±20 μm. Therefore, mandrels have to be culled to a narrower range before CH coating for OD yield improvement. Capsule diameter is also influenced by pyrolysis shrinkage variations. A 1% shrinkage variation in a 2 mm capsule would give rise to ~20 μm variation in the final capsule diameter.

The germanium layers in the CH coatings have been well defined in the NIF specification. The two different designs that were explored in the last year are Rev. 2 (target: 0.8 and 0.4 Ge at.% layers) and Rev 3.1 (target: 0.6 and 0.3 Ge at.% layers). Fabrication of Rev. 2 CH capsules have produced average values in the germanium layers of 0.77 ± 0.15 and 0.50 ± 0.13 at.%, respectively. However, both layers had spreads of ~0.48 at.%, which lead to a 13% yield (Rev. 2; ± 0.1 at.% tolerance) or if we compare to Rev 3.1 specification a 50% yield (Rev.3; ± 0.2 at.%). The low yield is due to the inability of the capillary flow element and differential pressure transducer to consistently maintain

zero or stable flow levels at 0.04 and 0.08 sccm (standard cubic centimeter per minute). The capillary flow control was replaced with a 0.2 sccm full-scale mass flow controller and the Ge-doping accuracy has greatly improved. The 9 batches for Rev. 3.1 specification runs had an average and standard deviation of 0.55 ± 0.06 at.% and 0.34 ± 0.04 at.% (target 0.6 at.% and 0.3 at.%) (Fig. 4-6). The yields of both Ge layers are 100% (± 0.2 at.%). The standard deviations are now half as compared to before the replacement of the flow controller.

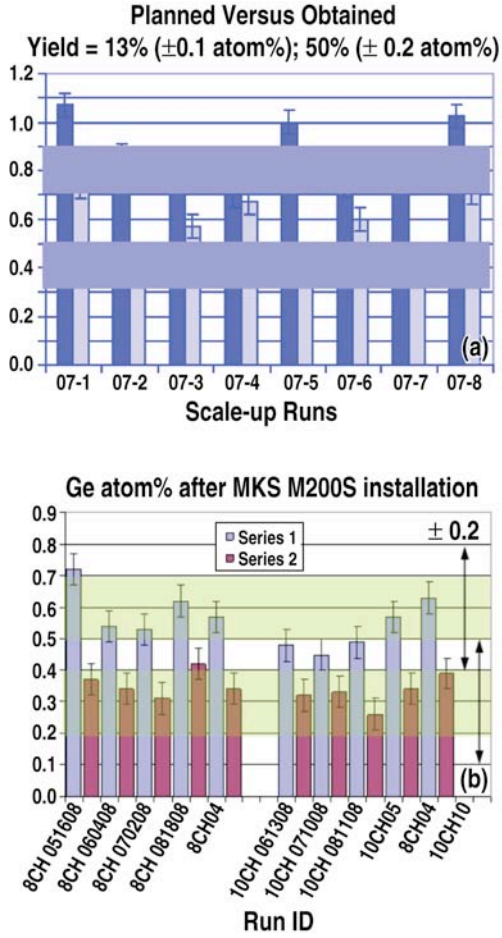

Fig. 4-6. Ge-doping levels of eight scale-up batches (07-1 to 07-8) shown in column plot. The precision of contact radiograph measurement is ± 0.05 at.%. Each dark-light column pair represents two Ge-doped layers in a batch. The dark-colored columns aimed for 0.8 Ge at.%, and the light-colored columns targets 0.4 at.% (a) or 0.6 and 0.3 at.% (b). Previously one batch meets both layers when tolerance is ± 0.1 at.%, and four batches meet both layers if tolerance is relaxed to ± 0.2 at.%. Since replacement of the low-flow mass flow controller, all batches are within ± 0.2 at.% of Rev. 3.1 specification.

Overall scale-up yield is 14% (i.e., meeting all NIF specifications) which is dominated by the low yields of Ge doping accuracy (Fig. 4-7). When a batch does meet both Ge doping levels, the overall yields of 15 shell batches are ~40%–50% which is limited by the wall thickness accuracy and high mid-modes roughness in AFM power spectra. Mid-modes of the capsule can only be improved by removing the large shallow depressions on the mandrel surface.

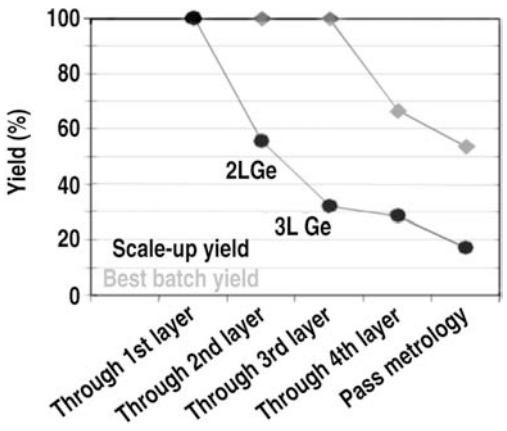

Fig. 4-7. The overall scale-up batch yield drops in the second and the third layer due to lack of Ge doping accuracy. The best batch has correct Ge doping levels. The drop of the yield in the best batch is due to over-coating at fourth layer, high mid-modes in AFM power spectra.

4.1.1.4. Capsule Fill Tube Assembly (CFTA). FY08 saw major improvement in the NIC subassembly area including CFTAs. CFTA production was transferred to General Atomics at the end of calendar year 2007. Throughout 2007, we had worked on the research and development of producing a CFTA. We were concerned with making the assembly a robust process and determining validation techniques. By the beginning of 2008, most of the techniques were in place. The rest of 2008 included increasing our capacities and meeting the NIC specification.

The NIC specification requires the adhesive fillet volume between the capsule and fill tube to be < 2.5 ng. We embarked on an experiment to reduce the adhesive fillet volume; current volumes were 30–50 ng at the time. This led to assemblies that were leak tight and had high integrity, yet they did not have a noticeable fillet extending beyond the outer diameter of the capsule, effectively a 0 ng fillet volume. In experimental testing with the Instron at Lawrence Livermore Laboratory, and with the assistance of Suhas Bhandarkar, we determined that CFTAs without a noticeable fillet were approximately 80% as strong as “bulky” fillets (around 30–50 ng). Most CFTA failures had occurred due to poor handling techniques that led to a massive failure that even a bulky fillet could not withstand. Therefore, we deemed these results acceptable.

The material of the fill tube in the CFTA was borosilicate glass made by Humagen. This material type was chosen due to its strength and flexibility properties. Due to needing a specific material type, the need for a tube-tube subassembly arose. The tube-tube subassembly specifications were determined throughout the course of the year due to target physics and dimensional requirements. The tube-tube subassembly process was tested, validated, and ultimately recorded in an ISO procedure by the year’s end.

Final assembly of the target at LLNL was made easier due to the on-time and consistent deliveries of the CFTA. Both CH and Be CFTAs were made to meet the demand. The CFTA did not contribute to any target failures in 2008 that could have been prevented in the subassembly process. If the CFTA failed during final assembly it was due to a final assembly mishap that put undue stress on the CFTA to cause failure. We produced approximately 100 CFTAs in FY08 with a yield of ~60%.

4.1.1.5. X-ray Absorption Spectroscopy for ICF Target Characterization. NIF targets not only have complex geometries and layered dopant compositions, but also impurities [4-1]. The NIF point-design ablator capsules are 2 mm shells with five beryllium layers doped with different atomic percent of copper. X-ray Absorption Spectroscopy (XAS) is used to supplement the profiling techniques that have been developed [Contact Radiography (CR), Differential Radiography (DR), and Energy Dispersive Spectroscopy (EDS)]. As it is a bulk method, XAS measures the areal density of each element accurately, without a need for a calibration standard.

In materials research that requires high sensitivity to the sample structures and compositions, XAS is often associated with a large synchrotron source with high intensity and highly collimated beams. In our project, however, there is no need to distinguish between the pre-edge, near edge, and extended fine structures in typical XAS analysis. Our main goal is to ascertain the presence of an elemental content to ~0.05 at.%. For this purpose, it suffices to analyze the general transition of the transmitted x-ray spectrum in the vicinity of an absorption edge. We developed a simplified version of XAS that uses a table-top x-ray source, a silicon detector, and dedicated software that makes it efficient in analyzing NIF scale samples.

This method utilizes the existing asset of a contact radiography system [4-2, 4-3]. As shown in Fig. 4-8, the ablator shell sits on top of an aperture within a holder mounted on the x-ray detector. (The detector in turn is mounted inside the contact radiography vacuum chamber.) The tungsten aperture has a 300 μm hole and a tapered front surface to self-center a NIF scale shell. Different apertures can be used for different shell sizes and for other (such as flat) samples. A tungsten-anode x-ray source is located 80 cm away from the holder. The x-rays go through two walls of the capsule in a nearly parallel beam, and the transmitted photon spectrum is measured by a XR100CR x-ray detector (by Amptek Inc. with a 160 eV FWHM resolution) [4-4]. To avoid detector saturation, the current is adjusted at a specific voltage to give a count rate of ~4000 counts/s for a given shell. The transmitted photon spectrum is acquired for 5 to 20 minutes to minimize statistical noise.

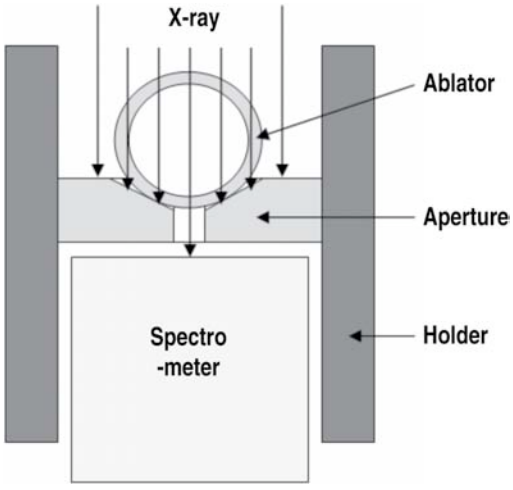

Fig. 4-8. The experimental XAS apparatus.

The measurement theory is very straightforward. It is based on the exponential attenuation of x-rays in a sample. For a given photon energy and a given element *i*,

$$(I/I_0)_i = \exp\left[-\left(\mu_i/\rho_i\right)\rho_i t\right] \quad , \tag{1}$$

where I_0 is the incident intensity and I is the transmitted intensity. The x-ray absorption of each element is independent of the other elements and the effect is cumulative.

$$I/I_0 = \prod_i (I/I_0)_i \tag{2}$$

Therefore, Eq. (1) can be rewritten as

$$I/I_0 = \prod_i \exp\left[-(\mu_i/\rho_i)(\rho_i t)\right] \tag{3}$$

The attenuation model is based on the element attenuation constant, m_i/r_i from the Lawrence Berkeley National Laboratory on-line x-ray database compiled by Henke *et al.* [4-5]. The same database is also used for contact radiography modeling [4-2, 4-3]. Because each element has distinctively different absorption edges, the areal densities of multiple elements in the same sample can be obtained simultaneously as long as there are sufficient counts to resolve the absorption edge. The areal density of all elements heavier than z = 17 can be measured to ± 3% 1 sigma accuracy. For beryllium samples, we record transmitted photon spectra at both 7 and 20 keV for sensitivity to argon and copper respectively.

The same methodology, in principle, can be applied to even lower z elements but the experimental set-up would have to be improved to provide a larger flux at lower energies. The current system uses an x-ray tube with a 127 μm thick beryllium window which absorbs almost all photons with energy below 1500 eV. The vacuum system with 5×10^{-3} Torr base pressure is not equipped to support open cathode x-ray tubes.

XAS for use with ICF targets has been validated by benchmarking with metal foils. The areal density of thin metal foils from Goodfellow [4-6] with a typical 99.9+% purity was determined independently through the measurements of the weight and the foil area.

$$\begin{aligned} \rho_i &= M/(A*t) \\ \rho_i t &= M/A \end{aligned} \tag{4}$$

Through the use of a microbalance to weigh the sample to ~1 μg and measuring a large sample to minimize area uncertainty, it was found that the areal density can be determined to below 1%. The foil uniformity is proven by comparing the areal density of multiple smaller samples cut from a larger piece. Using this information, XAS can be proven to accurately measure the areal density to ± 3% when compared against the foil standards. Figure 4-9 shows the validation on copper foils from 1 to 10 μm pertinent to capsule measurement. The 1:1 slope proves there is no other physical phenomenon affecting the experiment, which establishes the measurement accuracy. The measurement sensitivity can be demonstrated one of the two ways: (1) how much areal density change is needed to produce a visible change in the attenuated reference spectrum; (2) if different operators measure the same unknown sample multiple times, how much is the typical difference? Either way, the areal density

sensitivity is ± 0.3 mm•g/cc or 0.03 mm copper foil thickness. In other words, a full thickness NIF capsule can be characterized to ± 3% of the reported value.

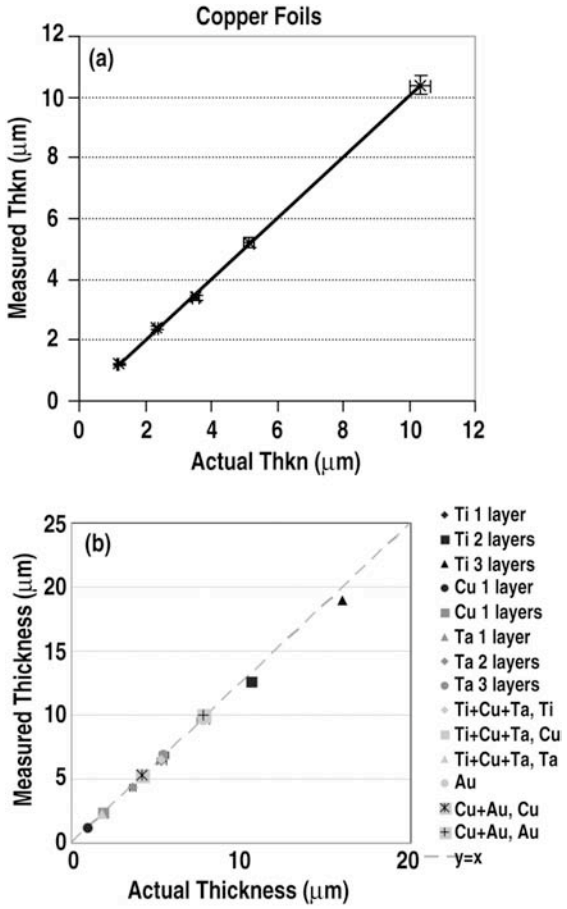

Fig. 4-9. XAS is validated by benchmarking against metal foil standards. (a) Copper foils were used for NIF capsule validation. (b) A mixture of metal foils was used for hohlraum and HED validation.

Direct benchmarking against XRF on PAMS shell permeation filled by argon to 1 atm has also been done. Two identical PAMS shells, with a 2 h decay time, were stored in an argon fill station for 4 days. The shells were retrieved from the fill station simultaneously and immediately loaded into the XRF and XAS chambers. Two operators performed repeated measurements every several minutes over the course of 2 h. As shown in Fig. 4-10, the two sets of argon decay curves are statistically indistinguishable. It is worth noting that, because the argon is uniform inside the shell and PAMS has a perfectly known composition, the shells can be modeled accurately by the "XRFer" program.

One source of systematic error is due to the non-zero aperture size. Unless the x-ray passes through the shell center, the actual x-ray path length is slightly larger than the two-wall thickness. This is a simple geometric effect that can be areal-averaged accurately: On a NIF sized 2 mm diameter shell, a 300 μm diameter aperture would inflate the measured dopant value by 0.6%, and a 400 μm diameter aperture would inflate the measured dopant value by 1.2%. In both cases, we assumed the operator simply uses the two-wall thickness as the x-ray path length without being aware of the distinction.

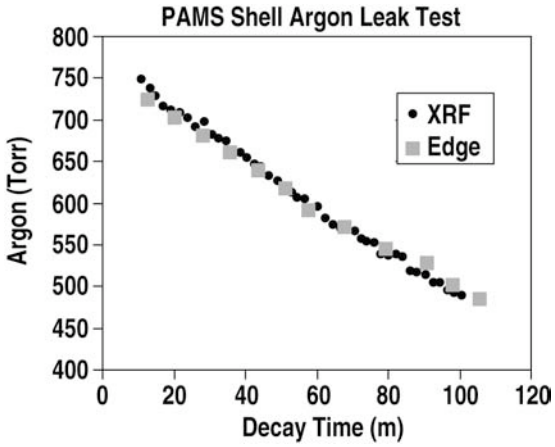

Fig. 4-10. XRF and XAS agree in the leak test of argon-filled PAMS shells.

The insensitivity of XAS to elemental distribution cuts two ways: On the one hand, it improved areal density measurement accuracy by not having the matrix effect. On the other hand, it cannot be used as a profiling technique. In practice, we use it to calibrate profiling methods such as EDS. EDS measures ICF capsules dopant (Be, Ar, Cu) count profiles very well, but it needs a scaling factor to convert into the atomic percent profiles. The missing scaling factor can be determined by requiring the integrated areal density of the argon and copper profiles to be equal to those measured by XAS [4-7]. The consistency between the XAS data and the contact radiography data can also be used to screen for gross measurement error.

Because XAS measures the areal density, the measurement sensitivity in atomic percent scales inversely with the sample thickness. For full thickness shells, we can measure argon and copper averages to ~0.03 at.% accuracy. For half thickness shells, we can measure to ~0.06 at.% accuracy. XAS is not sensitive to trace elements because a concentration below 0.01 at.% does not produce an identifiable absorption edge.

In conclusion, the XAS instrumentation was developed to measure the areal densities of individual elements in a sample without the need for a calibration standard or a concern for the unknown spatial dopant uniformity. The method can identify all elements above Z = 17 and measure the elemental areal densities to ± 3% accuracy. It complements existing tools and has found applications on many ICF and HED samples.

4.1.1.6. Characterization of Isolated Defects for NIF Targets Using PSDI with an Analysis of Shell Flipping Capability. NIF ignition targets demand full shell characterization of isolated defects to determine whether they meet specification (Fig. 4-11) [4-8]. These defects are defined as being elongated ridges or troughs and circular bumps or divots. Previously, the extent of surface mapping involved the atomic force microscopy (AFM), which takes ~40 μm orthogonal traces and is sufficient for low mode surface analysis, but can miss isolated defects (Fig. 4-12). The phase shifting diffraction interferometer (PSDI) apparatus allows for the precise mapping of shell surfaces by examining ~500 μm diameter regions to capture the surface over an entire hemisphere [4-9]. Using capsules with drilled holes for alignment, we compared the equatorial bands from AFM and PSDI measurements for

defect patterns, detectability, and defect height. Characterization capability improved to full shell mapping when a shell flipper was added to the system to precisely transfer a capsule to another chuck to view the opposing hemisphere. This section discusses the application and accuracy of the PSDI with the Shell Flipper, [4-10], defect statistics obtained from the analysis software developed at Lawrence Livermore National Laboratory [4-11], and the automated data processing tool from General Atomics.

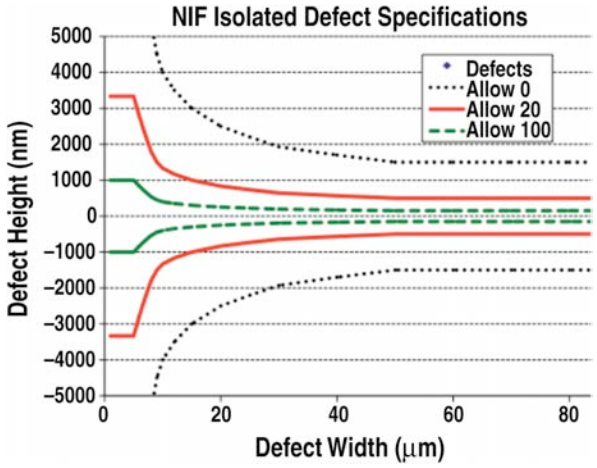

Fig. 4-11. Current NIF specifications for isolated defects on a layered CH or uniform beryllium capsule. Plot extrapolated from Haan [4-8].

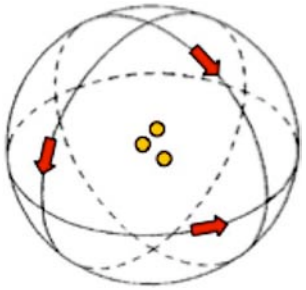

Fig. 4-12. Diagram of AFM traces for low mode analysis can miss large regions of capsule. The arrows show the trace paths and the spots represent defects that can be missed.

The PSDI apparatus utilizes linear and rotary Aerotech stages with 5 axis capability in the x, y, z, θ, and ϕ directions that provide submicron accuracy. The apparatus is controlled by data acquisition software developed by LLNL, which allows for surface mapping of an entire hemisphere [4-12, 4-13]. The PSDI functions by passing a single 532 nm laser beam through a beam splitter, that divides the beam into a reference and measurement beam. These beams are reflected back to the interferometer and undergo constructive and destructive interference. Fringes are captured on a CCD camera. Captured CCD images have a lateral resolution of ~1 μm and height accuracy of ~5 nm peak to valley (P-V) [4-14]. Figure 4-13 depicts how 71 images are acquired to capture surface defects on a hemisphere for analysis.

The PSDI data propagation software "LiteProp" developed at LLNL converts data into a format that can be readily analyzed. This software produces a height map of each image taken by the CCD. These data are plotted against the NIF specification, inspected for anomalous data points, and given a pass or fail determination as a NIF ignition target (Fig. 4-14).

These results revealed limitations of PSDI surface imaging and analysis software that prevent a pass or fail determination. The contribution of unwrapping errors to anomalous defect data are almost always present around larger defects with heights typically greater than 600 nm. In our initial studies with over fifty hemisphere data sets, about 20% of CH NIF shells have at least one defect that cannot be unwrapped. Preliminary studies indicate that unwrapping errors are governed by the Nyquist sampling theorem, which requires the defect slope to be less than a quarter wavelength per pixel for

the measurement to give an accurate height [4-15]. When the defect slope is greater than a quarter wavelength, there are an infinite number of solutions for the height. By reducing the pixel size, we will reduce the height difference between pixels, allowing us to resolve high slope defects.

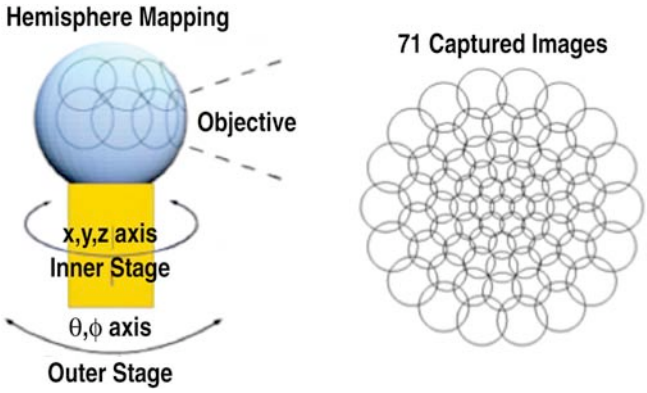

Fig. 4-13. Schematic of hemisphere mapping possible with 5 axis stage to output seventy-one 500 μm diameter images for defect analysis.

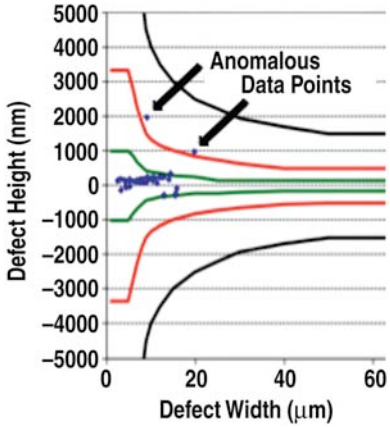

Fig. 4-14. Typical plot generated by defect data extracted from height maps of a NIF ignition target with Labview.

A Wyko optical profiler was used to study "undeterminable by PSDI" defects and provided promising data for quantifying the defects to increase the yield of capsules that can be measured. Figure 4-15 shows a typical unwrapping error and the same defect captured successfully by the Wyko with a 0.75 μm height and 35 μm width. We confirm that the correct defect is being analyzed by optically matching defect patterns around the defect of interest with images from the data processing software.

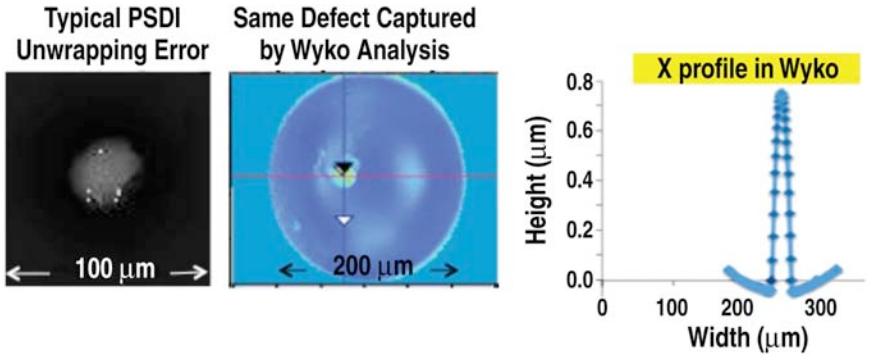

Fig. 4-15. High magnification of a typical unwrapping error on the PSDI successfully captured and measured on the Wyko.

In order to validate PSDI surface data, we mapped the equatorial bands of four shells on the AFM and PSDI and compared the surface defect patterns. The results of this can be found in Ref. [4-16].

The Shell Flipper developed at LLNL increased PSDI mapping to a full sphere by integrating a linear transfer stage, transfer chucks, and a novel pressurized chamber [4-9]. The system isolates the capsule onto the chuck in the chamber and preserves the shell orientation. After data acquisition is

performed for the first hemisphere on the PSDI, the chuck and capsule are tranferred to the receiving chuck (Fig. 4-16). The transfer chuck and receiving chuck are aligned using two orthogonal cameras, a 2X vertical camera view and 5X horizontal camera view. The shell is transferred, or flipped, to the receiving chuck, and the chamber is again used to bring the new shell orientation to the PSDI to map the second hemisphere.

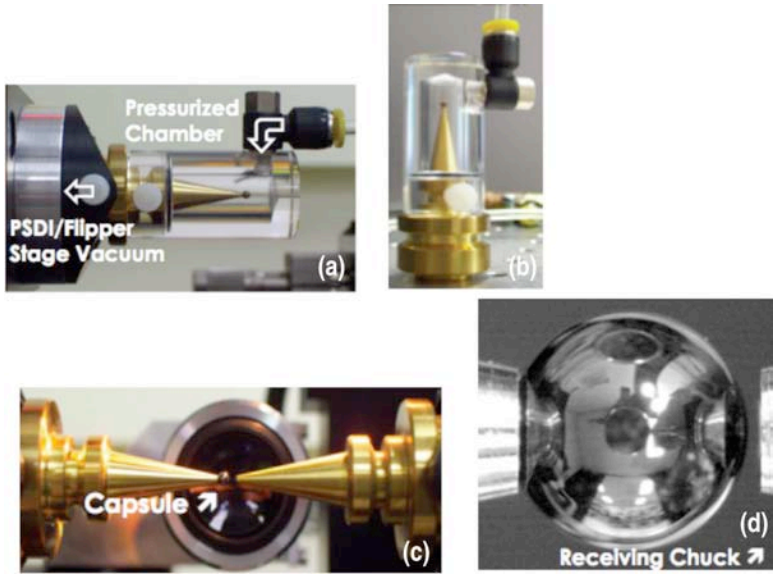

Fig. 4-16. Snapshots of capsule on (a) PSDI stage, (b) N_2 pressurized transfer chamber, (c) PSDI Shell Flipper, and (d) closeup (gravity acts downward in each image).

The Shell Flipper's ability in maintaining the capsule orientation was also studied and showed that the average drift of ~25 μm is the cumulative effect of two flips, during which the marker also underwent ~10 μm non-repeatable random walk.

The cause of the linear drift can be attributed to the non-concentricity between the sending and receiving chucks, and is quantifiable by a calculation from Montesanti [4-17]. Therefore, we expect the single flip error encountered in the normal PSDI measurement would lead to an average ~13 μm orientation shift, which is less than 1° on a NIF scale capsule. Such a small shift does not affect the full surface defect counting and is a factor of ~5 better than manual capsule transfer.

Finally, we improved the process by making data analysis more rapid as this was limiting the data processing rate to one shell per day. LiteProp mentioned above, unwraps the CCD image and filters out low mode information to produce a two dimensional height map [4-11]. Initially a bottleneck, this was a manual process that required individual inspection and focusing of the 71 images for a hemisphere. The software was modified and automated at General Atomics to increase throughput from 15 capsules to 30 capsules a week, necessary for NIF metrology requirements [4-18]. The wave-front propagation algorithm in IGOR Pro 6® from WaveMetrics™, through paraxial propagation along the optical path, generates a phase map and an amplitude map at the capsule surface, which cover a 500 μm diameter area on a NIF capsule. The phase map can be readily converted to a surface height map through a simple correlation, that 2 p equals half a wavelength. The amplitude map is

indicative of the data quality (No measurement can be made if the reflected intensity is zero). Attention was paid to minimizing artifacts: (1) use two soft masks on two stops along the optical path to minimize the concentric ring artifact that would otherwise result from the propagation; (2) remove piston and tilt artifacts due to imperfect alignment, (3) use a high path filter to remove low mode and thereby increase the visibility of localized defects. Through these processes, the useable area of the image is maximized (~80% or 400 μm diameter area within the image) for defect identification purposes, but the low mode (modes < 50) information is lost.

GA improved the propagation codes to allow batch processing of 71 images (one hemisphere) based on the manual focus of the first image. The routine requires the user to focus the first image and save its optical information including the focus distance. Once completion of the initial focusing, the auto batch propagation will search for the rest of the images, then extract the positions of q, f and read the value at each position. Then the data propagation commands of the algorithm described above are executed for each image. The processed data is then saved in windows in ASCII and binary formats. Data from the two hemispheres is then input into the data analysis software described above. The process time for the data propagation of 142 images is reduced from about 3 h to 1.5 h.

At the end of the data propagation step, we obtained 142 surface height maps. Examples of the surface maps are shown in Fig. 4-17. These continuous topological maps are not yet immediately useful because they cannot be benchmarked against the NIF surface roughness and point defect specifications. GA developed automated data analysis software to perform this task.

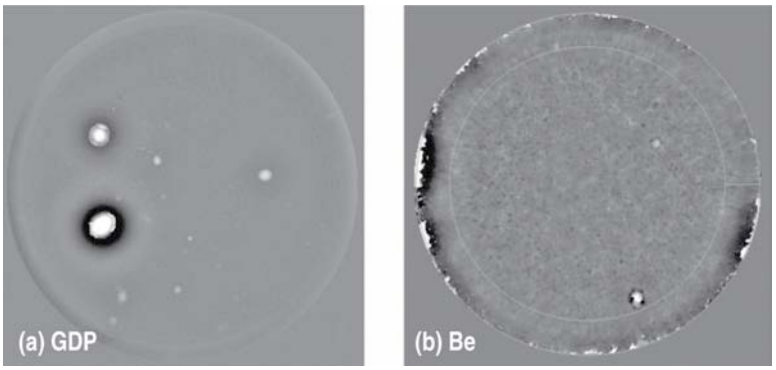

Fig. 4-17. Surface height maps (a) GDP capsule and (b) Be capsule. The automated routine finds the measured area (the larger circle) and quantitatively analyzes the area not affected by the artifacts around the circumference (the smaller circle).

We first developed batch processing software to convert Igor binary height maps into ASCII height maps to interface with LabVIEW Vision software for image analysis. Defect finding procedures must be defined precisely to gather reproducible isolated defects stats. Most image processing software uses a fixed threshold to turn a gray scale image into a binary image, and then uses blob analysis to tabulate localized regions above the threshold. This approach is problematic because the size of the defect is dependent on the threshold level: The lower the threshold, the larger the defect. We used a three step approach to solve this problem: (1) use a global threshold (such as 100 nm) that is low enough to capture all defects of NIF relevancy in binary analysis; (2) Find the

center height of each identified defect; (3) apply a local threshold to each defect with the threshold set to be half the defect height, then perform blob analysis to obtain the defect area above the local threshold, and calculate FWHM based on the area (Fig. 4-18). By comparing defect tabulations using different height thresholds, we experimentally verified that the defect height and FWHM calculated by this method does not have threshold dependency and can be compared directly against the NIF point defect specifications. The surface roughness power spectrum can also be computed and benchmarked against the NIF surface roughness specifications.

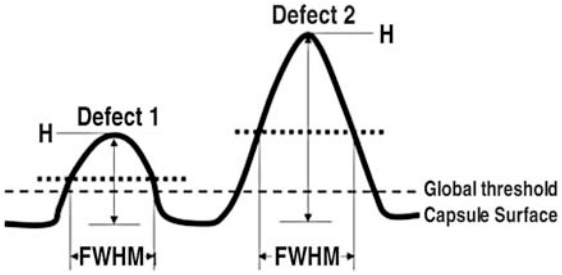

Fig. 4-18. Setting a local threshold at half height on each defect eliminates the threshold dependency in FWHM calculation.

We then automated the data analysis software to batch process all images. As shown in Fig. 4-17(b), the software automatically locks onto the active areas of a height map (the large circle) and performs analysis in the areas less affected by the artifacts near the circumference (the small circle). For most images, 80% radius is a good approximation, which reduces the 500 μm medallion size to 400 μm. The batch process reduces the data processing time from one hour to eight minutes, and tabulates all defects in a summary report that benchmarks against the NIF point defect specifications [Fig. 4-19(a)]. Similarly, the surface roughness is benchmarked against the NIF surface specifications [Fig. 4-19(b)]. The definition for power spectra is the same as for the spheremapper. However, there are two important distinctions: (1) PSDI power spectrum covers the entire capsule surface whereas the Spheremapper power spectrum only covers a few traces. (2) Spheremapper power spectrum measures low modes accurately whereas the PSDI power spectrum below mode 50 is meaningless. For capsules without significant local defects, the PSDI and Spheremapper power spectra have been proven consistent along common equators for modes 50–1000.

In conclusion, PSDI has become an important tool in NIF metrology for surface characterization of CH and Be capsules to qualify targets for NIF ignition experiments. Although the PSDI cannot capture low modes, the defect data extracted from the images are valuable for high mode analysis. Where the PSDI cannot define defects beyond the Nyquist sampling requirement, the Wyko can be used to determine the quality of undeterminable shells. The PSDI complemented with the Shell Flipper has improved performance with only a 1–2° capsule shift observed, experiments are still needed to eliminate orientation shift altogether. Future studies are needed to understand and reduce the unwrapping error events. In addition, studies with the AFM and Wyko are needed to fine-tune PSDI defect statistics and explain the trends. This effort can potentially be applied to identify poor mandrels and coating runs in advance, which can make capsule fabrication more efficient. Due to the limited numerical aperture of the focusing lens, 142 images are needed to cover the capsule surface,

which leads to a throughput bottleneck. Prior to automation, it took 6 h for data acquisition, 5 h for data propagation, and 2 h for data analysis. Only 3 to 4 capsules could be measured per week. Through engineering of the data acquisition hardware, and the development of sophisticated automation software packages in hardware control, wave-front propagation and data analysis, the required times have been cut to 20 min, 90 min and 10 min respectively. As a result, the 20 capsules per week throughput required by the NIF program can now be achieved. Furthermore, the improved software algorithms remove the operator dependence in data analysis and enable the defect and surface statistics to be quantitatively benchmarked against the NIF specifications for production quality control.

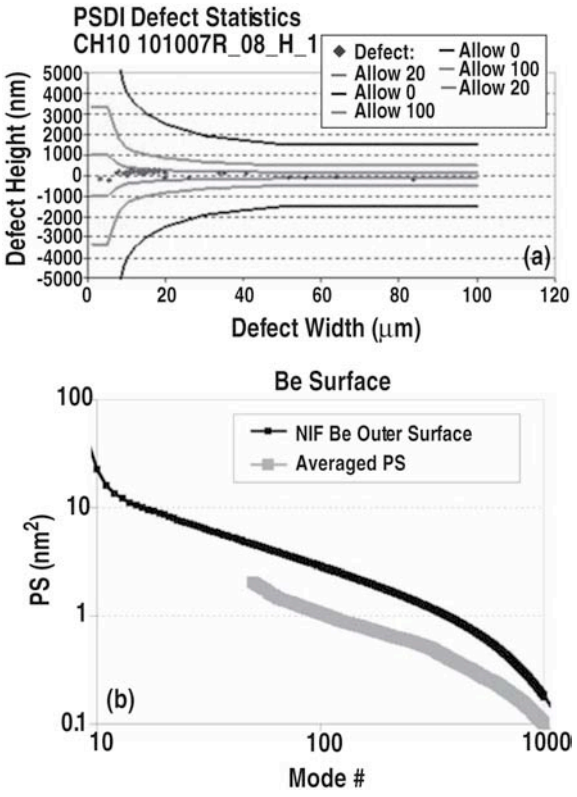

Fig. 4-19. (a) Isolated defect statistics of a CH capsule. (b) Surface roughness power spectrum of a beryllium capsule.

4.1.2. Hohlraum Development and Fabrication

4.1.2.1 Fabrication of AuB-lined Gold and Uranium Hohlraums for the National Ignition Facility. In response to requirements for NIF, a magnetron co-sputtering process has been developed to fabricate AuB liners on the interior of hohlraums made of either gold or depleted uranium (DU). Simulations and an experiment on the OMEGA Laser Facility at the University of Rochester Laboratory for Laser Energetics show that the addition of boron to the gold layer lining the interior of the hohlraum likely reduces laser reflection from this surface by reducing the stimulated Brillouin scattering [4-19, 4-20]. By reducing this backscatter through the laser entrance hole (LEH), the amount of energy that is available to compress the inertial confinement fusion capsule is increased.

Depleted uranium (DU) hohlraums are being routinely fabricated by rotating a hohlraum mold in front of a DU sputter source to build up the desired wall thickness [4-21, 4-22]. The mold is removed to leave a freestanding hohlraum half. Two halves are assembled to complete the hohlraum to specifications. Since DU oxidizes in air as well as in the chemicals required to dissolve the mold from the hohlraum [4-23], the main experimental challenge is to protect the hohlraum from damage. Oxidation leads to unacceptable expansion of the DU lattice, resulting in severe structural damage to the hohlraum. Also, the presence of oxygen increases the ionization heat capacity of the hohlraum wall, effectively canceling the efficiency gains gleaned with the addition of DU to a gold-only wall [4-24, 4-25]. By varying the deposition conditions, much progress has been made in the successful fabrication of hohlraums containing DU, including increased yield as well as an improved shelf-life.

Fusion ignition experiments at the National Ignition Facility (NIF) will be done in the indirect drive configuration during the first few years of operation. In the process of conversion of laser light to the symmetric x-ray drive, energy is lost by penetration of x-rays into the hohlraum wall. To mitigate this loss, calculations show that adding depleted uranium to the traditional gold hohlraum increases the efficiency of the laser to x-ray energy conversion by making the wall more opaque to the x-rays [4-26–4-30]. Previous attempts to produce hohlraums containing uranium were unsuccessful from the point of view of the longevity of the parts. Due to oxidation of uranium, the parts would typically break apart during the leaching of the hohlraum mold, or if it survived that step, would blister, crack, or contort, becoming unusable within a few days of leaching.

During the initial attempts to fabricate hohlraums containing DU, it was observed that after the part was leached from the mold, the material near the laser entrance hole, a flat area facing the sputter sources during deposition, did not degrade at the same rate as the material along the barrel. The flat area would persist unaffected for many months when the barrel of the same part would degrade and begin to disintegrate within weeks. Material purposefully coated onto flat substrates also fared much better over time than similarly coated 3-D substrates, suggesting that the structural stability of DU-coated onto flat substrates was superior. Not only was the material more structurally sound, but the oxygen pickup over time was also less in the flat materials as compared to leached hohlraums [4-21]. Sputtering onto inclined substrates is well studied. In general, as the angle of incidence increases from 90 deg, it is observed that the microstructure of the resulting material changes, tending towards an angular columnar structure [4-31, 4-32], which can lead to voids in the material. The cause for this change is self-shadowing of the material depositing at the substrate growth surface. It is therefore conceivable that the material coated on the curved portion of the hohlraums is morphologically different – and potentially less dense – than that coated on the flatter end cap region, due to the fact that the sputtered material constantly lands at a glancing angle along the circumference of the rotating mandrel.

Knowing the importance of directionality of the depositing material, an ion assisted plasma deposition technique has been adapted for the DU hohlraum deposition process. The general technique, originally developed to fill high aspect ratio trenches in integrated circuits, works by sputtering metal atoms into a high-density plasma to create higher than usual ionized metal flux fractions [4-33]. Subsequent ion energies at the deposition surface are controlled by the low voltage dc bias of the substrate, the electric field from which collimates the metal ions so that they approach the surface at a normal incidence angle, minimizing the effect of shadowing on a 3-D substrate. In

this way the density of the deposited film is maximized, improving the stability of the microstructure and therefore making it more resistant to oxidation by minimizing the presence of internal voids and open grain boundaries.

4.1.2.1.1. Experimental Setup for AuB Deposition. For AuB-lined gold hohlraums, the AuB is deposited onto a rotating copper mandrel by a magnetron co-sputtering process, one hohlraum-half at a time. By varying the sputter rates of each gun, the concentration of the resulting AuB co-mix can be controlled in the as-deposited film. The base pressure prior to film deposition must be less than 1.5×10^{-6} Torr and the coating pressure used is 5 mTorr, maintained with Ar. For the work discussed presently, the Au and B guns were conditioned for 5 min prior to film deposition with shutters covering the targets so no material is deposited on the mandrel. It was later observed that the self-bias of the B gun was found to become steady after an hour at 200 W, meaning that the plasma has not reached a steady-state condition until this amount of time. The base-line production recipe has therefore been updated to include the longer gun conditioning time. The gold gun is conditioned for that entire period so that no boron is deposited on the gold sputter target, to avoid rendering the target non-conducting to the point that the DC gun will not ignite. The part is plasma etched in-situ during the gun conditioning step to remove any oxide from the copper mandrel surface to promote good adhesion. Once the gun conditioning step is complete, the sputter source shutters are opened and the film deposition occurs for a set amount of time, depending on how thick of an AuB layer is required using the known sputter rate. Following AuB deposition a thin (< 0.1 μm) capping layer of Au is deposited over the AuB liner for 2 min. Three mandrels can be separately coated in this way in the same vacuum pump down with the use of a trolley mounted to a slide, the position of which is controlled with a magnetic feed-through. A shield with hinged doors is in place to prevent the sputtered material from coating onto the other mandrels in the set. For AuB-lined gold hohlraums, the AuB deposition step is followed by electroplating and the subsequent processes outlined in Fig. 4-20. AuB-lined DU hohlraums, are made similarly, with the AuB deposition step being done immediately before the DU deposition. The deposition of the AuB and DU layers are done in separate sputter systems.

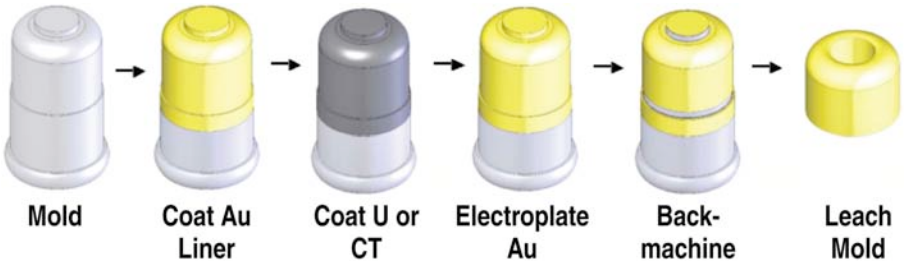

Fig. 4-20. This cartoon outlines the steps to fabricate a hohlraum containing uranium.

4.1.2.1.2. Experimental Setup for DU Deposition. Sputter deposition hohlraums containing DU is done with systems that were custom designed and built at General Atomics [4-19]. The base pressure in the systems is in the low 10^{-7} Torr regime, and the deposition is done with a background Ar pressure of a few mTorr. A residual gas analyzer is run throughout the deposition to monitor water and oxygen levels, which are typically below a partial pressure of nitrogen of $<1 \times 10^{-7}$ Torr. New to

previous work is the introduction of ionized plasma and a dc bias applied to the rotating mandrels used as a mold for the hohlraums.

The fabrication steps are outlined in the cartoons in Fig. 4-20. The molds for the hohlraums, also referred to as mandrels, are diamond turned from Al1100 rod to a surface finish less than 100 nm RMS. A thin (< 2 μm) layer of copper is sputtered onto the Al before DU deposition to promote good adhesion to the mandrel throughout the fabrication process. The U layers are sputtered up to > 7 μm, after which gold is electroplated to a total hohlraum wall thickness of 30 μm. This thickness is calculated at the various fabrication steps by measuring the diameter of the part on the mandrel with a laser interferometer. The uranium and gold is back-machined away at the mid-plane of the hohlraum and at the laser entrance hole (LEH) to the correct dimension of the hohlraum half, after which the Al mandrel is leached out in a 5M solution of NaOH. This leaching step takes up to 24 h. Nitric acid is used to remove the thin Cu liner during a quick etch of < 1 min.

Auger electron spectroscopy (AES) is done in house to characterize the composition and thickness of the AuB liner as well as to measure the amount of oxygen contained in both the AuB and U layers.

4.1.2.1.3. Uranium Hohlraum Longevity and Yield Improvement. Significant improvement has been made in the longevity and yield of hohlraums produced containing uranium by invoking an ion-assisted sputter deposition technique. An example of a part that exceeds the shelf-life requirement is shown in Fig. 4-21(a). Qualitatively the part is completely defect-free when observed under the microscope. The AES depth profile for the same part is shown in Fig. 4-21(b), which shows ~3 relative at.% oxygen in the bulk, which is under the maximum of 5 at.% oxygen allowed in the current NIF point design. The AES depth profile shown in Fig. 4-22 is from a similarly defect-free part, but contains a measurable oxygen uptake (< 20 relative at.%) at the interface of the Au liner and bulk uranium. Because the width of this peak takes up < 7% of the total thickness of the layer containing uranium, the average oxygen content in the bulk uranium is again under the specification for the NIF point design.

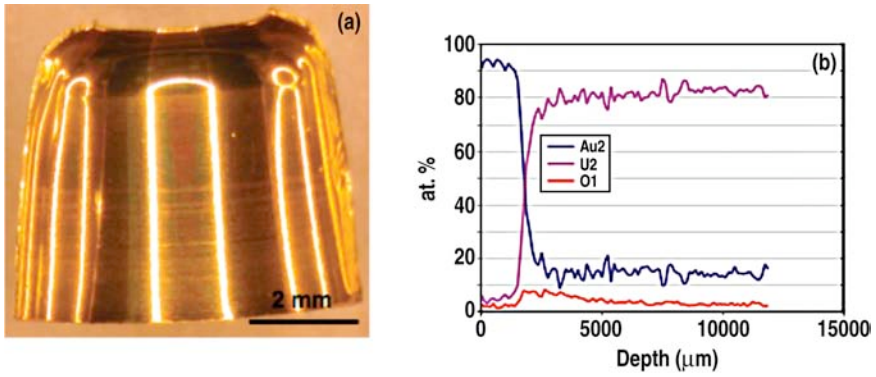

Fig. 4-21. (a) Pictured is a uranium-only hohlraum half cut in half length-wise for AES depth profiling after storage in laboratory air for 4 weeks. The uranium is encased by a 0.2 μm-thick sputtered Au liner on the interior and a thick (>30 μm) electroplated Au exterior overcoat. (b) Plotted is the AES depth profile for the hohlraum half shown in (a). The oxygen content in the bulk U is ~3 at. % relative to U and Au. Note that the Au appears in the bulk of the U because of an overlap of the AES peaks, not because there is any Au present in this layer; the Au sputter source was turned off during the entire deposition time of the U.

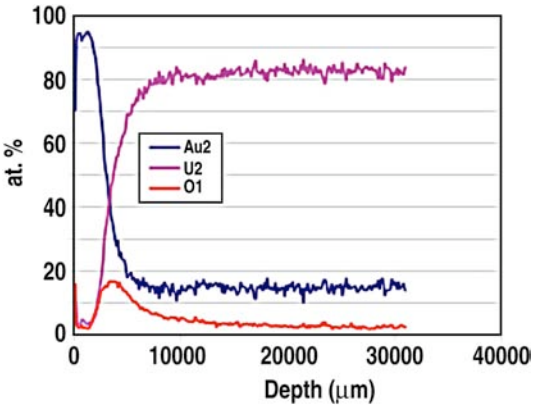

Fig. 4-22. This AES depth profile was made on a hohlraum half that was stored for over 7 weeks in dry air (<2% RH), with a 0.2 μm-thick sputtered Au liner. The part looked pristine on the day that it was cut open for AES analysis.

Because of the improvement in structural stability, we have shown that a variety of different Au liner thicknesses, from 0.5 μm down to 0.1 μm are an effective barrier from oxidation, as shown in Fig. 4-23. It can be seen, however, that a U-only part with no passivating layer has a large oxygen uptake in the bulk compared to the other samples, showing that at least a thin passivating layer is necessary.

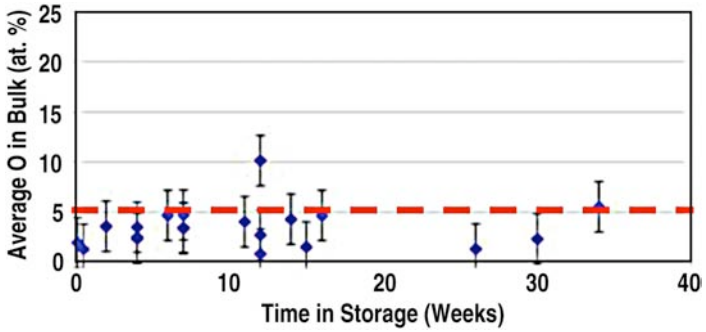

Fig. 4-23. The average atomic percentage of oxygen (O) in the bulk of the U is plotted as a function of the time in storage. The dotted line represents the maximum allowed O level in the bulk.

Before the change in the deposition technique, the yield of hohlraums containing DU that survived the leaching of the mold in an intact state was < 40%. Of those parts, the yield of those that survived the minimum of two weeks required for assembly of the target package was 0%. For uranium-only hohlraums, the yield of intact parts through the leach was 0%. Using ion-assist, the yield of uranium-only parts through the leach is 74%. Work is ongoing to understand why the 26% fail at the leaching step. Of those parts that survive fully intact, 94% survive with no observable degradation for 2 weeks, and 82% last > 4 weeks, with typically degradation being small cracks, bubbles, or blisters, which are on the order of several hundred micron in diameter. Yield on cocktail hohlraums is forthcoming over the next several months.

In conclusion, AuB-lined gold and uranium hohlraums for use on the NIF are being routinely processed to the required specifications. Not only are hohlraums containing DU structurally sound for a long enough time for them to be built and shot on NIF, but are also demonstrating acceptable low levels of oxygen pickup during the leach and subsequent storage. Current and future work concentrates on improving the production capacity and yield, which is currently at 10 hohlraum halves per week with a 44% yield (2 complete hohlraums per week), to levels that will be required for NIF (> 2 shots per day). To this end, an additional DU sputter deposition system is being built, for a total of three systems for NIF production.

4.1.3. Thermomechanical Package Components

The Center for Precision Manufacturing has been working with the National Ignition Campaign and is an integral part in the fabrication of components for the demonstration of laboratory ignition. The center has fabricated all of the R&D prototype components for layering targets, target assembly testing and gluing experiments. The center works in close proximity with the engineers and designers at LLNL responsible for the design of the Thermo Mechanical Package (TMP). The center has dedicated two of its diamond turning lathes and one of its precision mills exclusively for production of TMP components and this included the aluminum shell, diagnostic bands, LEH inserts, window washers and hohlraum machining. Figures 4-24 and 4-25 are photomicrographs of an aluminum shell and a diagnostic band respectively. The good working relationship with LLNL and the dedicated equipment has allowed for quick turn-around of parts when the design changes or when test parts are needed quickly. Recently, with a modification on how holes made by milling are protected from the final diamond turning finishing operation on the parts, the presence of burrs has been completely eliminated. Previously, each part had to be de-burred by hand which was time consuming and there was always the risk of damaging the part. With continuous component fabrication improvements and the TMP design maturing, the center is evolving into a production facility able to produce the hundreds of components per year needed to ensure the success of NIF.

Fig. 4-24. TMP aluminum can.

Fig. 4-25. TMP diagnostic band.

The TMP shell needs to be attached to the proposed Si cooling arms (fabricated at LLNL). This subassembly work is also being done at GA and has been transferred to production mode that was ramped up during 2008. For the first time, subassemblies were produced that used arms which had gold traces to allow connection to heaters and sensors that are also placed on the arms at GA to allow thermal control in the cryogenic implementation of the targets. The silicon arms with gold traces provided an additional challenge to the mere one micron thickness which were susceptible to losing

continuity due to scratching during assembly. Assembly processes were implemented to prevent such scratching that would otherwise lead to faulty subassemblies. The initial challenges of adhering together the components of the subassembly were overcome. We determined which articles would work with the subassembly in the curing process and which articles would not.

The first of a kind tooling for the TMP subassembly process had to be designed and manufactured. The tooling requirements included meeting specifications for concentricity between the inner diameter of the silicon arm and the outer diameter of the aluminum can, and the bond line thickness between the silicon arm pads and the aluminum can flange. The concentricity specification was met due to changing the design of the target to an interference fit. Much of the year was spent determining how to accurately measure the bond line thickness. The difficulty of this measurement was compounded by the inaccurate measurements of the silicon arm thickness as received from the production facility and high-error methods of measuring the bond line thickness post-production. Experiments later validated the new tooling design with respect to bond line thickness by showing a reduction in ice-layer asymmetry.

The final assembly team changed target designs often and—many times—late in the assembly process. Due to the flexibility of the TMP subassembly team, the end user was still able to meet all deadlines and milestones. All orders were delivered on-time and as-requested by the end user. The subassembly team had the opportunity to make 0.7 scale subassemblies, PIL subassemblies, and 1.0 scale subassemblies throughout the course of the year. By the year's end, the subassembly process was documented in an ISO procedure.

4.1.4. The NIF Cryogenic Target System

General Atomics personnel assigned onsite at LLNL are participating in the design and implementation of the NIF Cryogenic Target system (CTS), as shown in Fig. 4-26. This work is under the direction and management of LLNL staff, and is part of the National Ignition Campaign [4-34, 4-35].

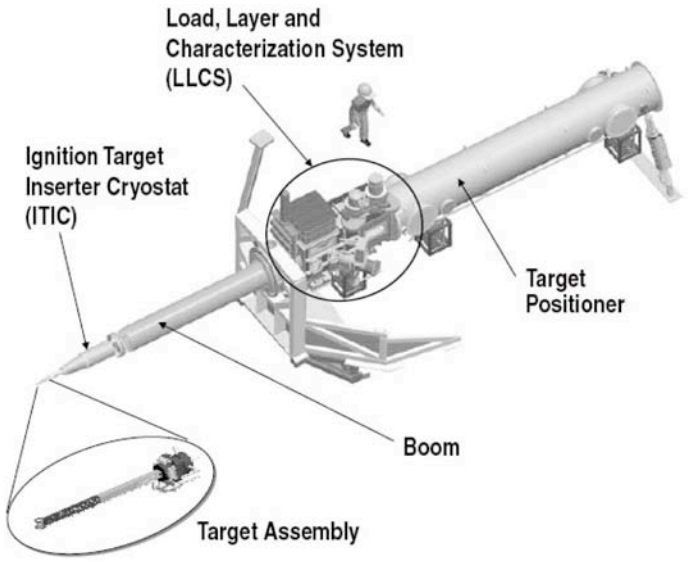

Fig. 4-26. The Cryogenic Target System provides the systems necessary to cool, characterize, and position the NIF ignition target.

The process begins when the target assembly is delivered to the NIF with its target base reservoir filled with DT fuel. The target assembly is first mounted to the end of a target positioner which sits just outside the NIF target chamber. After mounting the target, the positioner vessel is pumped to high vacuum and the cryogenic system begins to cool the target.

During cool down, temperature differentials are used to drive the DT fuel from the reservoir into the capsule. Once the capsule is filled, further cooling begins to form the fuel ice layer. The processes of fuel transfer and ice layer formation are monitored with three axes of x-ray imaging. During these steps, the target remains just outside the NIF target chamber in the high vacuum environment of the CTS.

After the DT ice meets the smoothness specification, the CTS boom extends the target into the NIF target chamber. Near target chamber center, the Target Alignment System (TAS) provides feedback for positioning of the target. The TAS can also image the NIF alignment laser beams and is used to align all beams to the upper and lower hohlraum windows. After the shot, the boom is retracted, the spent target is removed, and the CTS is readied for the next shot cycle.

The NIF Cryogenic Target System can be divided up into three subsystems: 1) the Target Positioning System, 2) the DT Ice Layer Imaging System, and 3) the Cryogenic System.

The CTS positioner is based on the existing and proven NIF room temperature target positioner and is used to place the target at the center of the 10 m diameter spherical NIF target chamber. The body of the positioner consists of a 304 stainless steel cylindrical vacuum vessel. Inside the vacuum vessel is a 0.5 m diameter by 7 m long low coefficient of thermal expansion carbon composite boom that rides on linear rails. The CTS positioner design incorporates five degrees of freedom to adjust the position of the target. The target's position along its axis is controlled by adjusting the stroke of the boom along the rails. The two transverse directions are adjusted by lengthening or shortening the struts that support the rear of the vacuum chamber. Two rotations of the nose cone, roll and nod, are adjusted by a geared mechanism at the end of the boom.

The error budget for laser-on-target positioning has allocated 7 μm rms to positioning of the target. The existing room temperature target positioner has demonstrated the ability to meet this requirement. The primary source of positioning error is vibration, which has been measured using accelerometers to be < 1.5 μm rms. Target positioning with the CTS will more fully utilize the 7 μm rms budget. The cryogenic system is designed to eliminate cryocooler vibration so that the CTS positioner vibration component should be nearly identical to that of the room temperature target positioner. The remainder of the positioning error budget, approximately 5 μm, is allocated to longer term drift primarily caused by imperfect control of the temperature of both the positioner and surrounding equipment.

The CTS positioner also holds the target during DT fuel ice layer formation. The stability required is dictated by ice layer characterization requirements and the x-ray imaging system. The stability requirement is ± 1 μm during the 6 s x-ray image frame integration time. Measurements made on the existing warm target positioner with the boom retracted, as it will be during ice layer characterization, are just above this requirement. To insure the CTS design can meet this requirement, the positioner design was augmented with stabilizers that can be used with the boom in the retracted

position. These stabilizers extend from the vacuum vessel inward and clamp on the end of the boom, effectively locking the two objects together.

The CTS design also includes a component called the Load, Layer and Characterization System (LLCS). As its name implies, this system is used to load the target into the CTS, to provide the environment for the DT ice to form a smooth layer, and to characterize the quality of the layer.

The LLCS vessel is a rectangular box 1.2 m tall by 0.8 m wide by 2.1 m long. It was fabricated using 304 stainless steel and has been electropolished to enhance tritium cleanup. The vessel operates as a vacuum vessel during cryogenic operation and characterization of the target. During installation or removal of a target, the vessel can be operated as a glovebox. In this mode, the operators work through gloveports, which include integral gate valves. During major maintenance operations, the vessel side door is opened and the vessel functions as a fume hood.

The purpose of the LLCS characterization equipment is to measure the smoothness and uniformity of the DT ice layer inside the spherical capsule. The ideal arrangement would be to image the ice layer from a large number of different orientations around the capsule. Since the capsule is inside a cylindrical hohlraum, however, it is only possible to image the capsule along three orthogonal axes. Two axes are horizontal through slits in the hohlraum wall and one axis is vertical through the circular laser entrance holes. The imaging of the DT ice layer is performed using the phase-contrast x-ray imaging technique [4-36]. Each imaging axis incorporates a microfocus x-ray source in close proximity to the target. Since these x-ray devices are designed to operate in air, each source is enclosed in an air box. All three air boxes are arranged on a single strongback that can be raised up to allow the boom to stroke into the NIF target chamber. X-ray CCD cameras are used to collect the image and are positioned to give an 11X magnification of the capsule. The CCD cameras are located outside the LLCS vacuum vessel and hence the x-rays must pass through the vacuum vessel wall. In both this location and in the x-ray source air boxes, the x-rays cross the pressure boundary through beryllium windows.

The CTS design also incorporates a cryogenic system called the Ignition Target Inserter Cryostat (ITIC), shown in Fig. 4-27, to cool the target. The ITIC is mounted at the end of the 7 m long boom using a kinematic mount. The ITIC employs a Gifford-McHahon cryocooler to cool the target base to temperatures as low as 7 K. Multiple control points, consisting of pairs of temperature sensors and heaters, are used to control the target hohlraum temperature as specified (~18 K) with 1 mK precision.

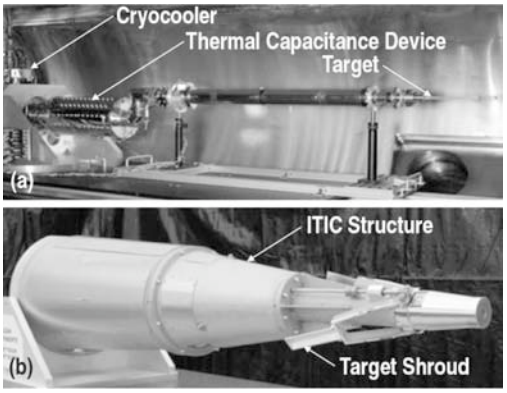

Fig. 4-27. The Ignition Target Inserter Cryostat (ITIC) cryogenic system (a) is assembled into the ITIC structure (b).

The ITIC provides cryogenic temperature control of the target while ensuring that all structure influencing target position is maintained at room temperature. Figure 4-27(a), shows a prototype of the cryogenic system. It consists of the cryocooler (left edge), connected to the cryogenic thermal capacitance device, followed by a coaxial structure reaching to the target base (right). The inner most conductive path, called the cold rod, is connected to the second stage of the cryocooler and operates near 4 K. Surrounding the cold rod is a 60 K thermal shield which limits heat transfer to the cold rod and is connected to the first stage of the cryocooler. Surrounding the 60 K cold shield is a warm shield that is controlled to 293 K using heaters. The cold rod, cold shield and warm shield are all fabricated using oxygen-free high-conductivity copper and are gold plated to reduce radiation heat transfer. The ITIC cryogenic system [Fig. 4-27(a)], is packaged into the ITIC structure [Fig. 4-27(b)]. The structure was fabricated from 6061 aluminum and has a conical geometry with a length of 2 m and a base diameter of 0.5 m.

Ignition targets are installed on the ITIC gripper at room temperature by operators working through the glove box ports integrated into the LLCS vessel. The target is then surrounded by a two layer thermal shroud. The inner layer of the shroud is thermally connected to the cold shield and operates at approximately 80 K. The purpose of the inner shroud is to minimize both thermal radiation and condensation on the target [4-37]. To minimize cooling of nearby equipment, the outer layer is controlled to 293 K. The shroud opens in a clamshell manner a few seconds before the shot to expose the target to the laser. Structural analysis and laboratory tests have been performed to ensure that the vibration imparted by the opening of the shroud will damp down to acceptable values before the shot.

A common challenge when using mechanical coolers in precision applications is the significant vibration disturbance caused by the pulsed nature of the Gifford-McHahon design. The NIF cryogenic target positioner has overcome this problem by utilizing a thermal capacitance device [4-37] that permits the cryocooler to be turned off during periods requiring positioning stability. X-ray imaging of the ice presents the most difficult challenge. An x-ray image is constructed from a series of 20 frames, each requiring 6 s of image integration time. The cryogenic system must maintain target temperature within ±1 mK with the cryocooler off for the duration of the x-ray imaging time. This is a difficult challenge since most engineering materials lose almost all of their heat capacity at temperatures below 100 K. The ITIC cryogenic system uses the thermal capacitance of high-pressure helium at cryogenic temperatures. The helium is confined in a copper structure that minimizes the heat transfer time constant by assuring that all helium is within a few millimeters of a copper conduction path. Figure 4-28 presents laboratory test results using the cryogenic system in Fig. 4-27(a) that demonstrate better than the required ±1 mK hohlraum temperature control with the cryocooler cycling on and off. The stability was demonstrated over a 48 h period with a 4 min off/6 min on duty cycle.

A room temperature positioner is operational and has demonstrated the viability of the design architecture. The cryogenic system has been prototyped and has demonstrated the necessary precision of cryogenic target temperature control. The first Ignition Target Inserter Cryostat (ITIC) has been assembled and will be fielded on the existing NIF positioner to demonstrate integrated performance of the system. Assembly of the first complete CTS system will begin late in 2008 with installation in NIF by 2010.

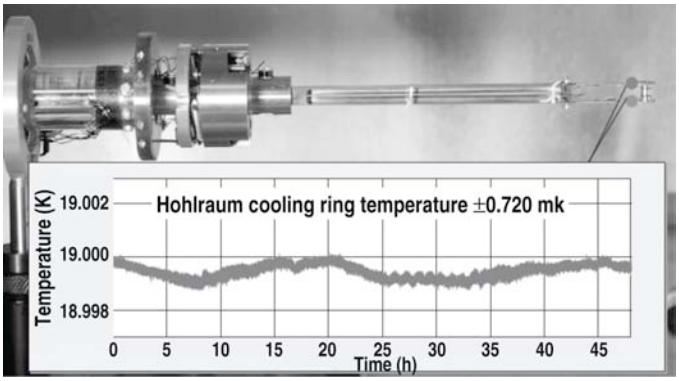

Fig. 4-28. The required ±1 mK temperature stability has been demonstrated with cryocooler cycling 4 min off / 6 min on for a test duration of 48 h.

4.2. DIRECT DRIVE TARGET DEVELOPMENT

4.2.1. Fill Tube Development for Foam Shells for OMEGA, NIF and Fast Ignition Application

A process for successfully attaching fill tubes has been developed for indirect drive NIF Shells as described in Section 4.1.1.4. We have extended this technology to attach a 10 μm fill tube to a variety of relevant shells for direct drive experiments. These include NIF scale CD and low-density R/F foam shells used in cryogenic layering experiments at LLE, as well as high density R/F foam (HDRF) OMEGA size shells used in room temperature gas filled surrogate shots (Figs. 4-29 and 4-30).

Fig. 4-29. The length of the stainless steel tube serves as a reservoir increasing the effective volume of gas in the shell for this room temperature OMEGA cryo surrogate.

Fig. 4-30. The fill tube comes in from the top with a side support stalk attached for the NIF scale CD and RF foam shells.

An assembly station is utilized for all three types of fill tube attachments to shells. For each target, the stage on the assembly station is slightly modified to accommodate certain needs for the specific attachments. Everything else stays in the same position. Two tilted microscopes interfaced with CCD cameras are positioned 90° from each other, while two manipulators are also positioned 90° from each other. Figure 4-31 shows the specifications for the HDRF assembly and a radiograph of a completed target with fill tube attached.

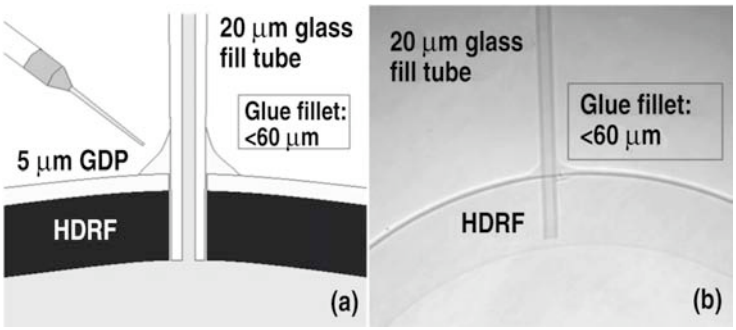

Fig. 4-31. Specifications for the HDRF assembly (a) and imaging by XRADIA (b).

Once the targets are assembled on the assembly station, the fill tube attachments are tested for conductance and leaks. X-ray fluorescence (XRF) is used to confirm that gas can flow into the shell and that the fill tube is not blocked somewhere along the attachment. After testing for conductance with XRF, HDRF foam targets are placed on the D_2 fill station to check for leaks in the glue joints at room temperature. For NIF scale RF/CD cryo-targets and fast ignition targets, each are tested on a mass spectrometer (MS) to check for leaks at cryo-temperatures after the XRF test.

The gas retention test of all the shells is done on an apparatus consisting of a SRS RGA 200 mass spectrometer, roughing pump, and sample chamber all connected to a T-fitting. To determine whether a shell is pinhole free, the gas-filled shell is transferred to the sample chamber on the MS after filling with D_2. If the shell holds the fill gas, the pressure of gas permeating through the GDP produces a signal on the MS. To determine if the shells are truly pinhole free at cryogenic temperatures, shells producing a signal on the MS are then tested using liquid nitrogen (LN_2). For pure permeation, the leak rate follows the Arrhenius equation and has a strong dependence on temperature. For a pinhole free barrier, the leak signal should drop several orders of magnitude at cryogenic temperatures versus room temperature.

We used this process to produce high density foam shells for OMEGA shots in FY08 as well as beginning to supply the cryo test station at LLE for layering of direct drive shells. The yield of this process for the room temperature targets is currently ~90% in the fill tube attachment stage (although the foam fabrication steps early in the process are much lower.

4.2.2. Development and Fabrication of NIF-Scale Resorcinol Formaldehyde Foam Shells for Cryogenic Ice Layering Experiments

Fabrication techniques for resorcinol formaldehyde foam shells were adapted for use making diameters from 2 – 5 mm. A foam capsule of this size is part of a design for future direct drive targets

at the National Ignition Facility (NIF), which calls for a 3.5 mm diameter resorcinol formaldehyde (R/F) foam shell with a 100–200 μm wall. For the near term, these NIF R/F foam targets are needed at LLE for cryogenic layering experiments. Ultimately, the foam capsules will be used in direct drive experiments on NIF. One of the critical specifications for these targets is wall uniformity. The specifications for the mode 1 wall uniformity for these R/F foam targets are usually quoted in terms of non-concentricity (NC), defined by Eq. (1).

$$\mathrm{NC} = \frac{\Delta\ \textbf{Wall Thickness}}{\textbf{2(Avg. Wall Thickness)}} \tag{1}$$

The current NC requirement for these targets is similar to the OMEGA R/F foam shells, which is $\leq 5\%$ [4-38]. The wall uniformity of these foam shells is important because wall non-uniformity adversely affects the implosions.

The density, viscosity and the interfacial tension of the emulsion components and the gelation of the R/F precursor solution all affect the R/F foam fabrication process [4-38]. For these experiments the R/F precursor solution was not altered from the OMEGA R/F shell fabrication process because the foam density required for both experiments are similar. Therefore, the gelation time, precursor viscosity and density remained unchanged [4-38]. The viscosity of the oils and interfacial tension between the emulsion components in these experiments were also similar to the OMEGA fabrication process [4-38]. In contrast, it was found that the density and the density matching of the emulsion components had to be altered in order to fabricate a high yield of the NIF-scale shells (90%). The density of the emulsion components was measured with an Anton Parr, DMA 4500 densitometer. The densitometer measures the density of the emulsion components as a function of temperature and is accurate to 0.05 mg/cc over a temperature range of 0°C to 90°C. The viscosity of the oil solutions was measured with a rheometer (Bohlin Instruments, CVO050). The interfacial tension of the emulsion system was measured by an interfacial tensiometer (Future Digital Scientific OCA-15) via the pendant drop method [4-39]. This allows measurement of interfacial tension to ±0.10 dyne/cm.

Some of the initial changes that were made to the OMEGA R/F shell fabrication process to fabricate NIF-scale R/F shells were the size of the W1 and O1 needle, and the collection tube. The OMEGA size needles and collection tube were not suitable to produce a NIF-scale double emulsion. (The largest size shells that we were able to fabricate with the OMEGA setup were 2200 μm diameter R/F shells.) In order to fabricate a NIF-scale double emulsion, it required that the diameters of the W1 and O1 needles needed to be 2x bigger than what was used in the OMEGA process. The collection tube used in the OMEGA process was also replaced with a collection tube that was 3x larger in diameter than the OMEGA-scale collection tube. Modifications to the droplet generator (DG) were also done in order to accommodate the larger needles and collection tube. Similar modifications were previously made when fabricating larger size (3–5 mm) full density Poly alpha Methyl Styrene shells (PAMS) [4-40]. Another parameter that was adopted by the NIF size PAMS fabrication process was reducing the speed of the rotary flask to agitate the shells when cured in the 70°C water bath. This was done to help stop these larger shells from breaking up during the curing process.

Another necessary modification was made in the relative densities in the double emulsion used to make the R/F shells. For the OMEGA settings, the density mismatch between the W1 and O2 components was 0.01 g/cc at 25°C, the density mismatch between the W1 and O1 needed to be

±0.005 g/cc at its curing temperature of 70°C. In order to see if the density mismatch made a difference in the yield of intact shells we fabricated NIF size shells with different O2 densities. This resulted in a mismatch of 0.02, 0.015, 0.01, 0.005, and 0.001 g/cc with the W1 solution at 25°C. The density of the O1 solution and its density mismatch with the W1 was unchanged and was in the same range as the OMEGA shell process. The results of these experiments showed that a density mismatch between the O2 and W1 solution of less than or equal to 0.005 g/cc resulted in a high yield of 90% intact NIF size R/F shells (Fig. 4-32). When the density mismatch was greater than 0.005 g/cc, the yield of intact R/F shells decreased to 20% or lower.

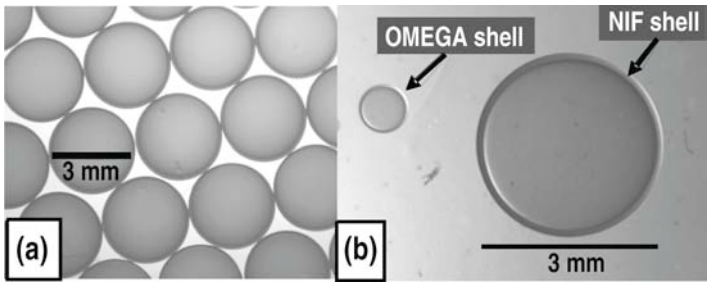

Fig. 4-32. (a) Shows a batch of NIF-scale R/F foam shells. (b) Shows the size difference between an OMEGA- and NIF-scale R/F foam shell.

Shells fabricated with this process were measured for wall uniformity using a white light interferometer and the results show that less than 5% of the shells fabricated meet the NC wall uniformity specification of < 5%. In order to improve this yield, a small amount of polymer additive (0.60 wt% styrene-butadiene-styrene (SBS) was added to the O2 solution which increased the interfacial tension of the emulsion components and the viscosity of the O2 solution [4-38]. This method was used to improve the wall uniformity of the OMEGA sized R/F shells, and a similar method was also found to help the sphericity and wall uniformity of the full density PAMS shells [4-38, 4-41, 4-42]. This modification was found empirically, but provides a hint for future theoretical work and provides a practical guide for increasing yield of shells with low NC. The addition of the SBS to the O2 solution increased the interfacial tension of the emulsion components by 4X as it increased to 4 dynes/cm, without the SBS additive the interfacial tension was 1 dyne/cm. The SBS addition to the O2 solution increased its viscosity from 10 to 18 cps at room temperature and at its curing temperature of 70° C the viscosity increased from 7 to 12 cps. This modification to the O2 helped improve the wall uniformity of the NIF-scale shell and improved the yield of shells that satisfied the 5% NC specification from less than 5% to 15%. The results of this can be seen in Fig. 4-33. Future work on improving the wall uniformity of these NIF R/F foam shells will include: optimizing the O1/W1 density mismatch for NIF size shells, as well as testing new types of oils, and polymer additives in order to increase the interfacial tension of the compound droplet.

By making the necessary modifications to the OMEGA R/F shell fabrication process we were able to successfully develop a process to fabricate a high yield of NIF–scale direct drive R/F foam shells. By optimizing foam shell fabrication parameters such as the rotation speed of the beakers, the density mismatch of the emulsion components, and increasing the size of DG dispensing needles and

the collection tube we were able to produce a 90% yield of intact foam shells. This method can be also used to successfully fabricate shells ranging from the 2 to 5 mm range.

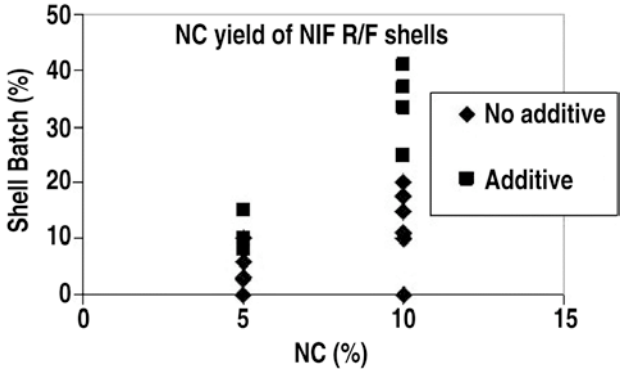

Fig. 4-33. Nonconcentricity wall uniformity plot showing the yield of shells in a batch that have <5% NC and <10% NC. Shells made with the additive in the O2 solution have a higher yield of shells with good NC (15% with NC <5%) than shells that were fabricated using no additive (<5% with NC <5%) in the O2 solution.

REFERENCES FOR SECTION 4

[4-1] S.W. Haan, P.A. Amendt, T.R. Dittrich, S.P. Hatchett, M.C. Herrmann, O.A. Hurrixane, M.M. Marinak, D. Munro, S.M. Pollaine, G.A. Strobel, L.J. Suter, "Update on NIF Indirect Drive Ignition Target Fabrication Specifications," Fusion Technol. **45**, 69 (2004).

[4-2] H. Huang, R.B. Stephens, S.A. Eddinger, A. Nikroo, K.C. Chen, H.W. Xu, J. Gunther, "Non-destructive Quantitative Dopant Profiling Technique by Contact Radiography," Fusion Sci. Technol. **49**(4), 650 (2006).

[4-3] H. Huang, R.B. Stephens, A. Nikroo, S.A. Eddinger, K.C. Chen, H.W. Xu, K.A. Moreno, K.P. Youngblood and M. Skelton, "Quantitative Radiography: Film Model Calibration and Dopant/Impurity Measurement in ICF Ablators," Fusion Sci. Technol. **51**, 530 (2007).

[4-4] Amptek XR100CR specifications: http://www.amptek.com/xr100cr.html.

[4-5] On-line x-ray absorption database compiled by Henke et al., maintained by LBNL: http://henke.lbl.gov/optical_constants/atten2.html.

[4-6] www.goodfellow.com.

[4-7] H. Huang, A. Nikroo, R.B. Stephens, S.A. Eddinger, D.R. Wall, K.A. Moreno, H.W. Xu, "Element Specific Dopant/Impurity Profiling for ICF Ablator Capsules," Fusion Sci. Technol., to be published.

[4-8] S.W. Haan, et al., "Update on Specifications for NIF Ignition Targets: Rev3," Fusion Sci. Technol., to be published.

[4-9] R.C. Montesanti, M.A. Johnson, E.R. Mapoles, D.P. Atkinson, J.D. Hughes, J.L. Reynolds, "Phase Shifting Diffraction Interferometer for Inspecting NIF Ignition-Target Shells," Proc. American Society for Precision Engineering 2006 Annual Meeting (2006).

[4-10] R.C. Montesanti, E.R. Mapoles, M.A. Johnson, J.D. Hughes, W.C. Behrendt, D.W. Bennett, J.L. Reynolds, M.A. Carillo, "Semi-Automatic System with Transfer Chucks for Handling the NIF Ignition Target Shells," Fusion Sci. Technol., to be published.

[4-11] M.A. Johnson, "LiteProp," Igor Analysis Software for PSDI based on algorithms developed by Donald W. Phillion.

[4-12] Donald W. Phillion, "Lick," PSDI Data Acquisition Software.

[4-13] Linear and rotary stages for PSDI. http://www.aerotech.com/.

[4-14] M.A. Johnson and J.S. Taylor. "PSDI Target Fabrication Overview," Proc. American Society of Precision Engineering 2006 Annual Meeting, pp. 15-18 (2006).

[4-15] Nyquist-Shannon Sampling Theorem, http://en.wikipedia.org/wiki/Nyquist%E2%80 %93 Shannon_sampling_theorem#References (2008).

[4-16] A. Nyugen, "Characterization of Isolated Defects for NIF Targets using PSDI with an Analysis of Shell Flipping Capability," Proc. 18th Target Fabrication Meeting, Lake Tahoe, California, 2008, to be published in Fusion Sci. Technol.

[4-17] R.C. Montesanti, "Rotation of a Shell when Transferring It Between Two Non-Collinear Vacuum Chuck Tips," 17 March 2006, (unpublished).

[4-18] Y.T. Lee, et al., "Increasing the Throughput of the Phase Shifting Diffraction Interferometer (PSDI)," Fusion Sci. Technol., to be published.

[4-19] D.H. Froula, L. Divol, N.B. Meezan, S. Dixit, J.D. Moody, P. Neumayer, B.B. Pollock, J.S. Ross, and S.H. Glenzer, "Ideal Laser-Beam Propagation through High-Temperature Ignition Hohlraum Plasmas," Phys. Rev. Lett. **98**, 085001 (2007).

[4-20] P. Neumayer, et al., "Energetics of Multiple-Ion Species Hohlraum Plasmas," Phys. Plasmas **15**, 056307 (2008).

[4-21] H.L. Wilken, J. Gunther, M.P. Mauldin, A. Nikroo, J.R. Wall, D.R. Wall, and R.J. Wallace, "Process in Coating Multi-layered Cocktail Hohlraums," Fusion Sci. Technol. **49** 846 (2006).

[4-22] H.L. Wilkens, A. Nikroo, D.R. Wall, and J.R. Wall, "Developing Depleted Uranium and Gold Cocktail Hohlraums for the National Ignition Facility," Phys. Plasmas **14**, 056310 (2007).

[4-23] J. Lillard and R.J. Hanrahan, "Corrosion of Uranium and Uranium Alloys," ASM Handbook Vol. **13B**: Corrosion: Materials, S D Cramer and B S Covino Jr, Volume Editors (ASM International, Materials Park, OH, 2005) pp 370–384.

[4-24] M.D. Rosen, "The Physics Issues that Determine Inertial Confinement Fusion Target Gain and Driver Requirements: A tutorial," Phys. Plasmas **6**, 1690 (1999).

[4-25] O.S. Jones, et al., "Proof Of Principle Experiments That Demonstrate Utility of Cocktail Hohlraums for Indirect Drive Ignition," Phys. Plasmas **14**, 0536311 (2007).

[4-26] J.M. Soures, et al., "Direct-Drive Laser-Fusion Experiments with the OMEGA, 60-beam, >40 kJ, Ultraviolet Laser System," Phys. Plasmas **3**, 2108 (1996).

[4-27] H. Nishumura, T. Endo, H. Shiraga, U. Kato, and S. Nakai, "X-Ray Emission from High-2 Mixture Plasmas Generated with Intense Blue Laser Light," Appl. Phys. Lett. **62**, 1344 (1993).

[4-28] T.J. Orzechowski, M.D. Rosen, H.N. Kornblum, L.J. Suter, A.R. Thiessen, R.J. Wallace, and L.J. Porter, "The Rosseland Mean Opacity of a Mixture of Gold and Gadolinium at High Temperatures," Phys. Rev. Lett. **77**, 3545 (1996).

[4-29] D. Colobant, M. Klapisch, and A. Bar-Shalom, "Increase in Rosseland Mean Opacity for Inertial Fusion Hohlraum Walls," Phys. Rev. E **57**, 3411 (1998).

[4-30] L. Suter, J. Rothenberg, D. Munro, B. Van Wonterghem, and S. Haan, "Exploring the Limits of the National Ignition Facility's Capsule Coupling," Phys. Plasmas **7**, 2092 (2000).

[4-31] L. Abelmann and C. Lodder, "Invited Review: Oblique Evaporation and Surface Diffusion," Thin Solid Films **305**, 1 (1997).

[4-32] J. Dalla Torre, G.H. Gilme, D.L. Windt, R. Kalyanaraman, F.H. Gaumann, P.L. O'Sullivan, J. Sapjeta, T. Diaz de la Rubia, M. Djafari Rouhan, "Microstructure of Thin Tantalum Films Sputtered onto Inclined Substrates: Experiments and Atomistic Simulations," J. Appl. Phys. **94**, 263 (2003).

[4-33] C.A. Nichol, S.M. Rossnagel, and S. Hamaguchi, "Ionized Physical Vapor Deposition of Cu for High Aspect Ratio Damascene Trench Fill Applications," J. Vac. Sci. Technol. B **14**, 3270 (1996).

[4-34] L.J. Atherton, E.I. Moses, K. Carlisle, and J.D. Kilkenny, "The Ignition Target for the National Ignition Facility," Proc. EUSPEN Conf., Bremen, Germany, V**2**, 158 (2007).

[4-35] J.L. Klingmann, et al., "Design and Fabrication of a Novel Cryogenic Laser-Driven Ignition Target," Proc. EUSPEN Conf., Bremen, Germany, V**2**, 249 (2007).

[4-36] B.J. Kozioziemski, J.A. Koch, A. Barty, H.E. Martz, W.K. Lee and K. Fezzaa, "Quantitative Characterization of Inertial Confinement Fusion Capsules Using Phase Contrast Enhanced X-ray Imaging," J. Appl. Phys. **97**, 063103 (2005).

[4-37] B.J. Haid, "Helium Pot System for Maintaining Sample Temperature after Cryocooler Deactivation," Adv. Cryogenic Eng. **51A**, 147 (2005).

[4-38] R.R. Paguio, et al., "Improving the Wall Uniformity of Resorcinol Formaldehyde Foam Shells by Modifying Emulsion Components," Fusion Sci. Technol. **51**, 682 (2007).

[4-39] Song, B. et al., "Determination of Interfacial Tension from the Profile of a Pendant Drop Using Computer- Aided Image Processing," J. Colloid & Interface Science **184**, 77 (1996).

[4-40] M. Takagi, et al., "Investigation of Large Poly (α-Methylstyrene) Mandrels for High Gain Designs Using Microencapsulation," Fusion Sci. Technol. **45**, 171 (2004).

[4-41] M. Takagi, et al., "Decreasing Out-of-Round in Poly(α-Methylstyrene) Mandrels by Increasing Interfacial Tension," Fusion Technol. **38**(1), 46 (2001).

[4-42] R.R. Paguio, et al., "Improving the Yield of Target Quality OMEGA Sized PAMS Mandrels by Modifying Emulsion Components," Fusion Technol. **49**(4), 743 (2006).

5. OMEGA TARGET DEVELOPMENT

5.1. INDIRECT DRIVE TARGET DEVELOPMENT

5.1.1. High Z Doping of Glass Shells

A new process for making High Z doped glass shells is based on the Si-GDP to glass conversion method (Hoppe process) and allows for the manufacturing of large, thick and exceedingly uniform shells [5-1]. Germanium (Ge) doped glass shells are made essentially by the same process as pure silica glass shells except a Ge dopant is added during the glow discharge polymer (GDP) coating step (Fig. 5-1).

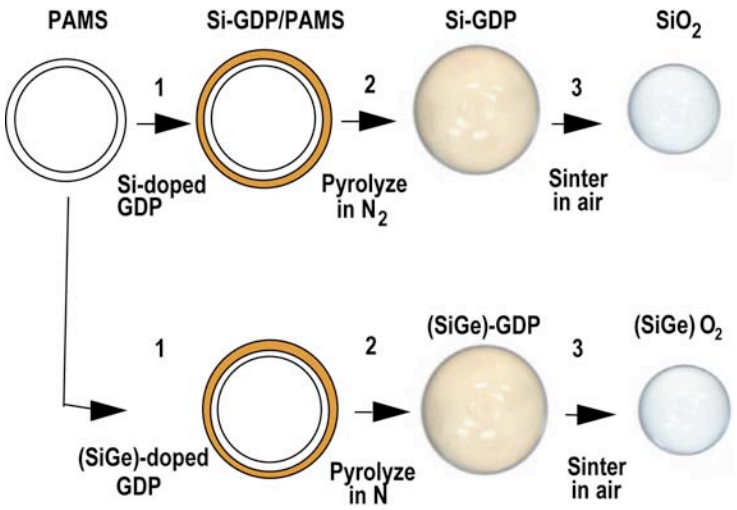

Fig. 5-1. Ge doped glass is made using the SiGDP to glass process.

PAMS mandrels were made by the droplet generator technique. These shells were roll coated in a plasma polymerization system based on a helical resonator and piezo bouncer described by previous authors [5-2]. Tetramethyl silane (TMS), tetramethyl germane (TMG), trans-2-butene (T2B) and hydrogen were used as feed-stock gases for the plasma coater. After the SiGe-GDP coating step was completed, the PAMS mandrel was removed by a controlled heating process in which the temperature was slowly ramped to 300°C under nitrogen to decompose and volatilize the PAMS polymer. The resulting SiGe-GDP mandrels were then successfully converted into a Ge doped glass shell by slow pyrolysis in air.

Measurement of the surface finish by an atomic force microscopy spheremapping technique and wall uniformity by optical interference [5-3] show the Ge doped shells are extremely round and uniform in thickness (Fig. 5-2). The ~1130 x 12 μm Ge doped glass shell depicted in this figure essentially meets the National Ignition Facility (NIF) requirements (smooth bold line) for surface smoothness and has a Δ wall ($wall_{max} - wall_{min}$) of only .04 μm.

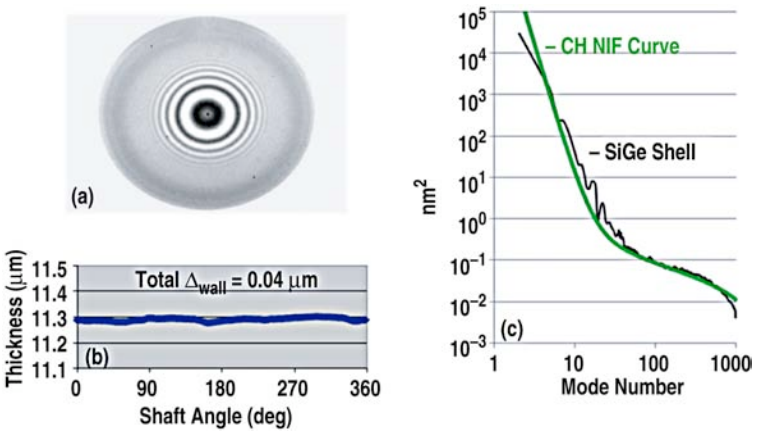

Fig. 5-2. Bull's-eye fringe pattern and spheremapper/wallmapper plots show the high quality of a 1130 x 12 μm glass shell made from SiGe-GDP.

X-ray Fluorescence (XRF) measurement of a doped glass shell confirms the presence of Ge and the absence of any other high Z contaminants. Ge concentration of 0.43 g/cc was measured. This corresponds to about a 5:1 Si:Ge ratio, or ~6 at.% Ge doped glass as shown in Fig. 5-3.

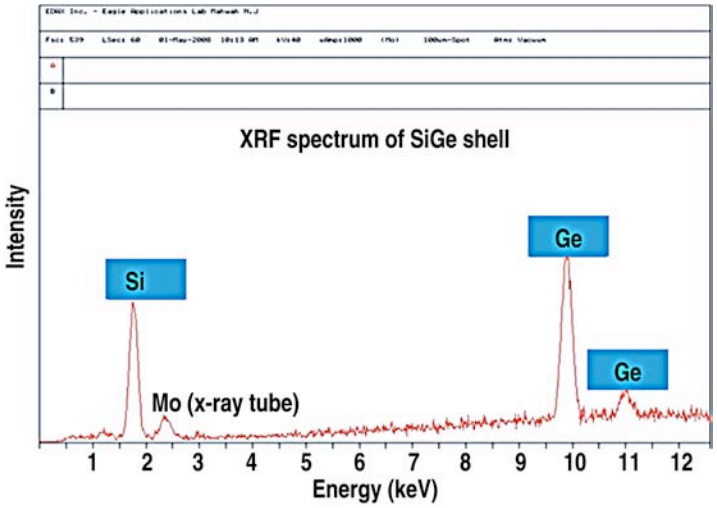

Fig. 5-3. First successfully doped glass shells as determined by XRF is ~6 at.% germanium.

The air conversion conditions still need to be fully optimized. Pyrolysis of a Ge and Si doped GDP mandrel in air at increasingly higher maximum temperatures yield differing results (Fig. 5-4). At around 450°C the SiGe-GDP appears to be essentially completely converted to glass. Up to ~750°C the only observed change was an apparent densification as the diameter and wall thickness continued to shrink slightly. However, when heated to around 900°C, the appearance of the shells indicates possible phase separation is occurring in the glass. Figure 5-5 shows the SEM/EDXS image of a shard of a glass shell pyrolyzed to ~900°C along with the image of a shard pyrolyzed to only 750°C. The surface of the higher temperature pyrolyzed shell has significantly more texture than the lower temperature shell. The Ge content also appears to be somewhat higher in these roughened patches. Additional work is planned to further investigate exactly what is occurring here and to determine the temperature that will lead to maximum density and shell strength with lowest permeability to helium and hydrogen.

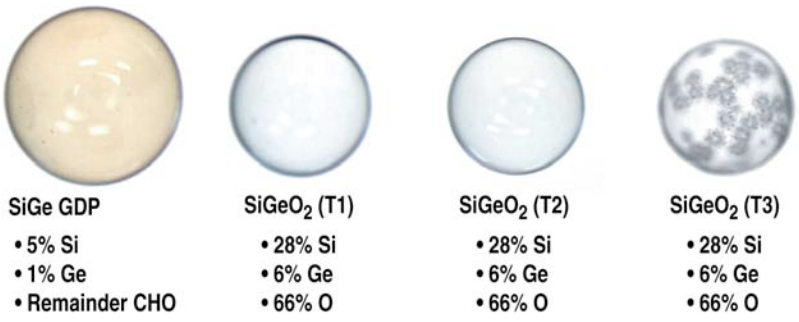

Fig. 5-4. Pyrolysis to different temperatures results in significantly different results. Optimum pyrolysis temperature needs to be found that results in maximum density (i.e., highest shell strength and lowest permeability).

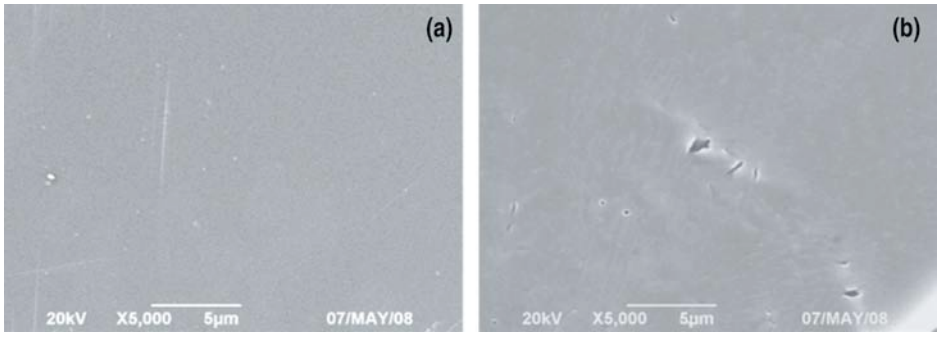

Fig. 5-5. SEM/EDXS analysis of SiGe shells reveals changes in surface texture at high temperatures. At higher temperature, formation of nodules indicates possible phase separation is occurring.

The results of measurements to determine some of the properties of Ge doped glass shells pyrolyzed to 750°C are summarized in Table 5-1.

Table 5-1
Properties of 6% Ge Doped Glass

	SiGe Glass	Si Glass
Index of refraction	1.48 ± 0.02	1.47 ± 0.02
Density (g/cc)	2.44 ± 0.1	2.20 ± 0.1
He time constant **t** (min)	22	67
Young's modulus	3.4×10^6	6.0×10^6

The index of refraction of these capsules was determined interferometrically by measuring the change in path length of white light traveling through the glass shell wall relative to air. Density was determined by a combination of optical measurement of shell diameter and wall thickness coupled with weighing of the shell on a precision microbalance. The buckle strength (P_b) of an ideal defect-free spherical shell of wall thickness w and diameter d, can be utilized to determine Young's Modulus from the equation [5-4],

$$E = [3\,(v^2 - 1)]^{0.5}/8P_b(d/w)^2 \quad .$$

Where E and v are the Young's Modulus and Poisson's ratio for the material respectively; v was assumed to be 0.24, typical for glass.

The densification of the glass has not been fully optimized so it is conceivable that the density, He time constant, and Young's modulus could increase with further optimization. As currently pyrolyzed, the shells are close to full density based on comparison of the measured density (2.44 g/cc) to the expected density of 6% Ge doped glass of 2.48 g/cc (ignoring lattice expansion caused by replacing an atom of Si with Ge).

5.2. DIRECT DRIVE TARGET DEVELOPMENT

5.2.1. Properties of Silicon-Doped GDP Shells used for Cryogenic Implosions at OMEGA

One suggested approach to decreasing preheat of LLE Cryo-targets is to add a silicon dopant of ~4–6 at. % to the normal plasma polymer. As in the case of pure CH and CD shells used previously, the physical properties of these shells, are of utmost importance to allow proper fielding for cryogenic shots. We fabricated and characterized two types of Si-doped GDP capsules: single layer Si-doped glow discharge polymer shells (SiGDP) and double layer Si-doped GDP/SCD shells (SiGDP/SCD).

SiGDP shells were made by the depolymerizable mandrel technique using poly-alpha-methyl styrene (PAMS) mandrels [5-5, 5-6] as described in previous Section 5.1.1. In particular, the slow PAMS removal profile, developed for fabrication of glass shells from silicon doped GDP shells, was adopted for the SiGDP cryogenic shells [5-7, 5-8].

The roughness, uniformity and strength of Si-GDP shells were measured and compared to those of CD cryo shells. Although the addition of Si does affect some of these properties slightly, the shells still meet the requirements. These differences are discussed here. The effect on IR transparency is much more profound. IR heating is used to layer and smooth the ice in cryogenic shells including SiGDP shells. If the shell wall material absorbs at the IR heating wavelength, it will interfere with the smoothing process. Oxygen pick up in polymer shells results in an OH stretch in the IR spectra at the 3200–3700 cm^{-1} region that interferes with IR heating at 3160 cm^{-1} [5-9]. SiGDP shells have been found to be more reactive to air than regular "strong" carbon deuterium (SCD) shells. An investigation of absorption in the OH region (3160 cm^{-1}) was carried out using Nicolet Fourier Transform Infrared Spectroscopy Continuum microscope (FTIR microscope) analysis. The OH absorption coefficient of SiGDP at 3160 cm^{-1} has been determined for comparison to absorption coefficient of D_2 ice at 3160 cm^{-1}.

A "witness" technique was developed to determine the OH absorption of SiGDP shells. In this technique, SiGDP witness shells and SCD witness shells were cut into pieces under a microscope. FTIR scans were taken of the pieces over time in air. The data were used to gain insight into the capsule's OH pick up rate at 3160 cm^{-1}, which is the wavelength used for IR heating. The OH absorption of the SiGDP shells wall interferes with IR heating for smooth ice layering at this specific wavelength. Results of OH pick up over time for SiGDP and SCD are presented in Fig. 5-6. SiGDP IR absorption at 3160 cm^{-1} shows a rapid OH pick up rate compared to SCD shells. In Fig. 5-7, a close up view of the region between 3200–3700 cm^{-1} shows the OH growth as a function of time for 5 μm Si doped GDP polymer coating. The baselines of each scan were normalized at 3800 cm^{-1}.

The FTIR spectra were quantitatively analyzed to determine the absorption coefficient at 3160 cm^{-1}. The plot of IR absorption coefficients over time for 5 and 26 μm SiGDP, are shown in Fig. 5-8. The absorption coefficient was calculated by measuring the absorbance difference on 3800 cm^{-1} and 3160 cm^{-1}, dividing by shell wall thickness and converting to natural log scale.

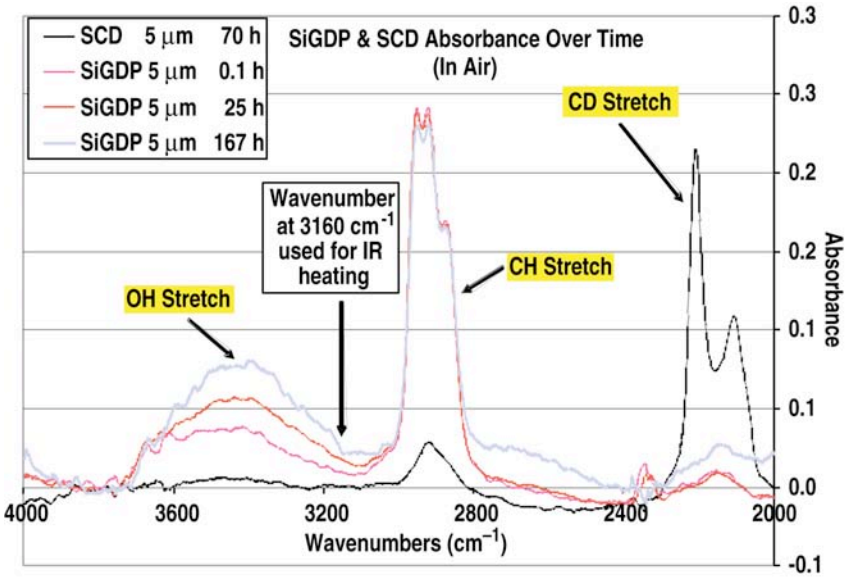

Fig. 5-6. SiGDP and SCD IR absorption at 4000–2000 cm^{-1} over time in air. SiGDP absorption shows a rapid OH pick up rate compared to SCD.

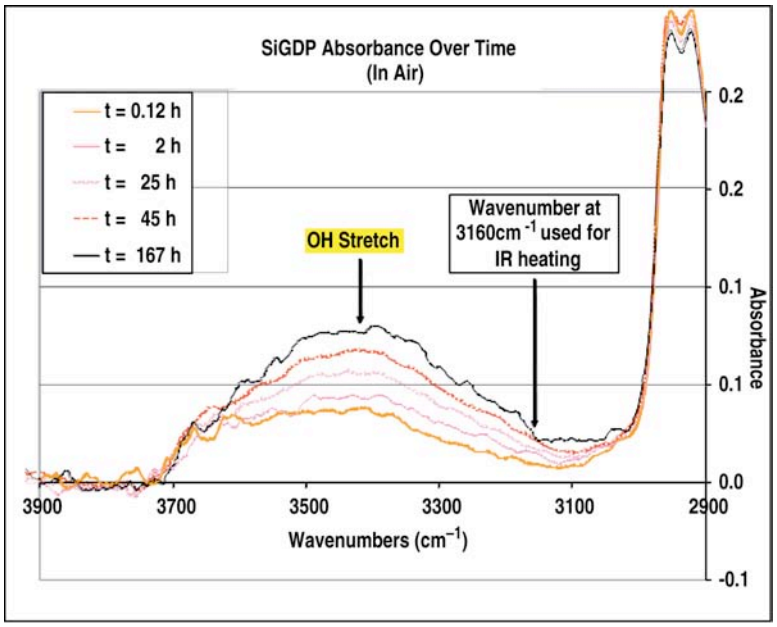

Fig. 5-7. SiGDP IR absorption at 3200–3700 cm^{-1} shows a rapid OH pick up over time. The broad OH stretch interferes with IR heating for smooth ice layering.

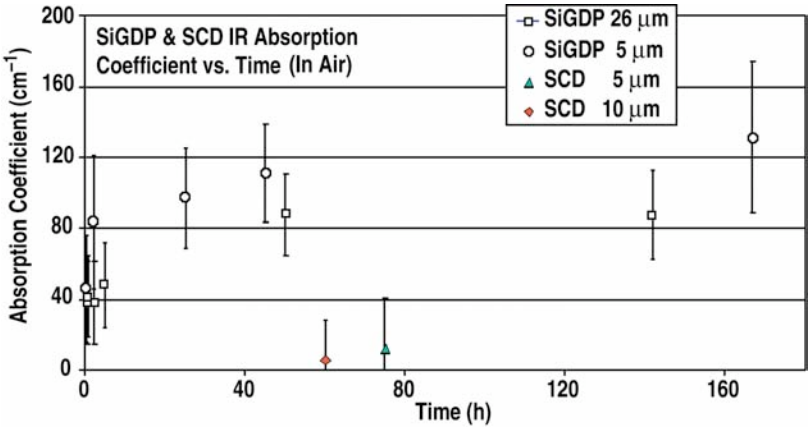

Fig. 5-8. Plot of 5 μm, 26 μm SiGDP and 5 μm, 10 μm SCD IR OH absorption coefficients over time. The absorption coefficient calculated from the 26 μm SiGDP test agrees with the absorption coefficient calculated from the 5 μm SiGDP test. The absorption coefficient was calculated by measuring the absorbance difference on 3800 and 3160 cm^{-1}, dividing by shell wall thickness and converting to natural log scale.

In order to limit air exposure, special handling was required. "Witness" shells, shells removed from the batch for analysis and not delivered for experiment, were used to determine the batch characteristic. After the controlled heating process, two shells were set aside for IR analysis, and the rest were immediately transferred to a nitrogen storage box upon removal from the pyrolysis oven. Shells were later removed from the nitrogen storage for dimensional analysis by interferometry, then returned to the nitrogen box immediately upon completion of measurement (~1 h). Air exposure time was monitored and recorded. "Witness" shells were removed for buckle test [5-10], wallmapper [5-11], AFM spheremapper [5-12], XRF spectrometry [5-13] and DD permeation test [5-14]. The use of "witness" shells allows SiGDP shells to be delivered with only 2 h air exposure.

The quality of the ice layer is dependent on shell wall uniformity [5-15]. The SiGDP shell wall must not vary more than 0.25 μm from maximum to minimum thickness. Shell wall thickness uniformity is driven by proper agitation during the coating process and the proper selection of mandrels with uniform walls as in the case of undoped shells. Orthogonal wall thickness traces of representative shells show that SiGDP shells can be produced with wall non-uniformity of less than 0.05 μm.

To determine the buckle strength, the shells are exposed to increasingly higher pressures and the buckle pressure is recorded when the shells are broken. Compared with the SCD shells of the same dimensions, which buckled at ~50 psi, SiGDP shells have higher average buckle strength of ~70 psi. Since SiGDP shells have higher buckle strength, it allows filling them in higher pressure steps for cryogenic experiments.

To determine the time constant, permeation rates were measured on 900x5 μm SiGDP shells. Two SiGDP shells from the same batch were filled with deuterium in a pressure vessel at 30 psi at room temperature and allowed to permeate for at least one hour. The pressure vessel was vented and each shell was measured in the mass spectrometer. For 900x5 μm SiGDP shells, a 12 s D_2 half-life was measured. The experiment was repeated on 900x26 μm SiGDP shells that confirmed the calculated time constant. The permeation time constant of the 900x26 μm shells measured as 70 s,

about five times that of the 900x5 μm shells. SiGDP shells have higher D_2 permeability than SCD shells; 2.4×10^{-14} (mol × m/m^2 × Pa × s) as compared to 9.0×10^{-15} (mol × m/m^2 × Pa × s). The higher permeability of SiGDP shells allows for faster D_2 fill rate compared to SCD shells.

Si concentration was measured on three shells from each batch using XRF spectrometry. With the flow rate of tetramethyl silane, trans-2-butene and hydrogen regulated by a mass flow controller, 4–6 at. % silicon concentration was attained. For 7 batches of SiGDP shells measured, the average Si at. % is 5.7 ± 0.4. The range of silicon atom percent achieved meets the OMEGA cryogenic target design.

5.2.2. Improved Gas Retention of GDP Coated R/F Foam Shells for Cryogenic Experiments on OMEGA

For cryogenic experiments using foam capsules, the shells must be able to hold a fill gas such as DT or D_2. This issue has led to the investigation of ways to improve the yield by modifying the coating conditions of the GDP over-coating process. Specifically, by changing the background coating pressure from the constant 75 mTorr throughout the run to a two-step coating process of a high pressure coating at 250 mTorr followed by low pressure coating of 75 mTorr. This modification has increased the yield of gas retentive styrene butadiene styrene (SBS) modified R/F shells from ~15% to 60%. The surface roughness of these shells is also improved from ~45 nm RMS to ~20 nm RMS with this modification to the coating conditions.

Once the R/F shells are over-coated, the GDP coating thickness is measured by white light interferometry. The uniformity of the over-coating is measured using a wall mapping process [5-16], and the surface roughness of the over-coating is analyzed by a Wyko interferometer. Once the shells are over-coated and characterized, they are tested for gas retention. The capsules are permeation filled with D_2 on a fill station and the permeation rate measured using a SRS RGA200 mass spectrometer (MS) [5-17] at room temperature and cryogenic temperatures.

Increasing the background coating pressure during the GDP deposition was investigated with the intent to improve the gas retention of SBS R/F shells. The background coating pressure affects the random walk of the hydrocarbon fragments; this can influence the way the fragment is deposited on the shell through diffusion limited aggregation (DLA). When coating a foam shell, the constituent strands act as the substrate for arriving atoms. If the deposition is more ballistic in character, the coating is less likely to bridge the strands and cover the intervening holes. The previous standard 75 mTorr (coating pressure) deposition creates a rough coating with many surface domes as shown in Fig. 5-9(a). Therefore, by increasing the pressure so that the deposition has a more DLA nature than ballistic, it could lead to a coating that is more likely to bridge the strands and cover the pores of the foam. Changing the random walk of these particles by increasing the background pressure can also lead to a slower coating rate because the mean free path of the fragments is decreased. For example, by increasing the background coating pressure to 250 mTorr, the measured coating rate is one tenth the typical coating rate for GDP using the standard process at 75 mTorr. This slower coating rate can also slow roughness growth of the coating [5-18].

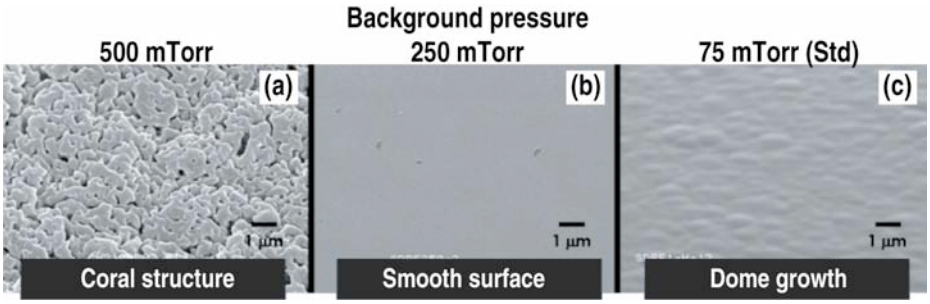

Fig. 5-9. SEM images of the surface of GDP coated R/F shells at various background pressures. Changing the background pressure of the CVD coater from 75 to 250 mTorr results in an improvement in surface roughness.

The first experiment was to overcoat the shells with 1–2 μm of GDP at various background coating pressures. The coating pressures that were used were 500 mTorr, 250 mTorr and the previously standard background coating pressure of 75 mTorr. The scanning electron microscopy (SEM) images of these over-coatings are shown in Fig. 5-10, which illustrates that the coatings done at 250 mTorr [Fig. 5-10(b)] are qualitatively smoother than the standard coating process at 75 mTorr [Fig. 5-10(a)]. But, DLA deposition at its extreme approaches fractal growth and cannot lead to a better surface finish by itself. In fact, the surface finish will degrade if the deposition is purely DLA and is the bulk of the coating. We observe this surface degradation when the coating were increased to 500 mTorr as shown in Fig. 5-10(c), and appears to be the roughest over-coating out of the three. This is empirically observed, of course, in terms of the observation that there appears to be an optimal initial pressure of 250 mTorr (about 3 times the normal pressure) to obtain the best surface finish.

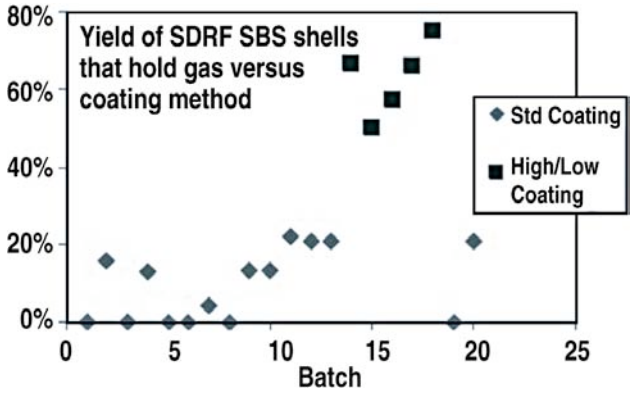

Fig. 5-10. Gas retention yield of OMEGA-scale GDP coated SBS R/F shells using the standard and High/Low GDP over-coating methods. The data shows that using the High/Low GDP method improves the yield of gas retentive shells from 15% to 60%.

In order to take advantage of the smoother coating observed, the next step was to overcoat a shell at 250 mTorr to the standard GDP thickness of 4–5 μm for SBS R/F shells. The overcoat at 250 mTorr was not possible because at this pressure the shells began to agglomerate after 24 h of coating. This caused rips and tears in the over-coating, and resulted in non-gas-retentive shells. At a

coating of 20 h the coating thickness of the GDP is only 0.8–1.0 μm. At this thickness the coating is not strong enough to hold the required fill gas.

The results observed by increasing the coating pressure to 250 mTorr led to the development of a dual pressure coating process. This coating process begins with a high pressure coating at 250 mTorr that was used to promote the smooth surface and create a more omni-directional coating which bridges the foam gaps in R/F. The high pressure coating was done for roughly 19–22 h, which was right before the shells were about to agglomerate. At this time, the background coating pressure was lowered to 75 mTorr for the remainder of the coating up to the required thickness of 4–5 μm (for the shells to hold gas). The Wyko interferometry data shows that the surface roughness RMS of the GDP over-coating done with the High/Low over-coatings improved from ~45 nm RMS to ~20 nm RMS in comparison to the standard process. Wallmap analysis of these over-coatings show that the coating uniformity using the High/Low process is comparable to the standard GDP coating process, and falls within the target specification (Coating Δ wall of < 0.4 μm). The shells coated with the High/Low coatings were then tested for gas retention. The gas retention results shown in the plot in Fig. 5-10 show that the yield of gas retentive SBS R/F shells improved from ~15% to 60%. Factors affecting the gas retention of the shells in a negative way using this method are the final thickness of the GDP over-coating (if > 4 μm) and the duration of the high pressure coating (if > 18 h).

Although the focus of this work was ~900 μm OMEGA size shells, this was applied to ~2 mm NIF shells that were fabricated with the GA roto-coater glow discharge polymer system. The result from the roto-coater using the high-low coating method was similar to the gas retention yield of 70% for NIF shells at a coating thickness of 13–15 μm [5-19]. The yield of gas retentive shells using these methods is shown on the plot depicted in Fig. 5-11. Future work will include optimizing the coater conditions in efforts to see if this process could create thinner pinhole free over-coatings. These R/F foam shells may need to have a thinner pinhole free permeation barrier than the current GDP thickness (12–15 μm) for future experiments.

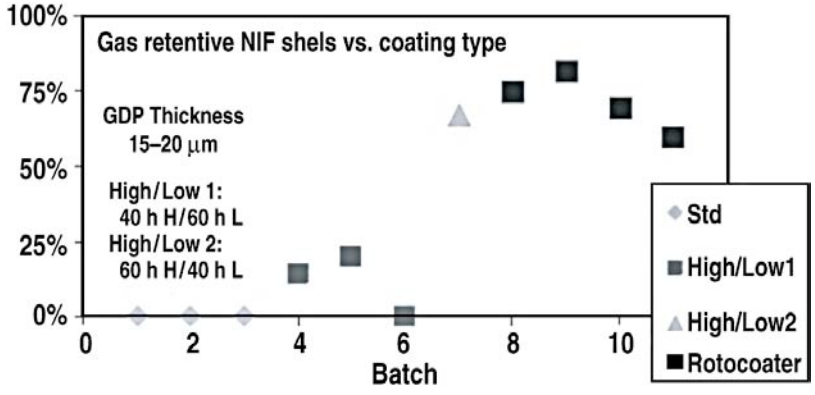

Fig. 5-11. The gas retention data of NIF SBS R/F shells that were over-coated with GDP using a variety of coating methods. Shells that are coated with the roto-coater and the High/Low methods are the only NIF-scale R/F shells that hold gas. Future work will include experiments to confirm this observation, as well as combining the two methods (Roto-coater and High/Low).

In summary, by changing the background coating pressure parameters during GDP deposition, we were able to develop a process that produces a smoother GDP over-coating with a higher yield of gas retentive, OMEGA-scale, SBS R/F foam shells. This work has been extended to improve the yield of gas-retentive shells of larger size R/F foam shells that are required for the NIF and HAPL programs.

5.2.3. Modifying the Pore Size of Resorcinol Formaldehyde Aerogels for Fabrication of Hollow Spheres for Direct Drive ICF Experiments

Cryogenic ice layering experiments at LLE using hollow R/F shells have shown advantages of larger pore aerogels compared to the pore sizes of the standard R/F formulation. This led to the request for hollow R/F shells with larger pores (Fig. 5-12) for cryogenic ice layering experiments. This work describes our success at making an improved formulation of large pore size R/F that is more suited to the shell fabrication process.

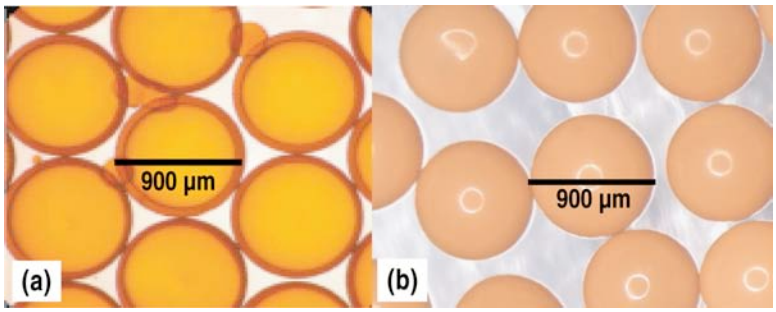

Fig. 5-12. (a) Standard R/F shells that are transparent. (b) Large pore R/F shells made with the PA Method (using PVA) that are opaque.

The R/F aerogel, first developed by Pekala, et al., begins with a precursor solution that forms into an aerogel by a polycondensation reaction using a two-step (base/acid catalysis) polycondensation reaction [5-20]. The precursor solution starts off with a base catalysis reaction using resorcinol, formaldehyde, water and a base catalysis (0.58M sodium bicarbonate) that creates the hydroxymethyl aggregates that react with one another to form the primary particles. These particles then go through an acid catalysis step (0.01M benzoic acid) that brings these particles together to form the gel by forming methylene ether bridges. Controlling solvent and precursor quantities can control the density of the aerogel. The gel is then solvent exchanged into isopropanol to remove any water in the porous gel network, then dried using a supercritical CO_2 drier to prevent shrinkage and cracking, preserving the low density structure of the resulting aerogel.

Previous work on modifying the pore size of the R/F aerogel to produce hollow shells was done by decreasing the base catalyst to resorcinol ratio, creating a large (~0.5 μm) pore R/F aerogel through reaction limited aggregation [5-21, 5-22]. We refer to this as the low-catalyst (LC) method. A drawback to the LC method is that the final density was 30% lower than the calculated target density (based on reactant mass) [5-22]. The density reduction is due to less catalyst in the base catalysis part of this two-step polycondensation reaction, which forms less hydroxymethyl adducts due to un-reacted monomer in the reaction. Another drawback was the instability of the precursor solution at room temperature.

These results lead us to investigate alternative ways to produce larger pore R/F aerogel that would be more compatible with our current shell fabrication process. This work describes an alternative way to modify the pore size of the R/F aerogel without any significant change to the aerogel target density. This was accomplished by an addition of hydrophilic polymer additive [Poly Vinyl Alcohol (PVA) or Poly Acrylic Acid (PAA)] to the R/F precursor solution which acts as an impurity in the reaction. We will refer to this as the polymer addition (PA) method. The polymer (0.10 wt% PAA or 0.30 wt% PVA) was dissolved into the water portion of the R/F precursor solution. Bulk samples of these aerogels were produced using the PA, standard (STD) and LC methods and were analyzed for pore and aerogel structure. The polymer impurity modified the cross linking and aggregation of the primary particles thus changing the formation of the aerogel structure, and changing the pore size. This modification successfully increases the pore size of the R/F aerogel with little or no change to the precursor's gelation time when compared to the standard process which made it possible to use the same shell fabrication process used for standard pore size R/F aerogel shells [5-23 – 5-25].

The resulting aerogels were characterized for aerogel structure using scanning electron microscopy (SEM), nitrogen gas absorption (Micromeritics ASAP 2020), and ultra-small angle x-ray scattering (USAXS) using the Advanced Photon Source (APS) instrument at the Argonne National Laboratory. USAXS is a nondestructive measurement technique in which the intensity of elastically scattered x-rays at small and ultra-small angles is recorded after they pass through the sample. As these x-rays scatter from inhomogeneities within a sample they deliver structural information about the sample [5-26]. The APS USAXS instrument is sensitive to more than 3 decades (1 nm to above 1 mm) of microstructural feature sizes, measured in a single 15-minutes long scan [5-26].

Prior to shell fabrication, bulk samples of the aerogel were produced to observe the precursors stability, gelation time, and optical clarity. The standard pore R/F that we use is transparent. A modification that resulted in larger pores would produce a more opaque aerogel due to the increased amount of visible light scattering caused by the larger pores near the wavelength of visible light. This was also observed in our initial large pore modification experiments [5-22] and was observed in our new modifications using the PA method.

Bulk R/F aerogel samples were analyzed using nitrogen absorption which provided the BET (Brunauer, Emmett and Teller method) [5-27] surface area of these aerogels. The results in Fig. 5-13 show that the modified R/F aerogels have a smaller surface area then the standard R/F aerogel. Since the surface area decreases as the pore diameter increases due to the increase in volume occupied by larger sized pores, this is a good indication that the pore size of the foam increased.

These bulk samples were then imaged using SEM. The results of the SEM images from these samples are shown in Fig. 5-14. The SEM images show that these modifications have changed the structure when compared to the standard transparent aerogel [Fig. 5-14(a)], and these modifications have larger voids or pores. The LC method [Fig. 5-14(b)] shows that the primary particles are larger than the other three samples analyzed, and that this increase leads to the increase in the pore size of the aerogel. The PA method samples are both similar to each other in that its primary particle size did not change when compared to the standard R/F, but we do see a web-like structure in the SEM images [Fig. 5-14(c,d)] which shows larger voids or pores than the standard R/F sample.

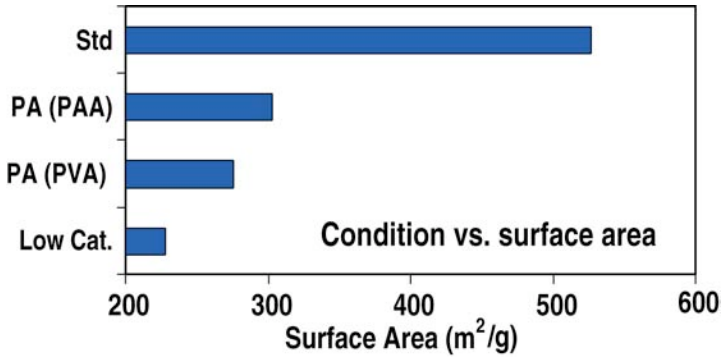

Fig. 5-13. Nitrogen absorption data of the large pore and standard small pore R/F foams. The surface area increases as pore diameter decreases due to the increase in volume occupied by larger sized pores.

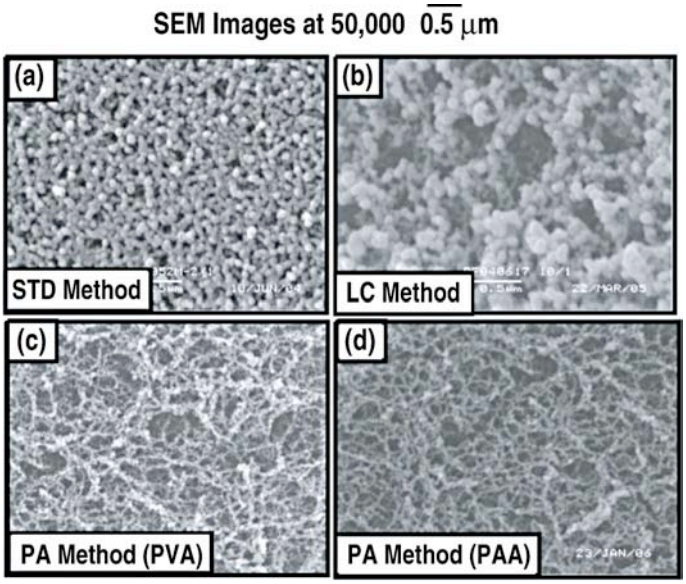

Fig. 5-14. SEM images of the R/F aerogels made with different methods, showing the structure and pores of the aerogel. The LC, and PA methods show that it has larger pores and a different structure than the R/F fabricated using the standard method.

After acquiring this data, we sent these bulk R/F samples to be analyzed for aerogel structure using the APS USAXS instrument. Because the aerogel is ~5% solid material and is mostly empty space, most of the scattering is from the solid material and not the voids. Usually, for more common low porosity materials, the scattering is dominated by the scattering from the voids, in which case the structure of the pores can be analyzed. However, in the present case of high-porosity materials, the USAXS provides information about the solid structure of the aerogel, at least at high-scattering vector (Q) data. At small Q values, where the microstructure is probed on large length scales, the dominating inhomogeneities in this material can be caused by a large void or structure. As this microstructure is

quite complex, we must use a combination of both the USAXS and the SEM to deduce the changes to the overall aerogel structure by processing modifications.

A plot showing the scattered intensity vs. Q from the USAXS is shown in Fig. 5-15. Information on the particle size and structure can be determined from this scattering data using, for example, the Unified fit method by Beaucage, et al. [5-28]. To analyze the structural features of these aerogels using this method, we need to analyze the Guinier areas, also referred to as knees, which supply information on the size of scatter using radius of gyration (R_g) approximation. The R_g values are related to various sizes of the primary particles as well as any inhomogeneities in the aerogel. These knees are followed, at higher Q values, by regions of power-law exponential decay, which can either provide information about the shape and structural arrangement of the scattering features or their specific surface area, depending on the power law slope. The detailed analysis of the exponential decay areas has not been attempted in this short work, but may be addressed in future publications.

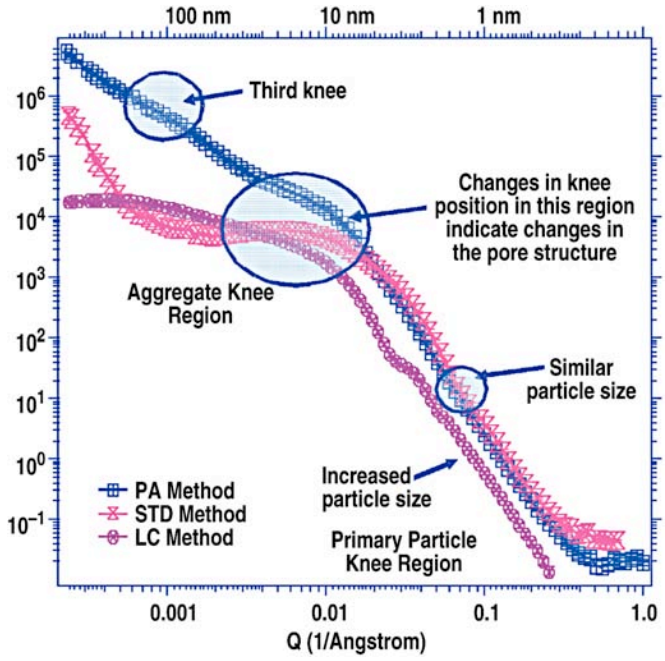

Fig. 5-15. Reduced data of the USAXS scans of these R/F aerogels made with different methods. This data along with the SEM data can provide a way to interpret the pore and structure change of the R/F aerogel due to the various process changes using the LC and PA methods.

Significant change in the scattering curve, Fig. 5-15, for an LC method produced sample indicates major change in the structure of this sample as compared with STD and PA produced samples. The shift in the knee between 0.01 and 0.06 $Å^{-1}$ to smaller Q values indicates that an LC manufactured sample has larger primary particle size than an STD sample, in agreement with SEM data. A PA method produced sample exhibits more complex behavior, which is discussed later, but the high Q data agreement between STD and particle size curves indicates that the primary particles for the STD and PA method are similar, also in agreement with the SEM data. Unique to USAXS, very valuable

information about the structures is obtained from the second knee region at Q values below 0.001 $Å^{-1}$ where the aggregation of the primary particles manifests itself. In this region, the three methods of sample manufacturing produce significantly different curves indicating major structural differences in these modified aerogels.

In summary, we developed a method to produce a larger pore R/F that was more compatible with our fabrication process to produce hollow R/F spheres. This new method did not have the dramatic density change that was seen using the previous large pore fabrication method. In addition to looking at methods that were used to analyze the structural modifications to R/F with the previous work, we also investigated USAXS as another method to analyze these structural changes.

5.3. NLUF TARGET DEVELOPMENT

5.3.1. Embedding Sapphire Spheres in Resorcinol Formaldehyde Aerogel for Astrophysical Jet Experiments

Traditionally, astrophysical jets and shocks have been observed through telescopes, and have only recently been studied through computer simulations and scaled laser experiments [5-29, 5-30]. A series of these scaled laser experiments for astrophysical jet studies was conducted on OMEGA at the Laboratory for Laser Energetics (LLE) [5-31]. These experiments involved using cylindrical R/F aerogel targets embedded with a sapphire sphere or spheres. Previous work done on fabricating generation 1 targets used a 100 μm thick stalk to place the sphere in the required position [5-32]. This stalk results in a large density perturbation in the target, which can cause issues with the hydrodynamics of the experiment. Because of this concern, recent experiments required the stalk to be $\leq$ 1 μm thick in order to minimize the density perturbation in the foam when compared to the target. Another requirement change from the generation 1 target was the embedded sphere changed from a 1 mm diameter CH sphere to a 500 μm diameter sapphire sphere. In order to maintain a similar density ratio between the sphere and the foam, the aerogel densities for these new targets increased from 100 mg/cc to 300 mg/cc. Additionally, the generation 2 targets required targets with both one and two embedded spheres for these experiments.

The single and double sphere targets were successfully fabricated without a supporting stalk by modifying parameters such as the density of the dry R/F, gelation time and stability of the aerogel precursor solution, and use of a micromanipulator with a vacuum chuck for the sphere placement. When the R/F solution reached the appropriate viscosity, the sphere was released by turning off the vacuum pump. The vacuum chuck was then removed, creating a target with a suspended sphere. Fabrication of a single sphere target was also developed using a sub-micron thick spider silk support that will remain in the foam. This support stalk is approximately 100 times thinner than the stalk used with the generation 1 target. Simulations have shown that a perturbation at that size ($<$ 1 μm) will have minimal effect on the hydrodynamics of the astroshock experiment.

The sphere placement is very critical in order to compare the simulation with the experiment, and needs to be within the given specified target tolerances. The generation 2 targets required a 300 mg/cc R/F aerogel cylinder with a diameter of 4 mm and a length of 5 mm. The single sphere targets required the sphere to be placed within 500 μm of the center axis; the z offset of the sphere was

required to be 650 μm (±200 μm) from the drive face of the foam cylinder to the center of the sphere. The double sphere targets required the spheres to be within 700 μm from the center axis. The z offset for the first sphere needed to be 650 μm (±200 μm) from the drive face of the foam cylinder to the center of the sphere. The second sphere needed to be placed no more than 500 μm from the first sphere and the spheres should not contact each other. Initial characterization of the ball placement was done using optical microscopy. Characterization of perturbations and density variations in the aerogel was done by radiography. Radiography was also used to verify the optical measurements for sphere placement. These measurements showed that the ball was accurately placed and the aerogel matrix was not significantly altered by perturbations or density variations in the foam.

The targets were fabricated on an assembly station consisting of a 70°C water bath to gel the R/F precursor solution, a micromanipulator that was connected to a vacuum chuck and pump to hold/release and position the sphere, and cameras to monitor and measure the position of the sphere. A similar station was used for both the stalk-and-release method and the spider silk method.

The stalk-and-release method uses a vacuum chuck that is connected to a vacuum pump to hold the sphere in place. A dual vacuum chuck is used for double sphere targets. The vacuum chuck is then connected to the micromanipulator on the assembly station to position the sphere or spheres in the X, Y and Z directions. The R/F precursor solution is poured into a jar containing the cylindrical mold and placed into the 70°C water bath on the assembly station. The sphere is then placed and positioned into the mold using the vacuum chuck and micromanipulators, and the position of the sphere is measured and monitored with cameras that provide two orthogonal views. Once the solution becomes thick enough to suspend the sphere without creating a perturbation in the foam, the sphere is released and suspended, and the vacuum chuck is removed. The solution stays in the bath until it gels. Once gelled, the jar is placed into a post-cure oven to increase the gel's crosslink density. After post-cure, the target is removed, solvent exchanged, and dried as previously described. A picture of a single sphere and double sphere R/F foam target fabricated using this method is shown in Fig. 5-16.

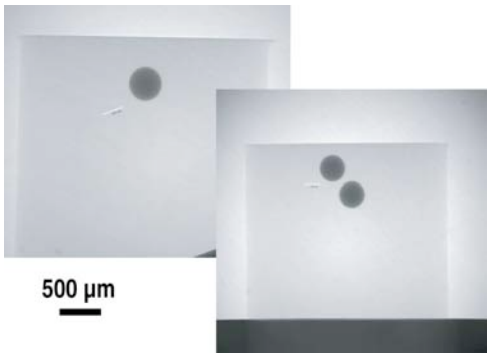

Fig. 5-16. Xradia images of R/F foam targets embedded with one and two free standing spheres with little to no perturbations in the foam.

The second method investigated was the spider silk method, which uses spider silk to support the sphere in the foam. Spider silk suspension has been a technique used at LLE for various fusion experiments [5-33]. The thickness of the spider silk is < 1 μm. At this thickness, the spider silk would create such a small perturbation in the foam that it would not affect the hydrodynamics of the experiment. Before a target is cast, the stalk, spider silk, sphere attachments must be fabricated. The spider silk attachments are assembled on an assembly station, which allows us to position and attach

the silk to the stalk and sphere. The attachments are held together by UV glue (Norland 68, Norland Products Inc.). The dispersion of the glue in controlled by dispensing the glue with a Femtojet micro-injector (Eppendorf). Once assembled, the spider silk attachment is attached to the vacuum chuck holder that is connected to the micromanipulator on the assembly station to position the sphere in the cylinder R/F foam target. This fabrication process is similar to the stalk-and-release method, except that the sphere was not to be released because it was held in place with a thin strand of spider silk that remains in the foam.

In order for the stalk and release method to be successful, the timing of the release of the sphere in the R/F solution is very critical to produce a target. For this to be a repeatable process it was critical that the viscosity of the R/F solution was stable at room temperature (RT) and had a consistent gelation time at 70°C. Results from the rheometer show that the R/F solution remains stable at RT with little to no viscosity change for 4–5 h, long enough to cast 6 targets. The results (Fig. 5-17) show that the viscosity change is very consistent when RT R/F solution (left at ambient conditions for 0–5 h) is heated at 70°C. In order for the viscosity to be high enough to suspend the ball, the sphere needed to be released before the 21st minute (when in the 70°C water bath) or the removal of the vacuum chuck would create a perturbation in the foam. At its optimal release time of 20 minutes, the R/F precursor solution would be viscous enough to suspend the sphere and backfill the area that the vacuum chuck takes when the chuck is removed, resulting in the desired free suspending sphere in an R/F foam cylinder with little or no perturbations. At 20 minutes, the viscosity of the solution was 4.7–5.2 Pa·s. The optimal release time was also found to be consistent within the 4–5 h time period. Pictures of targets when the sphere is released or not released at the optimal release time are shown in Fig. 5-18. Once the optimal release time is obtained, the stalk and release process can consistently produce a target having one or two free suspended spheres with little or no perturbations in the foam ~90% of the time.

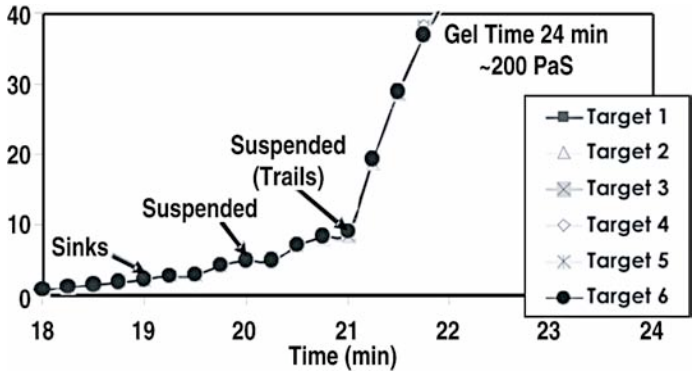

Fig. 5-17. Viscosity was measured for R/F solution sitting at ambient conditions at RT at 6 different times representing a target made during a production run. The viscosity data over time for each sample overlaps, indicating a consistent behavior for all 6 targets.

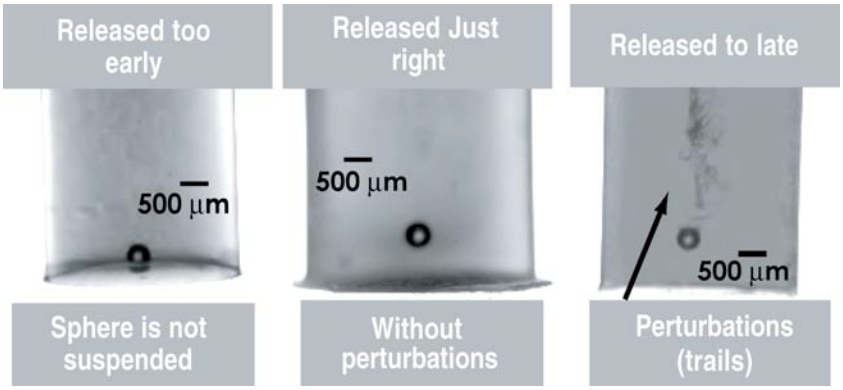

Fig. 5-18. Pictures of targets fabricated using the stalk and release method. Each picture shows the outcome of the placement of the sphere when it was released at various times.

Another requirement for these targets is that the spheres are positioned in the foam cylinder to the desired specifications. Measurements of the sphere placement in the foam targets show that 70% of the targets fabricated with the stalk-and-release method meet the sphere placement specifications. Placement of the sphere in the final target was less precise using the spider silk method with just 45% of the targets meeting the specifications. Because of the issues with the spider silk method that produce a lower yield of targets that meet the sphere placement specifications, the stalk-and-release method became the method of choice to fabricate the single and double sphere targets. The spider silk method may be revisited for future astroshock targets.

The double sphere targets were also fabricated using the stalk-and-release method. The yield for targets that meet the sphere placement requirements is 35%. This yield is lower when compared to the single sphere targets. This lower yield is the result of the limitations that we have with the spacing of the two stalks on the dual vacuum chuck. In the future, we will look at ways to improve this yield, by improving the design of a the dual vacuum chuck system. Figure 5-19 shows an assembled generation 2 astroshock target that was shot on OMEGA.

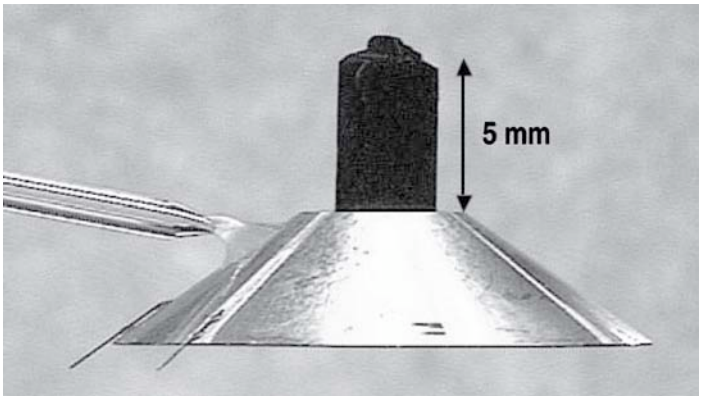

Fig. 5-19. Final assembled generation 2 astroshock target with shield, hohlraum and stalk that was shot on OMEGA.

REFERENCES FOR SECTION 5

[5-1] M.L. Hoppe, "Large Glass Shells from GDP Shells," Fusion Technol. **38**, 42 (2000).

[5-2] S.A. Letts, E.M. Fearon, S.R. Buckley, M.D. Saculla, L.M. Allison, and R. Cook, "Fabrication of Polymer Shells Using a Decomposable Mandrel," Fusion Technol. **28**, 1797 (1995).

[5-3] R.B. Stephens, T. Mroczkowski, J. Gibson, "Seeing Shell Wall Fluctuations," Fusion Technol. **38**, 132 (2000).

[5-4] R.J. Roark, W.C. Young, *Formulas for Stress and Strain*, 5th ed. (Columbus, McGraw-Hill Book Company, 1989) p. 557.

[5-5] S.A. Letts, E.M. Fearon, S.R. Buckley, M.D. Saculla, L.M. Allison, R. Cook, "Fabrication of Polymer Shells Using a Depolymerizable Mandrel," Fusion Technol. **28**, 1797 (1995).

[5-6] B.W. McQuillan, A. Nikroo, D.A. Steinman, F.H. Elsner, D.G. Czechowicz, M.L. Hoppe, M. Sixtus, W.J. Miller, "The PAMS/GDP Process for Production of ICF Target Mandrels," Fusion Technol. **31** (1997).

[5-7] M.L. Hoppe, "Recent Developments in Making Glass Shells from Silicon Doped GDP Shells," Fusion Technol. **41**, 234 (2005).

[5-8] M.L. Hoppe, "Large Glass Shells from GDP Shells," Fusion Technol. **38**, 42 (2000).

[5-9] B.C. Cook, M. Anthamatten, S.A. Letts, A. Nikroo, D.G. Czechowicz, "IR Absorptive Properties of Plastic Materials Used in ICF Capsules," Fusion Technol. **45**, 148 (2004).

[5-10] A. Nikroo and J.M. Pontelandolfo, "Fabrication of Thin Walled Glow Discharge Polymer Shells," Fusion Technol. **38**, 58 (2000).

[5-11] R.B. Stephens, T Mroczkowswi, J.B. Gibson, "Seeing Shell Wall Fluctuations," Fusion Technol. **38**, 132 (2000).

[5-12] R.L. McEachern, C.E. Moore, and R.J. Wallace, "The Design, Performance, and Application of an Atomic Force Microscope-Based Profilometer," J. Vac. Sci. Technol. **A13**, 983 (1995).

[5-13] M.L. Hoppe, R.B. Stephens, "Characterization of Chemical Dopants in ICF Targets," Fusion Technol. **31**, 504 (1997).

[5-14] E.L. Alfonso, J.S. Jaquez, A. Nikroo, "Using Mass Spectrometry to Characterize Permeation Half-life of ICF Targets," Fusion Technol. **49**, 773 (2006).

[5-15] E.L. Alfonso, I. Anteby, D.R. Harding, "Temperature Profiles and l=1 Nonuniformity within Cryogenic ICF Targets," Fusion Technol. **38**, 149 (2000).

[5-16] R.B Stephens, et al., "Seeing Shell Wall Fluctuations," Fusion Technol. **31**, 132 (2000).

[5-17] E.L. Alfonso, et al., "Using Mass Spectrometry to Characterize Permeation Half-Life of ICF Targets," Fusion Sci. Technol. **49**, 773 (2006).

[5-18] G.W. Collins, et al., "Surface Roughness Scaling of Plasma Polymer Films," Phys. Rev. Lett. **73**(5), 708 (1994).

[5-19] R.R. Paguio, et al., "Development of NIF scale Resorcinol Formaldehyde Foam Shells for Cryogenic Ice Layering Experiments on OMEGA," Presented at the 18th Annual Target Fabrication Specialist Meeting, Lake Tahoe, CA, 2008.

[5-20] R.W. Pekala, et al., J. Mater. Sci. **24**, 3321 (1989).

[5-21] D.W. Schafer, et al., J. Non-Cryst. Solids **186**, 159 (1995).

[5-22] C. Frederick, et al., Fusion Sci. Technol. **49**, 657 (2006).

[5-23] R. Paguio, et al., Fusion Sci. Technol. **51**, 682 (2007).

[5-24] A. Nikroo, et al., Fusion Sci. Technol. **45**, 84 (2004).

[5-25] R. Paguio et al., Polymeric Material: Science & Engineering **95**, 872 (2006).

[5-26] J. Ilavsky, et al., submitted to J. Appl. Cryst., 2008.

[5-27] S. Brunauer, et al., J. Am. Chem. Soc. **60**, 309 (1983).

[5-28] G. Beaucage, et al., J. Appl. Cryst. **28**, 717 (1995).

[5-29] S. Massaglia, Astrophysical Jets, Taylor & Francis (1998).

[5-30] P.A. Rosen, et al., "Laboratory-Astrophysics Jet Experiments at the OMEGA Laser Facility," J. Phys. IV France **133**, 857 (2006).

[5-31] R.F. Coker, et al., "Numerical Simulations & Astrophysical Applications of Laboratory Jets at OMEGA," Astrophys. Space Sci., **307**, 57 (2007).

[5-32] K.K. Dannenberg, et al., "Characterization of Embedded Spheres in Opaque Foams," Fusion Sci. Technol. **51**, 673 (2007).

[5-33] M. Bonino, "Material Properties of Spider Silk," University of Rochester Master Thesis, (2003).

6. SNL TARGET DEVELOPMENT

Z and Saturn targets though much larger than OMEGA targets are very complex and present many challenges as illustrated in Figs. 6-1, 6-2, and 6-3. For example, the Astroshock targets had one or two spheres embedded in an often opaque foam. The challenge was to center the sphere with respect to the radiation entrance hole of the hohlraum.

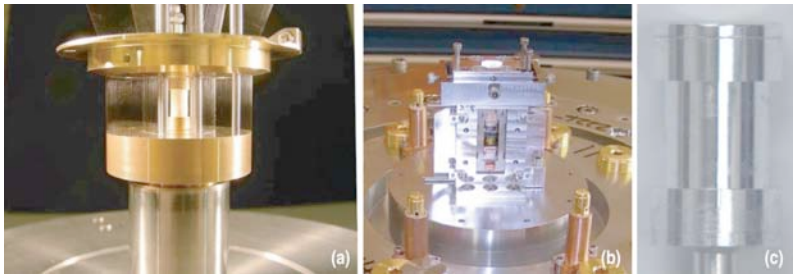

Fig. 6-1. Z targets. (a) Wire array, (b) EOS, and (c) a prototype cylindrical target.

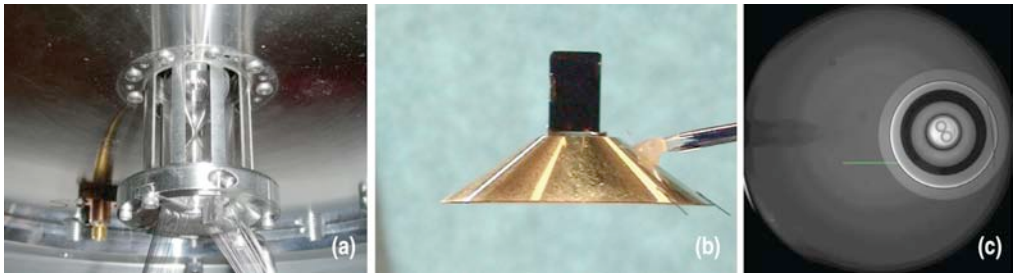

Fig. 6-2. These images are (a) a Saturn wire array, (b) a foam OMEGA target (whose assembly challenge was to center the optically invisible spheres in the aperture of the hohlraum), and (c) a radiograph of the same target showing the two spheres in the aperture.

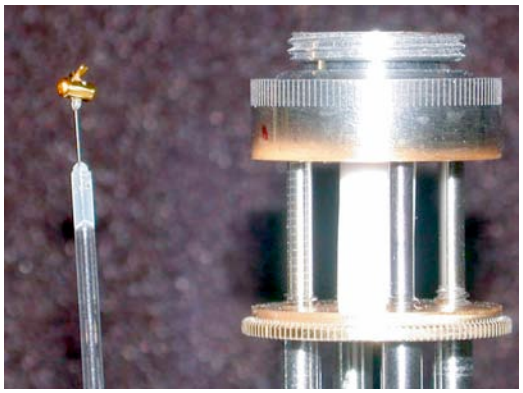

Fig. 6-3. This photo shows the difference in scale between an OMEGA hohlraum on the left and a dynamic (foam) Z hohlraum on the right.

It is important to remember that the differences in scale and requirements between the Z/Saturn targets and the OMEGA targets have required the SNL support staff to be flexible and diverse in their abilities and their equipment.

In spite of the reduced shot rate on Z due to its refurbishment, FY08 was a very constructive time for GA support of Z. There was the restructuring of the labor force that added the Load Assembly personnel from Ktech Corp. to this effort making a cohesive unit out of the two groups, Target Fabrication and Load Assembly, responsible for assembling the target and the load. ISO processes were combined, a single production meeting was instituted and cross training was begun. The success of this integration is demonstrated by a successful semi-annual ISO audit in February 2008 and a successful recertification audit in June 2008.

The total staff includes 9 FTEs which is reduced from the full staff of 17 FTE that had been required when Z was firing at its maximum rate of ~200 shots per year. This reduced staffing will need to be augmented as the shot rate increases.

6.1. CYLINDRICAL TARGET DEVELOPMENT

In addition to the standard operations at Z, GA and SNL, we began a joint effort to bring on line new cylindrical target capabilities of the type shown in Fig. 6-1. The goal of these efforts was to stand up facilities at both locations, have the GA facility produce targets first, then transfer the production of targets to SNL and maintain the facility at GA for target research and development. To begin the effort, equipment was set up in the vault at the GA San Diego facility and test parts were fabricated. As this was being pursued, SNL refurbished Building 984, converting it to a vault type room and outfitting it with two Precitech single point diamond turning machines, a Wyko profilometer, and an Xradia.

GA added significant equipment to both the GA and SNL facilities. For the GA laboratory in San Diego two items were purchased:

1. Laser micrometer ($15K)
2. Measuring Nikon microscope ($55K)

For the effort at SNL, GA purchased:

1. A custom Xradia radiography system for cryogenic targets ($451K)
2. Zygo interferometer for characterizing large surface areas ($80K)
3. Two micrometers including a three axis laser micrometer ($23K)
4. Three video microscopes for characterization and image capture ($12K)
5. Measuring Nikon microscope with polarizer and differential interference contrast (DIC) capabilities ($83K)

Experienced machinists and material scientists led the development work and a dedicated machinist was trained on the techniques needed to produce the targets with the goal of transferring the work to SNL in FY09. At the end of FY08, the Precitech machines were ready to begin making prototype targets, the radiography system and 3 axis micrometer are collecting data and the profilometer is operating in the manual mode.

The development effort required to characterize the cylindrical targets occurred at GA and included: 1) optical techniques to measure external physical dimensions, 2) pressure testing to ensure target integrity and monitor deformation under pressure, 3) radiography to measure wall thickness and uniformity (including concentricity of OD/ID) and 4) surface finish measurement. The optical characterization is very straightforward, but the other techniques deserve some discussion.

The pressure test has two phases. In the first phase, the target is pressurized and the incoming line is sealed. The pressure in monitored for 24 hours to determine if there are any leaks. In the second phase, the target again starts at atmospheric pressure and is pressurized. This time the deformation of the part is monitored. The part is placed in a polycarbonate chamber under an interference microscope and the change in diameter is monitored (Fig. 6-4). Deformations of over 4 microns have been noted for a pressure of 800 psi. Catastrophic failures have occurred but the polycarbonate enclosure has prevented damage or injury very well.

Fig. 6-4. (a) Interference microscope with polycarbonate safety enclosure (colored aqua). (b) A prototype target that catastrophically failed during the pressure testing.

The radiography characterization is done using a commercial system microcomputed tomography system (MicroCT) supplied by Xradia. This system can generate x-rays in the 40 to 150 keV regime. Images are collected on a CCD with typically 1 to 2 minute exposure times. The radiographs are used to characterize the wall thickness and wall uniformity (most notably, the wall non-uniformity caused by any misalignment of the OD and ID), the appearance of the glue bond and the depth of the end cap into the cylinder (Fig. 6-5). The complete characterization of a target requires 22 radiographs using three magnifications and requires the rotation of the target by 90° to obtain orthogonal views.

The surface characterization is complicated by the cylindrical surface of the target. To obtain a full scan of the surface the part must be rotated. This is done using a Newport programmable controller and rotary stage. The part is held in a custom fabricated vacuum stand placed on a Wyko NT3300 profilometer (Fig. 6-6). The two are coordinated using a LabView program that synchronizes the rotation, image collection and image saving. The images are stitched together to compile the location, size, quantity and distribution of sub-micron and larger defects. Defects can be caused by machining or handling issues, but more importantly can be intrinsic in the material as a function of the alloy being used. Figure 6-7 is an example of the compiled data and a representation of that data on a representation of a target. To date, the proof-of-principle for this characterization technique is done but it is not yet able to do targets on a routine basis.

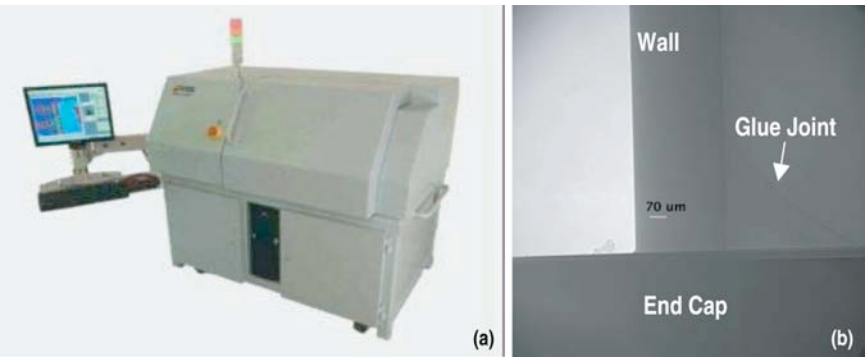

Fig. 6-5. (a) The Xradia system has computer controlled stages, source and camera systems contained within an intrinsically safe lead lined enclosure. (b) The radiograph shows typical features of the cylindrical target.

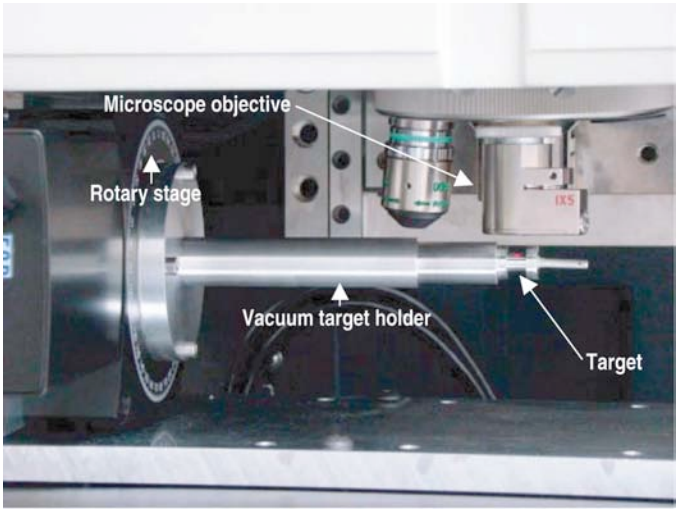

Fig. 6-6. This image shows the Wyko objective lens above the part being characterized. The red dot is the illumination from the Wyko. The disk to the left is the Newport rotary stage.

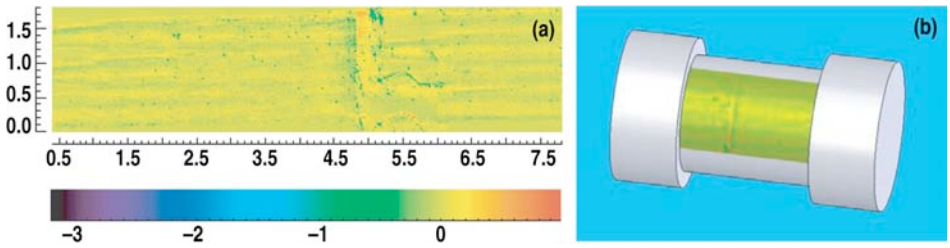

Fig. 6-7. (a) A 2D surface map compiled from 40 scans. (b) The schematic on the right shows those scans overlaid on a hypothetical target.

In summary, the development and production task for cylindrical ICF targets has been extensive, and very successful. As a measure of that success, please note that 17 targets were characterized and successfully shot on Z in FY08.

6.2. CRYOGENIC FAST IGNITION TARGET DEVELOPMENT

In addition to the cylindrical target development there was a cryogenic target development task. This target is designed to show proof-of-principle for a cryogenic fast igniter target compatible with the Z driver. This target development was begun in FY07. The assembly of this target proved to be unsuccessful until the design underwent a revision (in the beginning of FY08) that allowed for a larger fill tube. This fill tube is required to supply the hydrogen. Thanks to the redesign, three completed assemblies have been supplied and are undergoing testing to determine the strength on the inner thin walled shell (Figs. 6-8 and 6-9).

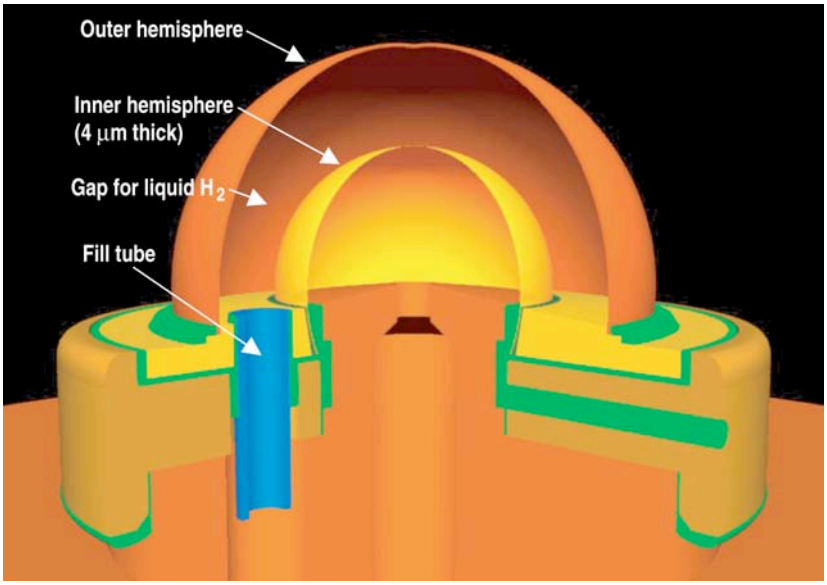

Fig. 6-8. This CAD drawing shows the redesigned cryogenic fast igniter target. The larger fill tube was required to prevent clogging of the fill tube during assembly.

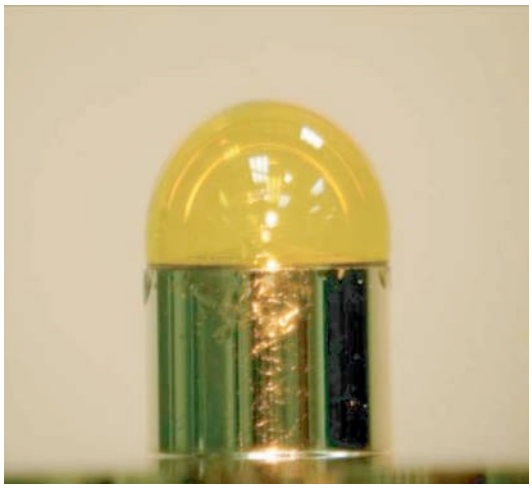

Fig. 6-9. This is a partial assembly showing the outer and inner hemispheres and the careful alignment. This alignment is required to produce a uniform hydrogen layer during the experiment.

Summary for Section 6

The refurbishment of Z has been a success. Z fired 82 times in FY08 and the rate of 3 shots a week is being exceeded in FY09. Understanding of the new machine design is developing and will result in innovations in target designs. The on-site and GA personnel in San Diego are actively contributing to target design, fabrication and fielding and look forward to many achievements.

7. PUBLICATIONS FY08

7.1. LIST OF PUBLICATIONS

Alexander, N.B., Stephens, R.B., Sweet, W.S., Brown, L.C., "Investigation and Attachment of Polyimide Fill Tubes," Proc. 18th Topical Meeting on the Technology of Fusion Energy (TOFE), San Francisco, California, 2008, to be published in Fusion Sci. Technol.

Alfonso, E.L., Moreno, K.A., Wilkens, H.L., Jaquez, J.S., Nikroo, A., "Investigation of Larger Poly(a-Methylstyrene) Mandrels for High Gain Designs Using Microencapsulation," Proc. 18th Target Fabrication Meeting, Lake Tahoe, California, to be published in Fusion Sci. Technol.

Bousquet, J.T., Hund, J.F., Goodin, D.T., Alexander, N.B., "Development of High Quality Poly(a-methylstyrene) Mandrels for NIF," Proc. 18th Target Fabrication Meeting, Lake Tahoe, California, 2008, to be published in Fusion Sci. Technol.

Chen, K.C., Nguyen, A.L.Q., Huang, H., Eddinger, S.A., Nikroo, A., "Stiffening of PAMS Mandrels During Curing," Proc. 18th Target Fabrication Meeting, Lake Tahoe, California, 2008, to be published in Fusion Sci. Technol.

Eddinger, S.A., Huang, H., Schoff, M.E., "Optimization of Plasma Uniformity in Laser-Irradiated Underdense Targets," Proc. 18th Target Fabrication Meeting, Lake Tahoe, California, 2008, to be published in Fusion Sci. Technol.

Fong, J.R., Eddinger, S.A., Huang, H., Moreno, K.A., "A Target Fabrication and Injection Facility for Laser-IFE," Proc. 18th Target Fabrication Meeting, Lake Tahoe, California, 2008, to be published in Fusion Sci. Technol.

Frederick, C.A., Forsman, A.C., Hund, J.F., Eddinger, S.A., "ARIES Inertial Fusion Chamber Assessment," Proc. 18th Target Fabrication Meeting, Lake Tahoe, California, 2008, to be published in Fusion Sci. Technol.

Gibson, C.R., Baltz, J., Malsburay, T., Atkinson, D., Brugmann, V., Coffield, F., Hund, J.F., Paguio, R.R., Schroen, D.G., "Mechanical Response of the Target Acceleration for a Laser Fusion Power Plant," Proc. 18th Target Fabrication Meeting, Lake Tahoe, California, 2008, to be published in Fusion Sci. Technol.

Goodin, D.T., Nikroo, A., Petzoldt, R.W., Alexander, N.B., Carlson, L.C., "Wake Shield Target Protection," Proc. 18th Topical Meeting on the Technology of Fusion Energy (TOFE), San Francisco, California, 2008, to be published in Fusion Sci. Technol.

Haid, B.J., Malsbury, T.N., Gibson, C.R., Warren, C.T., "Development of a GDP Coater Enabling Increased Production," Proc. 18th Target Fabrication Meeting, Lake Tahoe, California, 2008, to be published in Fusion Sci. Technol.

Hoppe, M.L., Vermillion, B.A., "Mass Production Methods for IFE Targets," Proc. 18th Target Fabrication Meeting, Lake Tahoe, California, 2008, to be published in Fusion Sci. Technol.

Huang, H., Eddinger, S.A., Schoff, M.E., "Developing Depleted Uranium and Gold Cocktail Hohlraums for the National Ignition Facility," Proc. 18th Target Fabrication Meeting, Lake Tahoe, California, 2008, to be published in Fusion Sci. Technol.

Huang, H., Eddinger, S.A., Stephens, R.B., Nikroo, A., "Investigating the Potential of Using Focused Ion Beam Technology to Drill Holes in and Attach Fill-Tubes to a Beryllium Ablator," Proc. 18th Target Fabrication Meeting, Lake Tahoe, California, 2008, to be published in Fusion Sci. Technol.

Huang, H., Nikroo, A., Stephens, R.B., Eddinger, S.A., "Microencapsulation Studies for Mass Production of IFE Targets," Proc. 18th Target Fabrication Meeting, Lake Tahoe, California, 2008, to be published in Fusion Sci. Technol.

Johal, Z.Z., Crippen, J.W., Forsman, A.C., Lundgren, E.H., Moreno, K.A., Nikroo, A., "Progress in Coating Multi-Layered Cocktail Hohlraums," Proc. 18th Target Fabrication Meeting, Lake Tahoe, California, 2008, to be published in Fusion Sci. Technol.

Lee, Y.T., Johnson, M.A., Nikroo, A., Montesanti, R.C., Huang, H., "A Comprehensive Assessment of Solar Thermochemical Water-Splitting Cycles for Hydrogen Production," Proc. 18th Target Fabrication Meeting, Lake Tahoe, California, 2008, to be published in Fusion Sci. Technol.

Lundgren, E.H., Forsman, A.C., "Materials Development for Sulfur-Iodine Thermochemical Hydrogen Production Process," Proc. 18th Target Fabrication Meeting, Lake Tahoe, California, 2008, to be published in Fusion Sci. Technol.

Luo, R.W., Greenwood, A.L., Nikroo, A., Chen, C., "Beryllium Capsule Coating Development for NIF Targets," Proc. 18th Target Fabrication Meeting, Lake Tahoe, California, 2008, to be published in Fusion Sci. Technol.

Nguyen, A.L., Eddinger, S.A., Huang, H., Lee, Y.T., Moreno, K.A., Schoff, M.E., "Dissociative Adsorption of Br2 on Pt(111): Hot Atom Dynamics," Proc. 18th Target Fabrication Meeting, Lake Tahoe, California, 2008, to be published in Fusion Sci. Technol.

Paguio, R.R., Frederick, C.A., Havsky, J., Hund, J.F., Nikroo, A., Thi, M.A., "Br Surface Chemistry and Corrosion on Pt(111) Surface," Proc. Materials Research Society Fall Meeting, Boston, Massachusetts, to be published in Mater. Res. Soc. Symp. Proc.

Paguio, R.R., Hund, J.F., Blue, B.E., Schroen, D.G., Saito, K.M., "STM Study of Oxygen on Rh(111)," Proc. 18th Target Fabrication Meeting, Lake Tahoe, California, 2008, to be published in Fusion Sci. Technol.

Paguio, R.R., Nikroo, A., Saito, J.M., Hund, J.R., Castillo, E.R., "STM Investigation of Hot Bromine Atom Chemistry on Pt(111)," Proc. 18th Target Fabrication Meeting, Lake Tahoe, California, 2008, to be published in Fusion Sci. Technol.

Petzoldt, R.W., Valmianski, E.I., Carlson, L.C., Stromose, J., Hares, J.D., "Oxygen Interactions with Mo(001) Surface Studied by STM," Proc. 18th Topical Meeting on the Technology of Fusion Energy (TOFE), San Francisco, California, 2008, to be published in Fusion Sci. Technol.

Saito, K.M., Hund, J.F., Paguio, R.R., Nikroo, A., Crippen, J.W., Johal, Z.Z., "Molecular NO Islands Versus O and N Islands on Rh(111) Surface Studied by STM," Proc. 18th Target Fabrication Meeting, Lake Tahoe, California, 2008, to be published in Fusion Sci. Technol.

Sheliak, J.D., Geller, D.A., Hoffer, J.K., "Oxygen Induced Missing Row Reconstruction on Mo(001) (2x1) Studied by STM," Proc. 18th Topical Meeting on the Technology of Fusion Energy (TOFE), San Francisco, California, 2008, to be published in Fusion Sci. Technol.

Stephens, R.B., Alexander, N.B., Brown, L.C., Goodin, D.T., Petzoldt, R.W., Sweet, W.S., "Cs Adsorption on Si(001) 2x1 Studied by STM, LEED/AES," Proc. 18th Topical Meeting on the Technology of Fusion Energy (TOFE), San Francisco, California, 2008, to be published in Fusion Sci. Technol.

Stephens, R.B., MacKinnon, A.J., Offerman, D., Akli, K.U., Bartal, T., Beg, F.N., Clark, D. Chawla, S., Chen, C.D., Freeman, R.R., Hey, D.S., "Co Cluster Growth and Induced Surface Morphology Changes on HOPG Studied by STM," Proc. Intl. Conf. on HEDP/HEDLA-08, St. Louis, Missouri, 2008.

7.2. LIST OF PRESENTATIONS

Alexander, N., "Target Supply and Fielding for Rep-Rated High-Power Lasers," 18th Target Fabrication Specialists' Meeting, Lake Tahoe, California, May 11-15, 2008.

Alfonso, N., "Update on Techniques to Measure the Thickness of Au and AuB Liners on Uranium Hohlraums," 18th Target Fabrication Specialists' Meeting, Lake Tahoe, California, May 11-15, 2008.

Alger, E., "Overview of Shell Fabrication for Cryogenic Implosions on OMEGA," 18th Target Fabrication Specialists' Meeting, Lake Tahoe, California, May 11-15, 2008.

Back, C., "Exploring Novel Physics in the Laboratory Using Low Density Materials," 13th Intl. Workshop on Radiative Properties of Hot Dense Matter, Santa Barbara, California, November 10-14, 2008.

Back, C., "GA Support for High Energy Density Experiments," JOWOG, Albuquerque, New Mexico, February 6, 2008.

Blue, B., "Shock-Clump Interaction Studies in the Laboratory," 50th APS Meeting of the Div. of Plasma Physics, Dallas, Texas, November 17-21, 2008.

Bousquet, J., "Advancements in Glow Discharge Polymer (GDP) Coatings for Mass Production," 18th Target Fabrication Specialists' Meeting, Lake Tahoe, California, May 11-15, 2008.

Chen, K., "Fabrication of Low Density Gold Foams Using Resorcinol Formaldehyde Foam as Templates," 18th Target Fabrication Specialists' Meeting, Lake Tahoe, California, May 11-15, 2008.

Chen, K., "Update on Ge:CH Capsule Production for NIF," 18th Target Fabrication Specialists' Meeting, Lake Tahoe, California, May 11-15, 2008.

Eddinger, S., "3D Wall-Mapping Using X-Radia with Distortion Correction," 18th Target Fabrication Specialists' Meeting, Lake Tahoe, California, May 11-15, 2008.

Eddinger, S., "Creating a Precision Optical Depth Uniformity Tool for ICF Targets," 50th APS Meeting of the Div. of Plasma Physics, Dallas, Texas, November 17-21, 2008.

Eddinger, S., "Precision Radiography (PR) Update," 18th Target Fabrication Specialists' Meeting, Lake Tahoe, California, May 11-15, 2008.

Florio, J., "Layering Target Base Assemblies," 18th Target Fabrication Specialists' Meeting, Lake Tahoe, California, May 11-15, 2008.

Fong, J., "Absorption Edge Spectroscopy for ICF Target Characterization," 18th Target Fabrication Specialists' Meeting, Lake Tahoe, California, May 11-15, 2008.

Fooks, J., "Assembly and Capsule-Centering for NIC Hohlraum Energetics Targets," 18th Target Fabrication Specialists' Meeting, Lake Tahoe, California, May 11-15, 2008.

Forsman, A., "Laser-Matter Interactions Confined in Small High Aspect Ratio Holes," Warm Dense Matter School, Berkeley, California, January 16, 2008.

Frederick, C., "Fabrication of Tantalum Oxide Foam Thin Films for Radiation Transport Experiments," 18th Target Fabrication Specialists' Meeting, Lake Tahoe, California, May 11-15, 2008.

Frederick, C., "Laser Machining of Complex Features into Tantalum Oxide Thin Films," 18th Target Fabrication Specialists' Meeting, Lake Tahoe, California, May 11-15, 2008.

Giraldez, E., "Machining And Metrology of a 51 Mode Perturbation on Drive Disks for Supernova Raleigh Taylor Experiments," 18th Target Fabrication Specialists' Meeting, Lake Tahoe, California, May 11-15, 2008.

Greenwood, A., "Current Experimental Layering Target Assembly and Future NIF Target Production," 18th Target Fabrication Specialists' Meeting, Lake Tahoe, California, May 11-15, 2008.

Greenwood, A., "Overview of Shell Fabrication for Cryogenic Implosions on OMEGA," 18th Target Fabrication Specialists' Meeting, Lake Tahoe, California, May 11-15, 2008.

Hoppe, M., "High Z Doping of Glass Shells," 18th Target Fabrication Specialists' Meeting, Lake Tahoe, California, May 11-15, 2008.

Huang, H., "Element Specific Dopant/Impurity Profiling for ICF Ablator Capsules," 18th Target Fabrication Specialists' Meeting, Lake Tahoe, California, May 11-15, 2008.

Huang, H., "Quantitative Data Analysis Method for Precision Radiography," 18th Target Fabrication Specialists' Meeting, Lake Tahoe, California, May 11-15, 2008.

Huang, H., "Quantitative Dimension Measurement of ICF Components Using X-radia," 18th Target Fabrication Specialists' Meeting, Lake Tahoe, California, May 11-15, 2008.

Huang, H., "Quantitative Dopant/Impurity Analysis for ICF Targets," 50th APS Meeting of the Div. of Plasma Physics, Dallas, Texas, November 17-21, 2008.

Huang, H., "Quantitative Impurity Analysis for ICF Targets," 18th Target Fabrication Specialists' Meeting, Lake Tahoe, California, May 11-15, 2008.

Hund, J., "Characterization of Tantalum Oxide Aerogel Radiation Transport Targets," 18th Target Fabrication Specialists' Meeting, Lake Tahoe, California, May 11-15, 2008.

Hund, J., "Droplet Microfluidics and Target Fabrication," 19th HAPL Workshop, Madison, Wisconsin, October 22, 2008.

Hund, J., "HAPL Target Fabrication Update," 18th Target Fabrication Specialists' Meeting, Lake Tahoe, California, May 11-15, 2008.

Hund, J., "IFE Target Fabrication Update," 18th High Average Power Laser (HAPL) Workshop, Santa Fe, New Mexico, April 8, 2008.

Hund, J., "Progress on HAPL Foam Capsule and Overcoat Fabrication," 19th HAPL Workshop, Madison, Wisconsin, October 22, 2008.

Hund, J., "Target Technologies: Foams, Capsules and Target Insertion," 2nd European Target Fabrication Conference, United Kingdom, October 27, 2008.

Jaquez, J., "Fabrication and Characterization of Au/B Lined Au Hohlraums," 18th Target Fabrication Specialists' Meeting, Lake Tahoe, California, May 11-15, 2008.

Jaquez, J., "Fabrication and Characterization of Thin Ta Opacity Packages for Omega," 18th Target Fabrication Specialists' Meeting, Lake Tahoe, California, May 11-15, 2008.

Johal, Z., "Making Robust Capsule and Fill Tube Assemblies for the National Ignition Campaign," 18th Target Fabrication Specialists' Meeting, Lake Tahoe, California, May 11-15, 2008.

Lee, Y., "Increasing the Throughput of the Phase Shifting Diffraction Interferometer (PSDI)," 18th Target Fabrication Specialists' Meeting, Lake Tahoe, California, May 11-15, 2008.

Lundgren, E., "Laser Forming of Shaped Fill Holes in Beryllium Capsules," 18th Target Fabrication Specialists' Meeting, Lake Tahoe, California, May 11-15, 2008.

Luo, R., "Adjusting Coating Parameters to Optimize GDP Gas Barrier on RF Shells," 18th Target Fabrication Specialists' Meeting, Lake Tahoe, California, May 11-15, 2008.

Mauldin, M., "Fabrication and Metrology Development of Thermal Mechanical Package Structures for NIF Targets," 18th Target Fabrication Specialists' Meeting, Lake Tahoe, California, May 11-15, 2008.

Moreno, K., "Developments in Polishing of Beryllium Sputter Coated Samples for NIF and Omega Experiments," 18th Target Fabrication Specialists' Meeting, Lake Tahoe, California, May 11-15, 2008.

Moreno, K., "Overview of NIF Capsule Metrology," 18th Target Fabrication Specialists' Meeting, Lake Tahoe, California, May 11-15, 2008.

Nguyen, A., "Comparison of AFM and PSDI Data for ICF Targets with an Analysis of Shell Flipping Capability," 18th Target Fabrication Specialists' Meeting, Lake Tahoe, California, May 11-15, 2008.

Nikroo, A., "Fabrication and Metrology of Graded Copper Doped Beryllium Capsules with Fill Tubes for the National Ignition Facility," 18th Target Fabrication Specialists' Meeting, Lake Tahoe, California, May 11-15, 2008.

Paguio, R., "Development and Fabrication of NIF Scale Resorcinol Formaldehyde Foam Shells for Cryogenic Ice Layering Experiments," 18th Target Fabrication Specialists' Meeting, Lake Tahoe, California, May 11-15, 2008.

Paguio, R., "Fabrication of HAPL Sized R/F foam Shells - (IFE Target Fabrication Update)," 50th APS Meeting of the Div. of Plasma Physics, Dallas, TX, 19th HAPL Workshop, Madison, Wisconsin, October 22, 2008.

Paguio, R., "Fabrication of Resorcinol Formaldehyde Aerogel with Embedded Sapphire Spheres for Astrophysical Jet Experiments on OMEGA," 18th Target Fabrication Specialists' Meeting, Lake Tahoe, California, May 11-15, 2008.

Paguio, R., "Improvements on Permeation GDP Coatings for Resorcinol Formaldehyde Foam Shells for Cryogenic Experiments on OMEGA," 18th Target Fabrication Specialists' Meeting, Lake Tahoe, California, May 11-15, 2008.

Paguio, R., "Modifying the Pore Size of Resorcinol Formaldehyde Aerogels for Fabrication of Hollow Spheres for Direct Drive ICF Experiments," Materials Research Society, Fall Meeting, Boston, Massachusetts, December 1–5, 2008.

Saito, K., "Fill Tube Development for Foam Shells for OMEGA, NIF and Fast Ignition Application," 18th Target Fabrication Specialists' Meeting, Lake Tahoe, California, May 11-15, 2008.

Schroen, D., "The Process for Placing Embedded Objects in Foams," 18th Target Fabrication Specialists' Meeting, Lake Tahoe, California, May 11-15, 2008.

Stephens, R., "Connecting Simulations and Experiments in HEDP," FESAC, Washington DC, August 26, 2008.

Stephens, R., "Electron Generation in Fast Ignition Targets," 50th APS Meeting of the Div. of Plasma Physics, Dallas, Texas, November 17-21, 2008.

Stephens, R., "Electron Transport in Hot Dense Plasma," OMEGA EP User's meeting, Rochester, New York, April 7-8, 2008.

Stephens, R., "Generation and Transport of High Intensity Laser-Generated Hot Electrons in Cone Targets," 30th European Conf. on Laser Interaction with Matter (ECLIM), Darmstadt, Germany, September 1, 2008.

Stephens, R., "High Intensity Laser Coupling to a Cone Geometry for Fast Ignition," 10th Intl. Workshop on Fast Ignition of Fusion Targets, Crete, Greece, June 12-18, 2008.

Stephens, R., "Toward the Design of a Fast Ignition Target," 18th TOFE Meeting, San Francisco, California, September 28, 2008.

Vermillon, B., "The Assembly and Characterization of Dynamic Hohlraum Double Shell Targets," 18th Target Fabrication Specialists' Meeting, Lake Tahoe, California, May 11-15, 2008.

Wilkens, H., "Sputtered Depleted Uranium for Applications in Inertial Confinement Fusion," Physics and Astronomy Colloquium, California State University, Long Beach, California, October 6, 2008.

Wilkens, H., "An Update on the Fabrication of Depleted Uranium Hohlraums for the National Ignition Facility," 18th Target Fabrication Specialists' Meeting, Lake Tahoe, California, May 11-15, 2008.

Xu, H., "Reducing Argon Incorporation in Be Coatings," 18th Target Fabrication Specialists' Meeting, Lake Tahoe, California, May 11-15, 2008.

Youngblood, K., "The Development of an Automated Adhesive Delivery System," 18th Target Fabrication Specialists' Meeting, Lake Tahoe, California, May 11-15, 2008.